THE EFFECTS OF ALLOYING ELEMENTS AND EXPOSURE ATMOSPHERES ON SIGMA FORMATION IN FERRITIC ALLOYS

by

Rita Nalin Patel

BS in Materials Science and Engineering, University of Pittsburgh, 2012

Submitted to the Graduate Faculty of

The Swanson School of Engineering in partial fulfillment

of the requirements for the degree of

Master of Science

University of Pittsburgh

2014

UNIVERSITY OF PITTSBURGH

SWANSON SCHOOL OF ENGINEERING

This thesis was presented

by

Rita Nalin Patel

It was defended on

February 28, 2014

and approved by

Frederick S. Pettit, PhD, Emeritus Professor

Department of Mechanical Engineering and Materials Science

C. Isaac Garcia, PhD, Research Professor

Department of Mechanical Engineering and Materials Science

Larry R. Foulke, P.E., PhD, Adjunct Professor

Department of Mechanical Engineering and Materials Science

Thesis Advisor: Gerald H. Meier, PhD, William Kepler Whiteford Professor

Department of Mechanical Engineering and Materials Science

THE EFFECTS OF ALLOYING ELEMENTS AND EXPOSURE ATMOSPHERES ON SIGMA FORMATION IN FERRITIC ALLOYS

Rita Nalin Patel, M.S.

University of Pittsburgh, 2014

Tests were performed on a variety of model and commercial ferritic steels in simulated cathode and anode environments of an intermediate temperature solid oxide fuel cell (SOFC). The alloys were picked for their similarity to currently used interconnect materials. Results from the test provide inside into the effect of exposure atmospheres and alloying elements on the nucleation and growth of sigma phase in the ferritic alloys. Two possible mechanisms for sigma phase transformation were discussed, but the exact method was not able to be determined based on the results shown.

The cathode environment was simulated by either using dry laboratory air, or in the case of a pipe-sealant leak in the SOFC, dry air with 10% water vapor at 700 °C. Three model alloys were tested in these environments to determine the effect of water vapor and alloying elements on the nucleation and growth of sigma phase. It was confirmed that molybdenum is a sigma phase promoter and allows for the nucleation and growth to occur. The presence of water vapor in the exposure environment caused an increased amount of sigma phase formation, although the exact reason why remains unknown.

The anode environment was simulated by using an Ar-4%H_2-10%H_2O gas-water vapor mixture at 700 °C. A variety of model alloys and commercial alloys were tested in this environment. To simulate the effect of a nickel mesh touching the interconnect in the SOFC cell, nickel was electroplated onto some specimens prior to exposure. The pre-coat of nickel caused the formation of an austenitic interdiffusion zone in all alloys, and in all but the low-Cr alloy, this also lead to the formation of sigma phase. Two possible mechanisms for sigma phase formation were suggested. The first is that the ferrite phase decomposed directly into austenite and sigma phase. The second is that the ferrite phase first transformed into austenite, which then transformed into sigma phase. Neither method could be confirmed based on the results obtained.

TABLE OF CONTENTS

LIST OF TABLES

LIST OF FIGURES

PREFACE

I would like to thank my advisor, Dr. Gerald Meier, who gave me much guidance and help throughout this project. I'd also like to thank the other members of the High Temperature Oxidation research groups who helped me in and out of the lab throughout the duration of this work. I'm also very grateful for the help and support of the Forschungszentrum Research Group, particularly Leszek Niewolak, who aided me during my time in Germany.

Financially, this project would not have been possible without the aid of both the Office of Naval Research as well as the Department of Energy: Nuclear Energy University Programs. Both sources allowed for me to focus my time on work and school without additional distractions that may have arisen.

To my friends in and out of school: thank you for listening to me talk, complain, and rejoice during every step of my project. Particular thanks go to Corinne Gray, without whom I would have had no one to run away to the gym with, or even go down the street for lunch and ice cream. To my parents and family: thank you for your quiet, steady support. Your faith in my ability to succeed has always been a constant reminder in the back of my mind. Finally, to my best friend and the best sister I could ask for, I thank Ami Patel, the only person who knows how to commiserate with me when appropriate, send me cat pictures when appropriate, and make me laugh when all I wanted to do was cry. Thank you all so much.

1.0 INTRODUCTION

The world population growth has been accelerating for the past 100 years. The current world population is roughly 7 billion people, and in the next 70 years, it is expected to increase to 10 billion people (see Figure 1) [1].

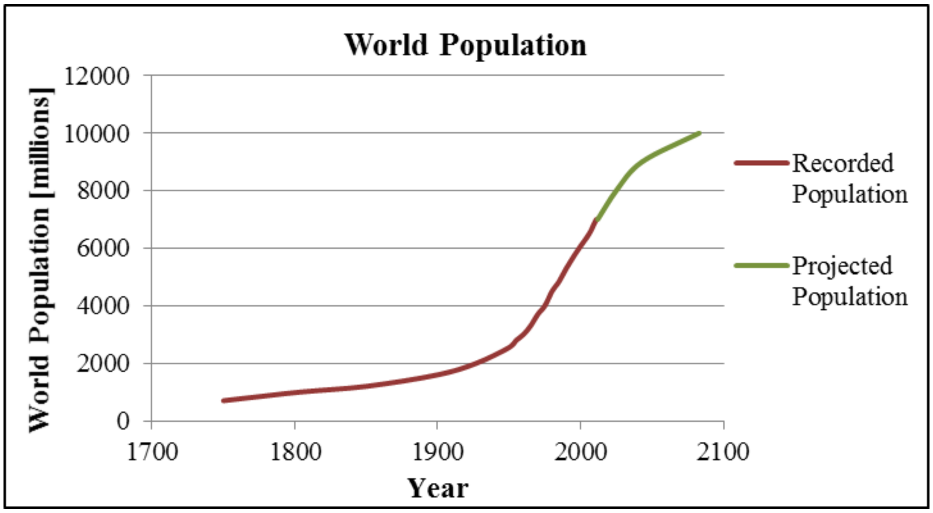

Figure 1. World Population Graph [1]

With the increase in world population, there comes an increasing demand for energy. Not only are developed countries such as the United States seeing a population surge, but underdeveloped countries such as China are rapidly developing and will also have an increased need for energy [2]. It becomes important, therefore, to analyze current energy sources and determine the best course of action for future energy needs. As the population of the world continues to expand, and countries continue to develop, the demand for viable energy sources will continue to escalate as well.

The use of a Solid Oxide Fuel Cell (SOFC) is a possible solution to the energy demand problem. Because the fuel cell relies on the conversion of chemical energy to electrical energy, as long as a continuous source of fuel and air is supplied, power can be generated. Also, unlike traditional batteries, if a fuel cell is not being operated, there is no loss of efficiency or wasted consumption of fuel [3, 4]. Some of the advantages of fuel cells include a higher efficiency, a lack of moving parts, relatively quiet operations, and low levels of emissions output when compared to traditional power sources. SOFCs could be used in a variety of environments, especially broad power generation or home power generation [3, 5].

One of the main advantages of the SOFC is its ability to operate at a range of temperatures while using a variety of fuel sources. These fuel sources can be pure hydrogen, or even a hydrocarbon such as natural methane gas [5]. Recently, there has been a push to lower the operating temperature of the SOFC. This will increase the durability and lifetime of the SOFC and its components as well as increasing its overall efficiency [3, 5, 6].

The biggest drawback to the use of SOFCs currently is their relatively high cost compared to other power generation [5]. By decreasing the operating temperature, a variety of more cost-effective materials could be used for the various parts of the system. One of these components, the interconnect, could transition from the use of ceramics to the use of metallic alloys. However, a new set of problems occurs when transitioning to these metallic alloys. Among them are the need for corrosion resistance and protective oxide formation, while retaining conductivity [3]. Additionally, unwanted secondary phases can precipitate and grow at these lower temperatures, including the brittle sigma phase. Precipitation and growth of this phase must be avoided in order to maintain the properties required for the metallic alloy to properly function in the interconnect environment.

This study focuses on the causes and mechanisms for the nucleation and growth of sigma phase in these metallic alloys. Model ferritic alloys were examined, as well as alloys in the Crofer 22 APU family, which is a commonly used interconnect material. The effect of alloying elements and exposure atmospheres were examined with respect to the oxidation behavior and sigma precipitation and growth in these materials.

2.0 LITERATURE REVIEW

2.1 THE FUEL CELL

A fuel cell is an electrochemical device that can directly convert the chemical energy from a fuel into electrical energy without the need for combustion [3]. It can be considered as a cross between a battery, which converts chemical energy into electrical energy, and a heat engine, which uses a continuous source of fuel and air to run [3,4].

Some of the advantages of fuel cells include high efficiency, lack of moving parts, relatively quiet operation, and low-to-no harmful emissions during operation. Because fuel cells can operate at a range of temperatures, they can be used in a variety of applications such as battery replacement, power for vehicles, or even broad power generation for a grid. All fuel cells are comprised of an electrolyte, either solid or liquid, which has a high ionic conductivity and low electronic conductivity for efficient use, along with an anode and cathode. On either side of the electrolyte is an electrode. For most types of fuel cells, on the cathode side, an oxidant usually in the form of air, is fed to provide molecular oxygen which reduces to form oxygen ions. These ions travel through the electrolyte to the anode side where it can react with hydrogen in the fuel to form water and sometimes heat, releasing electrons to the circuit [3, 5].

The various types of fuel cells can be broken into categories based on the type of electrolyte used (see Figure 2). This thesis will focus on the Solid Oxide Fuel Cell (SOFC) and its components.

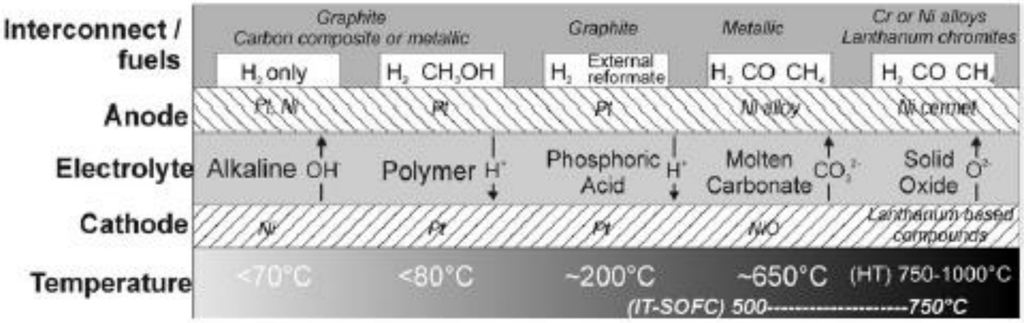

Figure 2. Overview of different fuel cells based on electrolyte type and operating temperature, among other factors [3]

2.2 SOFC

The concept of a SOFC is believed to have been demonstrated first by Bauer and Preis in 1937. However, it wasn't until 1962 when Westinghouse Electric Corporation published a paper called "a solid electrolyte fuel cell" that the first prototypes for SOFC were developed. The paper was the basis for the Westinghouse model of a cathode-supported tubular SOFC, which was produced and tested in several 5 – 250 kW power systems during the 1980's and 1990's. By the mid-1990's, other designs and materials began to be investigated leading to the popular anode-supported planar SOFC design. The biggest drawback of SOFCs currently is their high cost relative to other power generation technology [5].

The main characteristic of a SOFC is its use of a high-temperature solid-oxide electrolyte [7, 8]. Compared to a liquid electrolyte used in other fuel cells, the conductivity of a solid-oxide electrolyte is not as high, and therefore should be kept in the form of a thin film. The activation energy of conductivity is also higher for the solid-oxide electrolytes, which naturally leads into the high operating temperatures of SOFCs, generally between 850 - 1000°C [3, 7]. SOFCs can operate at a temperature higher than the steam reforming temperature, so the heat required for reforming can come directly from the exhaust heat. This leads to a much higher efficiency for the SOFC system, and is considered a major advantage [7]. Another major advantage of the SOFC is its ability to use a variety of gases for fuel, including both hydrogen as well as hydrocarbons [5]. This is advantageous because of the unlikelihood of a broad-distribution hydrogen economy and allows for the use of more abundant resources, such as natural gas in the form of methane, for fuel instead [3, 9]. A single cell typically produces between 1.1 – 1.2 V per cell, but under operating loads, this value can decrease to about 0.6 – 0.9 V per cell. By connecting the cells together in a multi-cell unit, a SOFC stack is created which can obtain higher power. The remaining chemical energy from the process is generally heat, which can be combined with an expander and a gas or steam turbine to increase the fuel and electrical efficiency [9]. This is referred to as a combined heat and power (CHP) system [7].

However, there are also some disadvantages to operating the SOFCs at such high temperatures. One of the major issues is higher thermal stresses which could result from a coefficient of thermal expansion (CTE) mismatch or from volume changes that occur during chemical reactions and the redox cycles. Because of the high operating temperature, large thermal gradients could develop which lead to even more thermal stress conditions. Also, the need for a higher operating temperature will cause a longer start-up and shut-down time. Although there is a longer lifetime expectation associated with the SOFC, since there is minimal liquid-corrosion from a lack of liquid electrolyte, the all-solid design makes it more difficult to construct a stack. Since all the components are solid, it is difficult to get material compatibility between various parts as well as chemical and mechanical stability of all materials used during operation [7]. These issues will be discussed in further detail in subsequent sections.

2.2.1 SOFC Cell Configurations

SOFCs have the ability to be configured in to a variety of shapes which have unique current paths and cell configurations [8]. They can be broadly classified as either self-supported cells, where one of the components of the SOFC is the structural support, or externally-supported cells, where the cell is comprised of thin layers on top of an interconnect or porous substrate. Each design has its advantages and disadvantages (see Table 1) [6, 8]. There are four stack designs for SOFCs which have been proposed and developed: segmented-cell-in-series, monolithic, tubular, and planar or flat-plate.

Segmented-cell-in-series SOFC design consists of segmented cells which are connected in electrical and gas flow series. The cells are arranged as either thin banded structures on porous supports or fitting one-into-another to create a tubular structure. A stack is considered a tube of these cells [8]. Monolithic designs began as a concept at Argonne National Laboratory. The cell components are formed into a corrugated structure of gas coflow or crossflow configurations which are combined in a green state and then co-sintered [6, 8]. It is possible to get a high power density with this design, but the co-sintering fabrication process is very difficult [6].

Table 1. Features of single cell configurations [8]

Cell Configuration	**Advantage**	**Disadvantage**
Self-supporting		
Electrolyte-supported	Relatively strong structural support from dense electrolyte. Less susceptible to failure due to anode reoxidation (Ni/YSZ anode) and cathode reduction (LSM cathode).	Higher resistance due to low electrolyte conductivity. Higher operating temperatures required to minimize electrolyte ohmic losses.
Anode-supported	Highly conductive mode. Lower operating temperature via use of thin electrolytes.	Potential anode reoxidation. Mass transport limited due to anode thickness.
Cathode-Supported	No oxidation issues but potential cathode reduction. Lower operating temperature via use of thin electrolytes.	Lower conductivity. Mass transport limitation due to thick oxides.
External-supported		
Interconnect-supported	Thin cell components for lower operating temperature. Stronger structures from metallic interconnects.	Interconnect oxidation. Flowfield design limitation due to cell support requirement.
Porous substrate	Thin cell components for lower operating temperature. Potential for use of non-cell material for support to improve properties.	Increased complexity due to addition of new materials. Potential electrical shorts with porous metallic substrate due to uneven surface.

Tubular and planar SOFC designs are the two most common-used designs currently. Tubular designs can be made in two sizes: large (diameter > 15 mm) or small (diameter < 5 mm) with a 0.66 – 1 m length [5, 6]. The cell tube is generally made of a porous doped lanthanum manganite created through extrusion and sintering which is closed on one end (see Figure 3). The cell components, a dense yttria-stabilized zirconia (YSZ) electrolyte, porous nickel-YSZ (Ni-YSZ) anode, and doped lanthanum chromite interconnect, are deposited in the form of thin layers onto the tube. The oxidant, air or O_2, is introduced through an alumina injector tube inside the cell. It is discharged near the closed end of the cell and flows towards the open end. Meanwhile, the fuel is flowing on the outside of the cell from the closed end and becomes electrochemically oxidized while flowing to the open end of the cell, creating electricity. At the open end, the oxygen-depleted air leaves the cell and combusts with the partially-depleted fuel. Any remaining depleted fuel is recirculated into the fuel stream again [5].

The biggest advantage of tubular designs is that they do not require high-temperature seals to isolate the oxidant from the fuel which allows for stable performance over long periods of time, on the order of several years. However, the areal power density of a tubular design is much lower than a planar design, and the manufacturing process is more expensive [5].

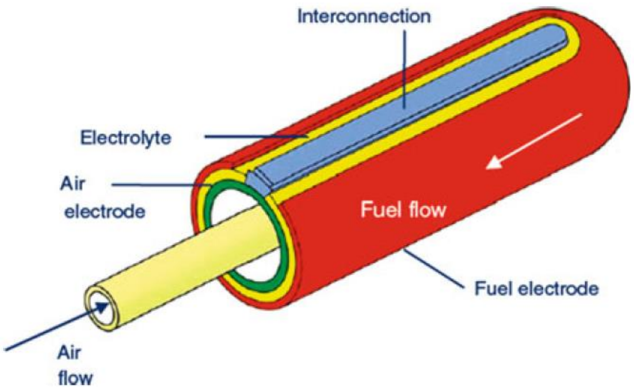

Figure 3. Schematic diagram of a tubular SOFC design [5]

The planar, or flat-plate, SOFC design is comprised of a series of cell components configured as thin, flat plates which are electrically connected to each other [5]. The planar design can use any of the SOFC cell configurations [8]. The plates can either be rectangular/square shaped with the gases being fed from the edges of the cell or circular disks with gases being fed from the central axis. The cell consists of an electrolyte plate sandwiched between an anode and cathode plate. The stack consists of individual cells stacked between interconnect materials, which also regulate the gas flow to the anode and cathode electrodes (see

Figure 4) [5]. The interconnect allows for a coflow, counterflow, or crossflow gas configuration [5, 6]. These components will be discussed in further detail in subsequent sections.

Because of its simple design, the planar configuration is less expensive to manufacture, since the parts can be fabricated separately and joined together afterwards. The planar designs also have a relatively higher power density, 0.5 – 2 $\frac{W}{cm^2}$ for planar compared to 0.2 $\frac{W}{cm^2}$ for a tubular design [8]. However, unlike the tubular design, the planar design requires high-temperature gas-tight seals between components, generally a glass or glass-ceramic [6, 8]. These seals are considered one of the most challenging areas of commercializing the planar SOFC design currently. This thesis will focus on the planar SOFC design and its components, specifically the interconnect material used to create the stacks.

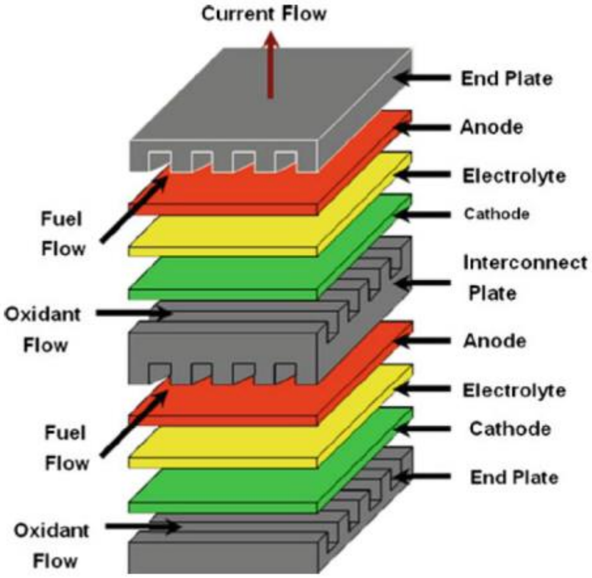

Figure 4. Schematic diagram of a planar SOFC design [5]

2.3 PLANAR SOFC DESIGN COMPONENTS

The four major components of a planar SOFC design are the electrolyte, cathode, anode, and interconnect. As seen in Figure 3, a stack consists of alternating layers of interconnect, anode, electrolyte, and cathode. Due to the high operating temperatures of the cells and the solid nature of the materials, many properties and characteristics must be considered when selecting appropriate materials for each component. These criteria are discussed in detail below.

2.3.1 Electrolyte

The electrolyte is located in the center of a SOFC. Since it is exposed to both an anodic and cathodic environment, its properties have a major impact on the performance of the cell [3]. The major purpose of the electrolyte is to allow the transport of oxygen ions. A good electrolyte material will have good oxygen-ion conductivity at SOFC operating temperatures as well as remaining an ion conductor when exposed to both oxidizing and reducing atmospheres [6]. Other properties that an electrolyte should possess include:

- Low electronic conductivity to provide high energy conversion and minimize ohmic loss [3, 5]
- Good thermal and chemical stability in relation to both environments as well as the contacting electrode materials [3]
- Good CTE match with electrode and contacting components to reduce thermal stresses [3, 5]
- A fully dense structure to maximize conductivity and minimize reactant cross-over
- Simple forming properties so that very thin layers, on the order of a few tens of microns, can be fabricated
- Low cost and environmentally friendly [3]

Electrolyte materials are typically oxides which are able to take low valence element substitutions. The most common materials currently used are doped-zirconia based materials, in particular, yttria-stabilized zirconia (YSZ) [5, 6]. The dopants added to the zirconia stabilize the high temperature tetragonal or cubic crystal structure at room temperature [6]. In the case of YSZ, the zirconia is stabilized in its cubic and tetragonal form allowing for a wide range of operating temperatures without suffering from electronic conductivity and has good chemical and physical stability. The YSZ is typically doped with somewhere between 8 – 10 mol.% yttria. The 8 mol.% provides the YSZ with the best oxide ion conductivity, but the 10 mol.% YSZ has a more stabilized zirconia [3]. Acceptor doped ceria and perovskite structure oxides have also been investigated as possible electrolyte materials [5]. However, its range of operating temperatures is relatively narrow and if the SOFC operates above 650°C, the partial reduction of Ce^{4+} to Ce^{3+} can result in a lattice expansion and lead to microcracking in the electrolyte [3, 5, 6]. The perovskite structure, such as $(La,Sr)(Mg,Ga)O_3$ (LSMG) is promising because of its reasonably good oxide ion conductivity and compatibility with a variety of cathode materials, however there are still many challenges associated with the uncertain cost of gallium sources and its chemical and mechanical stability at SOFC operating temperatures [5].

2.3.2 Cathode

The cathode is where oxygen gas molecules react with incoming electrons, supplied by an external circuit, to form oxide ions [5, 8]. These ions will travel through the cathode and electrolyte to react with fuel on the anode side [3, 5, 6]. Therefore, the most important property of a cathode material is its ability to provide a high catalytic activity for the oxygen dissociation and reduction to take place [10]. Other properties that the cathode should have include:

- High electronic conductivity
- Chemical and dimensional stability in environments of cell fabrication and operation
- Good CTE match with the electrolyte and interconnect [5, 10]
- A stable, porous microstructure so that gaseous oxygen can easily diffuse through the cathode to the cathode/electrolyte interface [3, 5]

Originally, platinum was used as the cathode since other materials were not yet available. However, platinum is expensive and not very cost-effective for making SOFCs. Perovskite-structure oxides were then considered as a cathode material. In 1969, $LaCoO_3$ was tested with an initially good performance, but it was determined that degradation occurred with increasing operating time due to reactions with the YSZ electrolyte. Investigations then moved to lanthanum manganite, $LaMnO_3$, based materials. The degradation for these materials was not as severe, but some potential reactions with the YSZ electrolyte at higher cell fabrication temperatures were acknowledged. Therefore, chemical interactions between the cathode and electrolyte should be avoided during the fabrication process in order to avoid the formation of $La_2Zr_2O_7$. This can be done by creating an A-site(La)-deficient $LaMnO_3$ material [10]. When the lanthanum manganite is doped with low-valence elements, such as calcium or strontium, it has superior p-type electronic conduction from the high concentration of Mn^{4+} in the material [5, 6]. Currently, strontium doped lanthanum manganite (LSM) is the preferred cathode material due to its improved electrical conductivity and CTE match with other SOFC components [6, 10].

2.3.3 Anode

The anode is where the fuel, supplied as either hydrogen gas or a hydrocarbon (ex. methane), is electro-oxidized through a catalyzed reaction [3]. For this reason, the anode material must be an excellent catalyst for the oxidation of the fuel [5]. Other properties it must possess are:

- Stability in a reducing environment, including an atmosphere of hydrogen, hydrocarbons, and products of combustion such as water vapor, CO, and CO_2 [5, 11]
- Electronically conducting so that the electrons can be transported to the external current collector [3, 5]
- Sufficient porosity to allow gaseous species in and out of the electrolyte-anode interface
- Good CTE matching with the electrolyte and interconnect
- Applicability for a variety of fuels, such as hydrogen and hydrocarbons, as well as impurities
- Cost-effectiveness [5]

Early development of SOFCs used precious metals like platinum and gold, or transition metals like iron and nickel as anode materials. However, they did not meet all the requirements necessary for long-term stability under operating conditions [5]. Most anodes now are porous cermets – a mix of ceramics and metals. The microstructure has a fully percolated metallic component which allows for the conduction of electrons. Cermets also optimize the amount of active three phase boundary locations, which are the interface for electronic and ionic conductive phases to exist [3]. The most commonly used anode material is a nickel-YSZ (Ni-YSZ) cermet which is capable of preventing the sintering of nickel particles during fabrication [3, 5, 6]. The use of a Ni-YSZ cermet improves the CTE matching between the electrolyte and current collector [3]. The nickel in the Ni-YSZ is also a good catalyst for the oxidation of hydrogen and helps with the electrical current collection. However, nickel can also promote the formation of carbon when a hydrocarbon fuel is used, so a high steam-to-carbon ratio is necessary in the anode environment to suppress the deposition of carbon [3, 5]. Oxide-based catalysts have been investigated in order to overcome the limitations of nickel-based anodes, but their benefits are counterbalanced by other limitations such as high electrical resistivity and the difficulty of integrating such materials into the currently existing cell and stack fabrication process and materials [5].

2.3.4 Interconnect

The interconnect is the jack of all trades in a SOFC stack. It separates the fuel from the air, collects current from the electrodes, conducts electrical current between layers in the stack, evenly distributes gas across the face of the electrode, and can provide mechanical support to the cell and stack structure [3, 11]. Because the interconnect separates the anode of one cell from the cathode of the next cell, it must be stable in both an oxidizing and reducing atmosphere, especially under thermal cycling [5, 11, 12]. Due to its unique dual exposure, the interconnect has a variety of physical, chemical, and electrical property requirements including:

- Low electrical resistivity (high electrical conductivity) to ensure current collection from the cell
- Good compatibility with other cell components, including a good CTE match with the anode and cathode materials [3, 5, 11]
- Low permeability to reactant gases, which include air, O_2, H_2, hydrocarbons, water vapor, CO, and CO_2 [3, 11]
- Good mechanical properties, especially strength, and corrosion resistance
- Ease and low cost of manufacturability, including ability for a thin and lightweight construction [3, 5, 11]

At high temperatures, the interconnect may be a ceramic, such as doped lanthanum chromite, a high-chromium-nickel metallic, or even a cermet. The use of these materials can be very expensive [3, 5, 6]. Metal interconnects have high electrical and thermal conductivity which minimize temperature gradients and allow for easier fabrication, but their corrosion resistant layers and CTE mismatch are generally much larger [6]. Metallic interconnects are considered more robust, especially if they are able to form a protective layer which slows corrosion and prevents volatilization of species [3]. However, these protective oxide layers can have a higher electrical resistivity which lowers the efficiency of the cell. Chromia is considered the best protective scale for interconnect materials since it has a lower resistivity than alumina and silica, although it grows faster [11]. For this reason, iron-chromium (Fe-Cr) stainless steels are a popular interconnect choice. They also have high strength, good machinability, a good CTE match with both the anode and cathode, and are relatively low cost [3, 11, 12]. In recent years, a number of steels have been developed specifically for use as interconnect materials in SOFC systems at slightly lower temperatures [13]. This will be discussed in detail in further sections.

2.4 INTERMEDIATE TEMPERATURE SOFC (IT-SOFC)

Although SOFCs are considered high temperature systems which normally operate around 850 - 1000°C, there has been a significant effort to lower the operating temperature to an intermediate range of 600 - 800°C [3]. Because the operating temperature would be lower, a greater variety of materials could be used in the fabrication of the SOFC which would help provide a more cost-effective system, more rapid start-up and shut-down, reduced corrosion rate of products, improved ductility and construction, and simplified system requirements [3, 5, 6]. Along with these properties, a lower operating temperature could actually increase the theoretical maximum efficiency of the SOFC stack (see Figure 5) [3, 6]. The efficiency can also be improved at these lower temperatures by reducing the thickness of the electrolyte, which reduces its resistivity, or choosing new materials with better ionic conductivity and electrode performance [3].

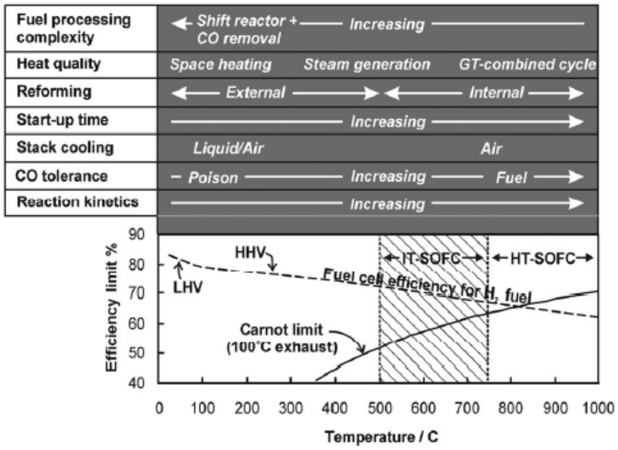

Figure 5. Summary of fuel cell issues in comparison with operating temperature [3]

One of the major focuses of the IT-SOFCs is their ability to use a wider range of materials for fabrication, specially the interconnect. Because of the lower operating temperature, metallic materials can be used for the interconnect instead of a ceramic [3, 6]. However, at this lower temperature range, an additional set of property requirements is created which includes:

- Resistance to surface oxidation and corrosion in both anode and cathode atmospheres
- The creation of an oxide protective layer which can provide resistance to surface oxidation and corrosion while maintaining slow growth kinetics, sufficient electrical conductivity, strong adhesion to the alloy in thermal cycling, and good chemical compatibility with the electrodes [3]

Metallic materials for interconnects are still a popular choice due to their improved ductility and increased ease and reduced cost of fabrication for use in IT-SOFCs [12]. At a lower operating temperature, there is more leniency with the CTE mismatch between the interconnect and electrodes. This would allow for the interconnect thickness to be reduced from a few millimeters thickness to a few tenths of a millimeter, which would help reduce stack weight and cost [14]. Currently, high-chromium ferritic steels are under consideration for use as interconnect materials for IT-SOFCs. However, they have a poor creep resistance for the operating range of 700 - 900°C, which is an issue when the interconnect is very thin [15]. Austenitic stainless steels have been considered as well. They possess increased ductility and creep resistance, but also have a higher amount of CTE mismatch [14]. This thesis will mainly focus on the Fe-Cr ferritic stainless steels.

2.5 FE-CR SYSTEM

The Fe-Cr system contains three solid phases: a ferritic alpha phase, an austenitic gamma phase, and a sigma phase (see Figure 6). Ferritic stainless steels are steels which are mainly comprised of the body-centered cubic (bcc) alpha phase. At lower temperatures, the face-centered cubic gamma phase is unstable and therefore unlikely to be seen below about 850°C. The sigma phase is considered an intermetallic phase which has no definite stoichiometric composition [16]. Many properties and mechanisms for this phase are still relatively unknown and merit further discussion.

2.5.1 Sigma Phase

The Fe-Cr system was the first system in which sigma phase was suggested to exist in the early 1900’s [16]. However, its true discovery came in 1927 when Bain and Griffiths found a hard, brittle, non-magnetic phase in Fe-Cr-Ni alloys which they dubbed “B constituent” [18]. Its official name as sigma phase was given by Jette and Foote almost a decade later [19]. As can be seen in Figure 6, the maximum limit of formation is roughly 820°C, with a low limit existing around 520°C although it has been reported to exist as low as 460°C [16]. Below this temperature, the sigma phase undergoes a eutectoid transformation into the alpha and alpha prime phases.

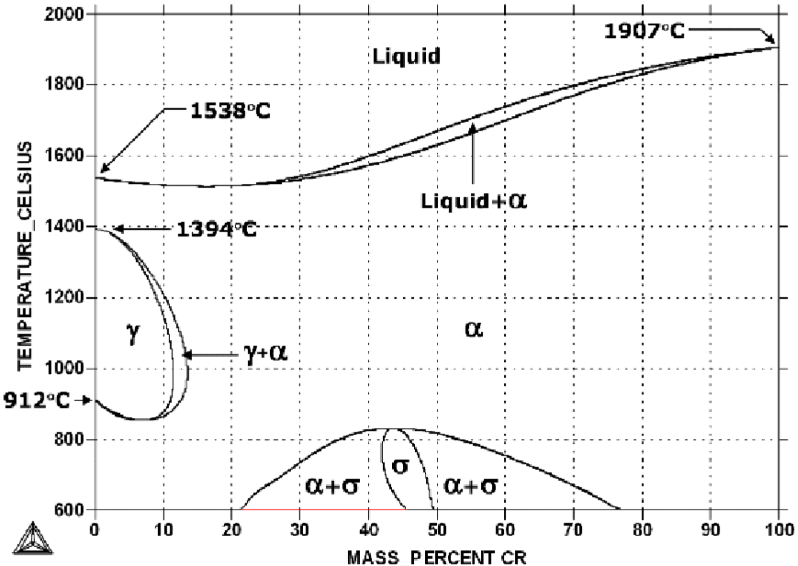

Figure 6. Calphad Model of the Fe-Cr system [17]

The sigma phase is a brittle phase, possessing a hardness almost 3 – 4 times higher than alpha, that is very hard to characterize. There is difficulty in determining its phase boundaries in terms of temperature and composition due to the slowness of transformation, purity required in the alloy tested, dependence on the mechanical state of the alloy, and the temperature at which the alloy is annealed [16]. The crystal structure was determined to be a $D\frac{14}{4h}$ structural spacegroup containing 30 atoms in the unit cell that have mixed occupation at all atomic sites (see Figure 7) [20]. The unit cell can be described as two pseudo-hexagonal layers of atoms which are located half a unit cell apart. The hexagonal close-packed (HCP) net of the sigma phase can be fitted into a tetragonal cell with only a small amount of distortion, and so the sigma phase can sometimes be referred to as a tetragonal-type crystal structure [16, 20]. The atoms in the cell are distributed over five sites, labeled A through E, which are all different due to different occupation numbers, coordination numbers, volume available around each site, and their symmetry. Because the sites, like the cell, are disordered, the actual occupation numbers depend on the composition of the alloy possessing the sigma phase [16].

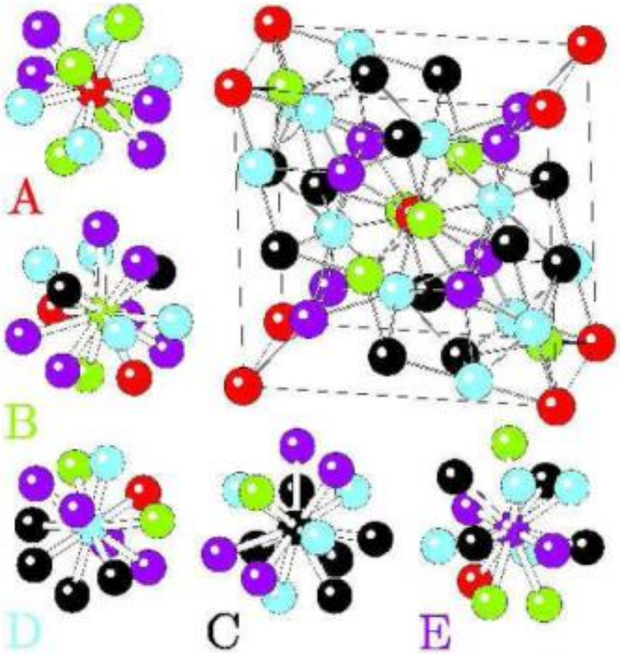

Figure 7. Unit cell configuration of sigma phase and its five sub-lattices [16]

Because the presence of even a small amount of sigma can drastically degrade many properties in a ferritic material, the ability to detect the phase is important [16]. The brittleness of sigma is the most discussed characteristic of the phase, but not the easiest way to identify it in a material. The phase is also technically non-magnetic, although at very low temperatures, near 113°C, it has been found to be ferromagnetic [20]. Because of these issues, an XRD pattern of sigma is usually the easiest way to confirm presence of the phase in a material (see Figure 8) [16]. The pattern has a group of eight strong lines with spacings close to 2Å and a few weaker lines at larger spacings, near 1.8 – 1.3 Å. Because the peaks are so close to each other, a powder diffraction pattern of sigma is often difficult to interpret [20].

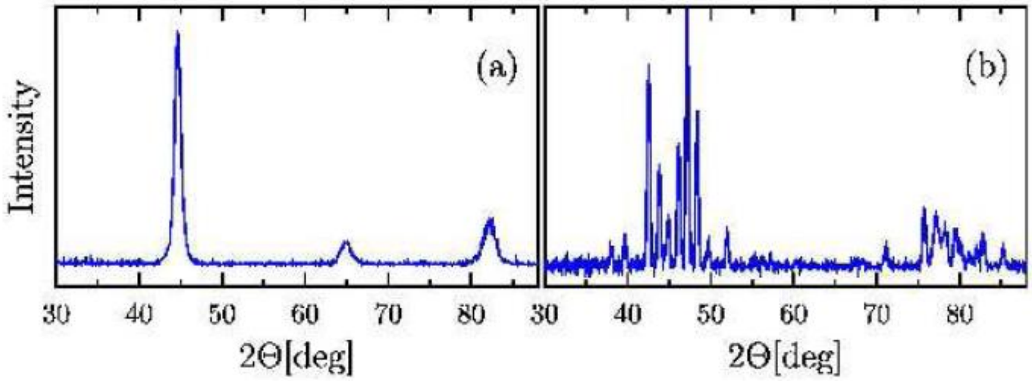

Figure 8. XRD patterns of alpha phase (a) and alpha plus sigma phase (b) [16]

Although the kinetics of sigma phase formation are known to be slow, there have been many attempts to study the way in which the phase nucleates and grows in a material. It has been determined that the alpha to sigma transformation kinetics curve is S-shaped, characteristic of a nucleation and growth process which consists of three distinct phases: an incubation period, a nucleation period, and a growth period. The incubation time and growth time are both slow whereas the nucleation period can be quite fast. In particular, the incubation time is dependent on the annealing temperature and composition of the Fe-Cr alloy. It was also seen that precipitation of sigma in mechanically alloyed samples was higher than that of identical composition samples which were created through a melting process. It is theorized that the higher fraction of grain boundaries in the mechanically alloyed sample provided additional nucleation sites for the precipitation of sigma [16].

2.6 FE-CR ALLOYS AS INTERCONNECTS

Metallics are a popular choice for interconnect materials because of many properties previously mentioned. The interconnect needs to be impermeable to both the anode and cathode environment gases, and it is easier to get to full density with a metallic compared to a ceramic. Metallics can also be excellent electronic conductors which minimizes their internal resistance. Since they have good thermal conductivity, they also reduce a temperature gradient and minimize the need for a strong CTE match between the interconnect and other components. However, almost every metallic that is exposed to anode and cathode gas at a SOFC operating temperature will form a layer, or multiple layers, of protective oxides [11, 21]. Reactions between the interconnect material and the anode or cathode environments can also lead to the formation of other phases below the oxide layer, which could increase the electrical resistance or even lead to a reduction of mechanical properties and cause degradation of the SOFC [12].

Minor alloying elements are added to the Fe-Cr binary to improve its properties in SOFC environments. Manganese is often added to create a chromium-manganese spinel above the chromia layer, to prevent volatilization. Silicon and aluminum are commonly added to alloys to help reduce the level of oxygen in the melt during fabrication, although their levels should be kept low to prevent the formation of silica or alumina. Tungsten can be added to help improve the hardness of a material, while niobium additions can improve the strength. Lanthanum can help slow the growth of the chromia scale and improve the adherence of the scale to the base alloy. Small amounts of titanium can be used as a carbide stabilizer and to help reduce chromia evaporation [11]. Even minor additions of reactive elements, such as yttrium, hafnium, or cerium, will help improve the adherence of the chromia scale to the base alloy. These elements can also reduce the growth rate of the oxide, decrease the amount of transient oxidation, decrease the overall oxide grain size, and can alter transport mechanisms through the oxide. Although the effects of these elements are known, their specific mechanisms for causing such reactions are not [22]. In recent years, knowledge of the effect of these elements has led to the development of new steels specifically created for use as interconnects, such as Crofer 22 APU and ZMG 232 [13].

2.6.1 Chromia Oxide Layer

As mentioned earlier, the oxide layer that forms on the metallic interconnect must have relatively slow growth in both the anode and cathode environment. This is because the oxide layer, which protects the underlying alloy from further corrosion or degradation, generally has a much higher electrical resistivity compared to the alloy. This large resistance in the oxide can not only cause a drop in the efficiency of the SOFC stack, but could also cause premature failure of the stack before its projected lifetime. For these reasons, the oxide scale should also be strongly adherent to the underlying alloy as well as homogeneous in structure and thickness. If it has the ability to be a good electronic conductor, especially at SOFC operating temperatures, this is ideal [3, 21].

One of the ways to compare the electrical resistance of the various oxide layers that can be formed is the area-specific resistance (ASR) value. The ASR is a normalized value determined by the product of the electrical resistivity of the oxide layer and its thickness. Therefore, as the oxide scale thickens, the ASR value also increases. An ideal interconnect material will have an ASR value of its oxide below 0.10 $\Omega\cdot\text{cm}^2$ [12, 21]. The three types of alloys generally considered for interconnect use are alumina formers, silica formers, and chromia formers. These oxides are considered protective and help prevent further degradation of the alloy from which they are formed. However, in terms of ASR, only chromia is feasible for interconnect use. Both alumina and silica are highly resistive, with ASR values at 800°C ranging from 10^4 – 10^6 times higher than chromia [11]. Nickel-based alloys are also being considered, although their ASR value parabolically increases with time due to scale thickness. However, the nickel oxide scale is a semiconductor which helps to keep the ASR from increasing too rapidly (see Figure 9) [12]. Currently, Fe-Cr ferritic steels with a chromium content around 22 – 26 wt.% are in the target range for ASR values. The ASR value can be further reduced by increasing the chromium content with very little variance based on temperature. It has also been seen that after 7000 – 15000 hours of operation, ASR values become worse when the material is alloyed with molybdenum and better if the material has some niobium [12].

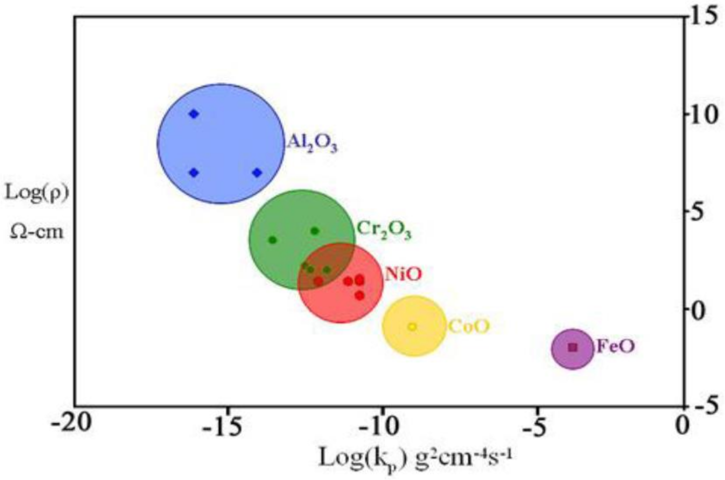

Figure 9. Resistivity verses growth rate for selected oxides [23]

Another reason that chromia formers are an ideal interconnect material is because the CTE of Fe-Cr alloys and chromium-based alloys are the closest to the YSZ-based anode of a SOFC. Generally speaking, the metallic interconnect should have a CTE that is slightly higher than the ceramic to which it is attached. This is especially important at higher temperatures where the CTE match should be as close as possible to avoid thermal stresses from thermal cycling caused by start-up and shut-down [12]. The problem with chromia-forming alloys is the reactive evaporation (volatilization) of the chromia scales, which is a significant issue at both high temperatures and high oxygen partial pressures [5, 11]. The cathode of the SOFC is usually fed with air which has a relatively high oxygen partial pressure. At the cathode side, the chromia scale could react with the oxygen to form gaseous chromium trioxide (see Reaction 1). Initially, diffusion of chromium through the chromia scale is rapid and so the effect of volatilization is not so significant. However, as the thickness of the scale increases, the volatilization rate becomes comparable, and then equal to, the diffusive growth rate. It has been seen that a water vapor content of about 0.1% in air could result in volatilization due to an increase in the oxygen partial pressure, which is why it is very important to keep the cathode gas atmosphere as dry as possible [11].

$$Cr_2O_3(s) + \frac{3}{2}O_2\,(g) = 2CrO_3(g) \qquad (1)$$

Other issues include the formation of chromium-containing species at the electrolyte/cathode interface which could lead to a poisoning of the cathode. Deposits of chromium onto the electrolyte and cathode interface cause a rapid deterioration of the cathodes oxygen reduction rate, which further reduces the efficiency of the SOFC. Mechanisms for this breakdown are still unknown, although some theories have been suggested. Methods to reduce chromia evaporation from the scale include various types of coatings and growth of other layers, such as a manganese-chromium spinel, above the chromia layer [5, 11].

2.6.2 Anodic Environments

In the SOFC system, the anode environment is usually comprised of hydrogen or hydrocarbons, along with products of oxidation, such as water, CO, and CO_2 [5, 11]. The key point of the atmosphere is that the oxygen partial pressure should be very low. A commonly tested anode environment is argon with 4% hydrogen and a small range (generally 2 – 4 %) of water vapor. Sometimes a nitrogen-hydrogen-combustion product mix will be used to simulate gasoline fuel [14].

At 600°C, a variety of ferritic steels with a chromium-content ranging from 16 – 25% showed excellent oxidation resistance up to 1000h. Most of the alloys formed a protective inner chromia layer with an outer Cr,Mn spinel. It was determined that alloys with a higher chromium content showed better oxidation resistance. Also, an increase in the molybdenum content improved the mechanical properties of the alloy, but also had a drawback of increasing embrittlement through the precipitation of sigma phase, Laves phase, or T-1 phase [14]. Increasing the anode temperature to 900°C caused a slightly different reaction. When a ferritic alloy with 26 wt.% chromium was tested, it was shown to still possess an external chromia scale, but with an internal distribution of aluminum-rich precipitates just below the scale. There was also a substantial amount of silica at the alloy-scale interface. When Crofer 22 APU, a ferritic alloy with about 22 wt.% chromium, was tested there was very little Mn,Cr spinel observed on the outer surface and the chromia scale seemed friable underneath the spinel [11].

2.6.3 Cathodic Environments

The oxidant supplied to a cathode is generally air, although it can also be supplied as pure oxygen [5, 8]. One main problem of the ferritic stainless steels in the cathode environment is the volatilization of the chromia layer. In a cathode gas, the CrO_3 partial pressure increases as the oxygen partial pressure increases. Analysis of oxide evaporation has shown that a water content above 0.1% in air will cause evaporation of the chromia layer. For this reason, it is very important to keep the cathode gas as dry as possible. Two commonly tested cathode atmospheres are dry air, and dry air with some small percent of water vapor [11].

The difference between dry air and wet air can have a huge impact on the oxidation behavior of the alloys. When Crofer22 APU was exposed to dry air at 900°C, it was observed to have a continuous Mn,Cr spinel outer layer with an internal chromia layer beneath it. However, in an air environment with 10% water vapor, the spinel layer turned into discontinuous particles on top of a chromia layer, which only provides partial protection. When a Fe-26Cr alloy was tested in the same wet air environment, its chromia scale had excessive spallation [11]. While the chromia content itself does not have a significant effect on the oxide formation in the cathode atmosphere, it can influence the relative fraction of the types of oxide phases that are formed [24]. Another issue with the wet air atmospheres is that it can cause rapid scale growth which will reduce the efficiency of the SOFC. By lowering the temperature, for example to 700°C, the growth rate of the oxide can be lowered. However, this can lead to the formation of other unwanted phases, such as sigma [11].

2.6.4 Sigma Transformation during SOFC Operation

When the operating temperature is lowered from above 850°C into an intermediate range of 500 - 750°C, sigma formation can begin to occur based on the Fe-Cr phase diagram (see Figure 6) [17]. Normally, this would not be an issue, as sigma is slow to nucleate and grow in a traditional Fe-Cr binary alloy [16]. However, in the case of SOFCs, the lengthy operating lifetime of almost 40,000 hours can allow for sigma nucleation and growth [21]. Furthermore, the other alloying elements in the interconnect materials can have an effect of the rate of the sigma nucleation and growth.

There is a suggestion that sigma phase nucleation requires high-energy interfaces, such as high angle grain boundaries, incoherent twin boundaries, or high-energy interfaces of second phases in order to nucleate [25]. In ferritic alloys with a composition of Fe – 40 wt.% Cr or Fe – 45 wt.% Cr, sigma phase tends to nucleate first at the external surface of the alloy, and then grows inward. In a ferritic alloy with a Fe – 50 wt.% Cr, the sigma phase nucleated first at the external surface of the alloy at grain boundaries and then grew inward along grain boundaries [26]. In austenitic alloys, sigma phase tends to nucleate first at the external triple points, then grain boundaries, then incoherent twin boundaries, and finally intragranularly at oxide inclusion locations. In the case of intragranular precipitation, sigma cannot nucleate alone, but still requires some sort of high-energy interface [27].

In duplex stainless steels comprised of almost even amounts of ferrite and austenite, nucleation of sigma phase occurred preferentially at ferrite-austenite interfaces. In this case, sigma growth was related to the consumption of the ferrite phase [28]. Alternatively, in the case of austenitic stainless steels, particularly alloy 310, sigma phase formed as a direct transformation of austenite into sigma. In this case, austenitic stainless steels were exposed to high temperature liquid sodium which caused a depletion zone rich in iron under the surface of the alloy. Sigma nucleation was primarily restricted to the boundary of the depletion zone and the austenite zone. Even when the alloys were isothermally aged, the sigma phase formation kinetics were the same, although there was no formation of the depletion zone rich in iron [29]. The transformation of austenite into sigma has also been in the multipass heat affect and fusion zones of austenitic steels [30].

It has also been seen that cold working prior to aging a material will cause an increase in the sigma phase formation. When austenitic stainless steel is less than 20% cold worked, the sigma particles tend to nucleate mostly at the deformation faults [27]. Depending on the alloying elements in the steel, the volume fraction of the sigma fraction can vary. For the 316 alloy in a 20% cold-worked state, there was 13 vol.% sigma phase. However, in the 310 alloy, which had a slightly lower iron content, and slightly higher chromium and nickel, there was almost 30 vol.% sigma phase formed [29].

One element that is a known sigma promoter is molybdenum [31]. Molybdenum is often used to increase the mechanical properties of a material as well as improving the ASR value for interconnect use [12, 14]. When austenitic steels, with a chromium content of about 25 wt.% and a nickel content of about 20 wt.%, were examined, sigma content increased with increasing molybdenum content, although there was a certain saturation point for the volume. As the molybdenum content increased, the chromium content in the sigma phase was also decreasing. This is because the chromium atoms in the sigma phase were being replaced by molybdenum atoms and the iron and nickel atoms remained fairly constant [31].

Since certain elements can have an effect on sigma formation, purity of the alloy being used becomes important. When a low-purity Fe-50Cr alloy was compared with a high-purity alloy in the same testing conditions, the low purity alloy had sigma precipitation while the high-purity alloy did not. Carbon was determined not to have an effect on sigma formation because it cannot dissolve into the ferrite phase and instead precipitate out [32]. When the amount of nitrogen in the alloy was reduced, the formation of sigma phase could be suppressed [33]. However, silicon can dissolve significantly into the ferrite phase and therefore has some effect on the precipitation of sigma phase. It could be due to a lattice strain causes by the silicon atoms in the ferrite phase, which would have a similar effect to coldworking on the material. When 4 wt.% tungsten is put into an Fe-30Cr alloy, no sigma phase was formed. This could be due to the smaller strain of tungsten compared to silicon which would not cause enough of a mismatch for the sigma phase to nucleate [32]. Therefore, elements which can dissolve easily into ferrite and which can cause a large lattice strain should be avoided to prevent sigma phase formation at lower temperatures.

The environment in which a material is exposed will also have an effect on the sigma phase formation. When Fe-26Cr alloys were tested, various environments caused different amounts of sigma to nucleate and grow. In a dry air, cathodic environment, sigma was seen to penetrate only about 50 microns into the sample from the edge. However, in a wet air (10% water vapor) cathodic environment and in a simulated anode environment, sigma was seen to penetrate completely to the center of a 1mm thick sample. Out of all three environments, the wet air environment had the largest volume fraction of sigma phase [11].

Interdiffusion is a more recently identified problem associated with sigma formation. One particular area of interest is the effect of the nickel from the mesh on the anode side of the SOFC touching the metallic interconnect. To determine this effect, a variety of ferritic and austenitic stainless steels were electroplated with a thin layer of nickel and then exposed to a simulated anode environment. In all cases, an interdiffusion zone was created due to the migration of elements, mainly iron and chromium (see Figure 10). In the ferritic steels, a layer of austenite was formed due to this interdiffusion [13].

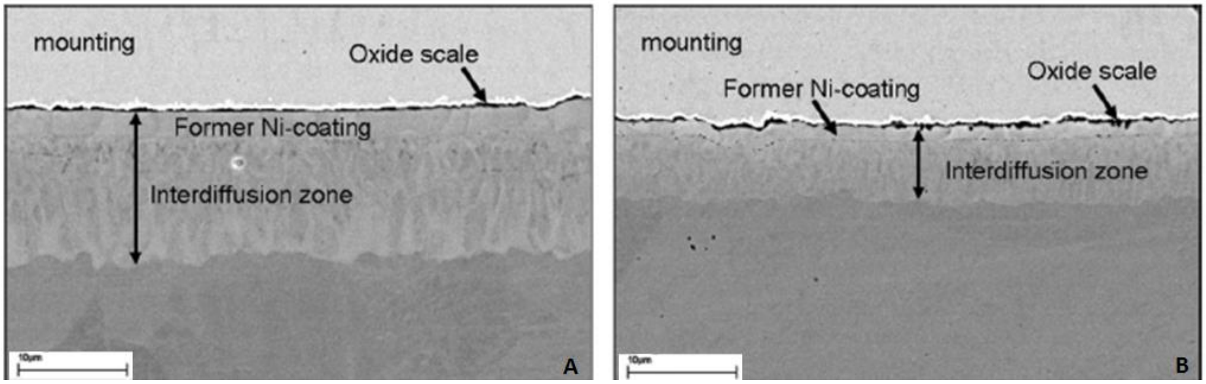

Figure 10. SEM-BSE images of cross-sectioned nickel-coated Fe-22.7Cr ferritic steel (A) and Fe-17.3Cr ferritic steel (B) [13]

The most interesting result, however, is the formation of sigma phase in the Fe-22.7Cr ferritic steel due to the interdiffusion zone (see Figure 11). It can be seen that the presence of the nickel layer before exposure promotes a phase change from ferrite to austenite, and in certain cases, from austenite to sigma [13]. When the same materials were tested in the same conditions without the pre-coated layer of nickel, no sigma formation was observed; therefore the effect is clearly due to the nickel layer [13, 14].

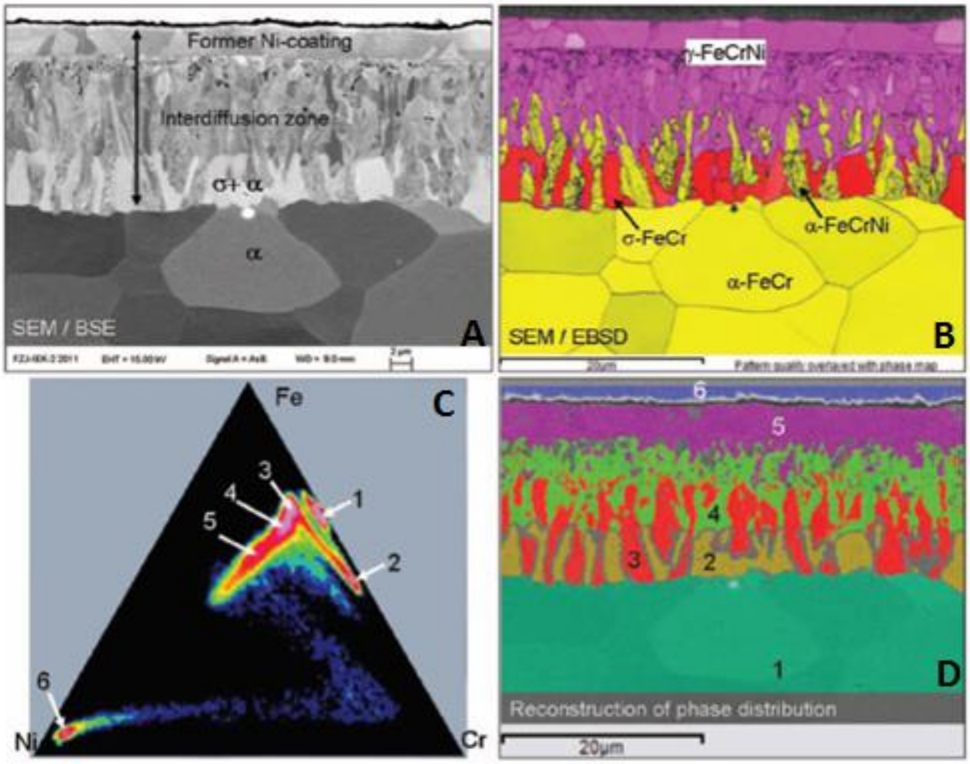

Figure 11. SEM-BSE (A), SEM-EBSD (B) images and reconstruction (D) of phase distribution from EDX mapping on a cross-section of Ni-coated Fe-22.7Cr ferritic steel. The sides of the Fe-Cr-Ni triangle (C) correspond to intensities of Kα lines of Fe, Cr, and Ni collected by EDX mapping [13]

As can be seen by the images, the commonly used nickel mesh in the SOFC design is promoting phase transformations which lead to a degradation of material performance, especially in the metallic interconnect. Additionally, the formation of these phases, along with other precipitates, can pull chromium from the alloy causing the oxidation resistance of the overall material to decrease due to the inability to form a protective chromia scale. The use of a higher carbon-content steel could prevent sigma formation due to the slower diffusion of carbon through the austenite phase and lack of ability to be dissolved into the austenite phase [13, 32].

3.0 RESEARCH OBJECTIVES

The use of metallic alloys for interconnect material is currently being investigated and implemented for certain SOFC designs. In order to increase efficiency and lifetime while decreasing degradation, there has been a push to lower the operating temperature from a high range to an intermediate range. However, these intermediate range temperatures can lead to new problems with the metallic interconnect.

Currently, the alloy of choice for interconnect materials in IT-SOFCs is a ferritic stainless steel. When exposed to an IT- SOFC operating environment, precipitation and growth of the intermetallic sigma phase can occur. Presence of this phase will degrade the properties of the alloy needed to properly function as an interconnect. Although some properties and mechanisms for sigma phase nucleation and growth are known, there is still much to be learned with regard to the SOFC environment. The first goal of the research is to determine the effect of alloying elements on the precipitation and growth of sigma phase. The second goal of the research is to determine the effect of various SOFC atmospheres on the nucleation and growth of the sigma phase.

The planar SOFC design involves the use of a nickel mesh between the interconnect and the anode side of the cell. Recently, it has been observed that exposure at operating temperatures can cause interdiffusion of the nickel from the mesh and the interconnect alloy, leading to precipitation and growth of sigma phase. Very little about this effect is understood. The third goal of this research is to understand the effect of the nickel contact and the mechanism by which sigma phase is able to nucleate and grow in the presence of this diffusion zone.

4.0 EXPERIMENTAL PROCEDURE

4.1 MATERIALS TESTED

Both model alloys and commercial alloys were tested. The model alloys consisted of an iron-chromium binary alloy with several alloying elements. The commercial alloys consisted mostly of ferritic stainless steels with Crofer® 22APU as a starting point. Crofer® 22H, a commercial stainless steel, was also tested. Additionally, one austenitic stainless steel was tested. The specific alloy compositions are listed below in Table 2.

The MPS, MPT, and MPU alloys were received as circular disk specimens, with a thickness of about 1mm and a diameter of about 12mm. The other five alloys (KMT, KST, KDN, MEC, LKC) were received as rectangular coupons with thickness ranging from 1mm – 2mm and a specimen size of 1cm x 2cm. The round specimens were ground to a two-grit finish. One circular face was ground to a 600 grit SiC finish ("coarse") and the opposite face was ground to a 1200 SiC finish ("fine"). The edge was ground to a 600grit SiC finish. The rectangular specimens were all ground to a 600 grit SiC finish. All specimens were cleaned with ethanol before exposure, then dried, measured and weighed before any testing was performed.

Table 2. Alloy Compositions (wt. %)

Alloy (Code)	Fe	Cr	Mn	W	Nb	Si	Ti	La	Ni	Mo	Other (Al, C, N, O, S, P)
MPS	Bal.	30	--	--	--	--	--	--	--	--	--
MPT	Bal.	30	2	--	--	--	--	--	--	--	--
MPU	Bal.	30	--	--	--	--	--	--	--	2	--
Crofer® 22APU (KMT)	Bal.	21.8	0.38	--	--	0.02	0.075	0.06	0.019	--	0.01Al 0.0008C 0.0035N 0.0054O 0.003S 0.009P
Crofer® 22APU+Nb,Si (KST)	Bal.	22.2	0.46	--	1.03	0.25	0.09	0.16	<0.01	--	0.01Al 0.011C 0.014N 0.004O 0.002S 0.003P
Crofer® 22APU+W (KDN)	Bal.	20.65	0.53	2.62	0.01	0.038	0.11	0.13	0.01	--	0.01Al 0.002C 0.006N 0.005O 0.002S 0.01P
Crofer® 22H (MEC)	Bal.	22.93	0.43	1.94	0.51	0.21	0.07	0.08	0.28	--	0.02Al 0.007C 0.015N 0.0056O 0.002S 0.014P
LKC	Bal.	17.3	0.43	--	0.42	0.35	0.12	--	0.20	0.02	0.02Al

Some specimens (MPS, KMT, KST, KDN, MEC, LKC) also received an electroplated layer of nickel. Before coating, specimens were cleaned and washed in a 15% aqueous HCl solution and water, for 10 seconds each respectively. They were then attached to an electrode and lowered into a beaker containing constantly mixing nickel-plating solution, comprised of 90g $NiSO_4 \cdot 6H_2O$ + 6.4g KCl + 38g NH_3SO_4 in 750 mL of H_2O, which was held at a constant temperature of 60°C. A solid metallic nickel plate was wrapped around the inside of the beaker with an edge which could be attached to the second electrode (see Figure 12).

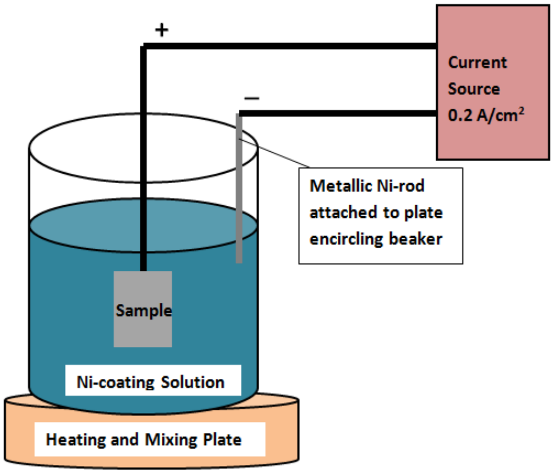

Figure 12. Schematic diagram of nickel coating procedure

A constant current density of 0.2 $\frac{A}{cm^2}$ is applied for 10 – 30 minutes, depending on the size of the specimen, to ensure an even layer of nickel plating is achieved. After plating, specimens were removed from the bath, dried, and measured and weighed before any testing was performed.

4.2 CATHODE ENVIRONMENT TESTS

The MPS, MPT, and MPU alloys were tested in two SOFC cathode environments. The first environment was a dry air environment, and the second simulated a seal-leak or “wet air” environment of dry air with 10% water vapor. The water vapor was established by running dry air through two heated beakers of water. The first beaker contained water held at a temperature of 55 – 60°C. The wet air then travelled through a second beaker containing water held at a temperature of about 46°C which provides 10% water vapor at standard pressure. This air then travelled through the furnace where the specimens were being exposed.

Specimens for the wet air environment were placed in an alumina crucible which was inserted into a horizontal furnace manually through the use of a magnet. The magnet was used to push a quartz rod, to which the crucible was attached, into the hot zone. The hot zone was maintained at 700°C ± 10°C. Specimens for the dry air environment were hung on a platinum wire placed inside a vertical quartz tube. A vertical furnace was manually raised until the specimens were located inside the hot zone, which was also maintained at 700°C ± 10°C. The gas atmosphere, either dry air or wet air, was flowing at a constant rate of $60\frac{mL}{min}$. After exiting the furnace, the gas was bubbled through water to ensure proper flow through the furnace and hot zone. A variety of exposure times were tested on the three alloys (see Table 3).

Table 3. Testing times for alloys in cathodic environments (hrs)

Alloy (Code)	Dry Air	Air + 10% H_2O
MPS	500	500
MPT	500	500
MPU	22, 220, 362, 500	500

4.3 ANODE ENVIRONMENT TESTS

All alloys except MPT and MPU were tested in the anode environment. The gas mixture used for the anode environment was Ar-4%H_2. Water vapor was introduced into this environment, as with the cathode environment, to create a gas mixture of Ar-4%H_2-10%H_2O. All specimens were exposed in a horizontal furnace, loaded in a similar fashion to the cathode environments. The hot zone was maintained at 700°C ± 10°C and the gas was flowing at a constant rate of $60\frac{mL}{min}$. The alloys were tested in the anode environment for a range of exposure times (see Table 4). One set of specimens was not coated with a nickel-layer.

Table 4. Testing times for alloys in anodic environment (hrs)

Alloy (Code)	With Ni-layer pre-exposure	No Ni-layer pre-exposure
LKC	22, 220	220
KMT	22, 220	220
KST	22, 220	220
KDN	22, 220	220
MEC	22, 220, 500	220, 500
MPS	500	500

4.4 ANALYTICAL PROCEDURE

After exposure, the specimens were weighed and the thickness measured in order to determine the weight change as a function of time. Characterization was performed through the use of Scanning Electron Microscopy (SEM), X-Ray Diffraction (XRD), Optical Metallography, and Sputtered Neutrals Mass Spectrometry (SNMS).

4.4.1 X-Ray Diffraction

XRD patterns for all cathodic environment specimens were obtained using a Philips PW3710 Diffractometer with a CuKα radiation (λ = 1.54056). Two different equipment settings were used to obtain information about the diffraction patterns of the peaks (see Table 5).

Table 5. XRD Scan Settings

Scan Name	2θ range	Step Size	Dwell Time
Full	20° – 90°	0.05°	0.25s
Sigma	23° – 70°	0.01°	0.75s

4.4.2 Optical Microscopy and Scanning Electron Microscopy

After cathodic exposure, all specimen surfaces and any oxide formations were examined through the use of a JEOL JSM-6610LV SEM equipped with secondary electron (SE), backscatter electron (BSE), and energy dispersive spectroscopic (EDS) analysis. The surfaces of anodic environment specimens which were not pre-coated with a nickel layer were also analyzed through the use of a Zeiss Supra 50 VP SEM equipped with SE, BSE, and EDS.

After SEM investigation, all anodic environment specimens were cut into two pieces using an automatic saw. One piece of the specimen was roughly $\frac{1}{3}$ of the original specimen size, and the other piece was roughly $\frac{2}{3}$ of the original specimen size. The $\frac{2}{3}$ piece was coated with a thin gold layer through sputtering to preserve the sample surface, after which it was coated with a nickel layer through the use of the nickel bath described above. After this coating, the specimens were cold mounted in an epoxy. The cathodic environment specimens were directly mounted into the epoxy without the gold and nickel layers. The cross-sections of all specimens were polished and prepared for analysis.

Optical micrographs of specimen cross-sections were taken with either a Keyence VHX-600 digital optical microscope. Micrographs of the anodic environment specimens which had been pre-coated with nickel were taken before the application of any etch. An electrolytic etch was used on all cathodic environment samples as well as all anodic environment samples which had been pre-coated with a layer of nickel. Additionally, the electrolytic etch was used on the MPS and MEC samples which were exposed for 500 hours without a pre-coated layer of nickel. The etching solution was a 10% aqueous KOH solution which was electrolytically applied for 5s at a constant voltage of 1.5V. After etching, specimen cross-sections were carefully rinsed in water and then ethanol to ensure cleanliness and preservation of the etched surface before observation. Specimens were again observed with the digital microscopes and optical micrographs were taken.

After etching, specimen cross-sections were again polished and prepared for additional analysis. Cross-sections of all cathodic specimens and all anodic specimens which had been pre-coated with a layer of nickel were observed on the SEM. Prior to observation, specimen surfaces were coated with a thin layer of palladium to ensure conductivity. Compositional analysis of any oxide formation, interdiffusion zone, and precipitation of particles and phases were performed using the Inca EDS program on the JEOL SEM. SEM micrographs were taken in the BSE mode.

Some specimens were also prepared for Electron Backscattered Diffraction (EBSD) analysis. For these specimens, additional polishing was performed for two hours using a VibroMet® polisher containing a 1 micron colloidal alumina polishing solution. After polishing, the sample cross-section was washed with soap and water multiple times to ensure removal of all polishing solution and particles. EBSD analysis was performed through the use of a Phillips XL-30 Field Emission Gun SEM, which was also equipped with SE, BSE, and EDS. Analysis of the EBSD patterns was performed with Orientation Imaging Microscopy (OIM) Data Collection and Analysis Software.

4.4.3 Sputtered Neutrals Mass Spectrometry

SNMS was performed on two anodic samples: MEC with and without a pre-coated nickel layer exposed for 500 hours. The analysis was used to characterize the oxide scales and determine the composition of various elements through the thickness of the reaction layer into the base alloy.

5.0 RESULTS AND DISCUSSION

5.1 SIMULATED CATHODE ENVIRONMENT

5.1.1 SEM Surface Analysis

5.1.1.1 Dry Air

An ideal cathode environment consists of dry air with no water vapor. Three model alloys, Fe-30Cr (MPS), Fe-30Cr-2Mn (MPT), and Fe-30Cr-2Mo (MPU) were exposed to dry air for 500 hours at 700°C, which is within the intermediate temperature SOFC operating range as well as the sigma formation temperature range. Additionally, the molybdenum-doped alloy was exposed at 700°C for 22 hours, 220 hours, and 362 hours. The Fe-30Cr was covered in a chromia layer on both the coarsely-polished and the finely-polished face (see Figure 13). However, the finely-polished face also had some areas which were enriched in iron. There were also some areas of localized attack on the fine face, which contained a slightly higher chromium content.

Figure 13. SEM BSE images of the MPS coarse face (A) and the MPS fine face (B) after 500 hour exposure in air at 700°C

The alloy doped with manganese showed sites of manganese enrichment on the coarsely-polished face (see Figure 14). The majority of the face was covered by chromium and iron oxides with very little manganese, but at certain areas, the iron content dropped and the manganese content significantly increased, while the oxygen and chromium levels remained relatively constant over the surface. In contrast, the finely-polished face was covered by a uniform scale consisting of oxygen with mostly manganese and chromium, and very little iron. Some precipitation of impurities, rich in carbon, magnesium, silicon, sodium, sulfur, potassium, chlorine, and calcium were seen. The origin of these species are unknown.

Figure 14. SEM BSE images of the MPT coarse face (A) and MPT fine face (B) after 500 hour exposure in air

When exposed for 22 hours, the molybdenum-doped alloy was covered in a mostly uniform iron oxide on both the coarsely-polished face and the finely-polished face (see Figure 15). The molybdenum and chromium concentrations were similar in value to the base alloy for the oxide of both the faces and did not vary significantly. On both faces there were instances of localized attack, which were generally higher in oxygen concentration and lower in iron concentration, with the chromium concentration staying roughly constant. However, in the areas of localized attack there was no molybdenum present. There were also some impurities in the areas of localized attack, mostly trace values of sodium, aluminum, silicon, and calcium.

Figure 15. SEM BSE images of the MPU coarse face (A) and MPU fine face (B) after 22 hour exposure in air

After 220 hours of exposure, the finely-polished face of the molybdenum-doped alloy specimen had more locations of localized attack (see Figure 16). The underlying oxide covering the face seemed to be a mixture of iron and chromium oxide with no molybdenum seen. The localized attack areas were very high in chromium oxides and very low in iron. It appeared as if small nodules, of more localized oxides perhaps, were growing all over the face. On the coarsely-polished side, there were some areas of localized attack, but also areas of concentrated nodule growth. The face was mostly covered by a high concentration of iron oxides with some chromium oxide as well. Just as with the finely-polished face, no molybdenum was seen on this face. The localized attack, just as with the finely-polished face, was mostly chromium oxides with a lower amount of iron compared to the rest of the face. There were a few impurities seen on this face, mostly trace amounts of sodium, sulfur, chlorine, potassium, and calcium.

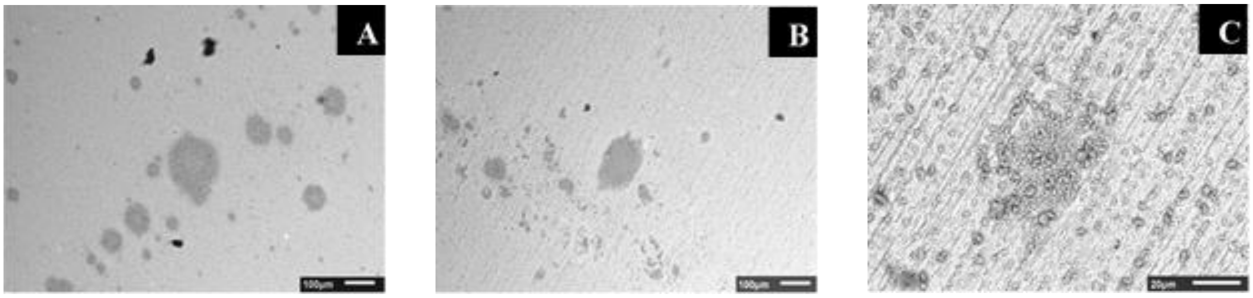

Figure 16. SEM BSE images of the MPU fine face (A) and MPU course face (B) after 220 hour exposure in air with emphasis on the nodule growth on the coarse face (C)

After 362 hours of exposure, the finely-polished face of the molybdenum-doped alloy was covered by small nodules of growth with a few areas of localized attack (see Figure 17). Most of the finely-polished face was covered with a mix of iron and chromium oxides. The areas of localized attack were heavy with chromium oxides and very little iron was observed, just as with the 220 hour specimen. There were a few brighter areas observed which were determined to be oxides slightly richer in iron than chromium. A few impurities were observed, although there were some cases of heavy carbon impurities, possibly from the SEM observation procedure. On the coarsely-polished face, there was uniform nodule precipitation and no obvious areas of localized attack. In areas not covered by a nodule, the surface was covered by a mixture of iron and chromium oxides. No molybdenum was observed on either face and the nodules which formed were chromium-rich.

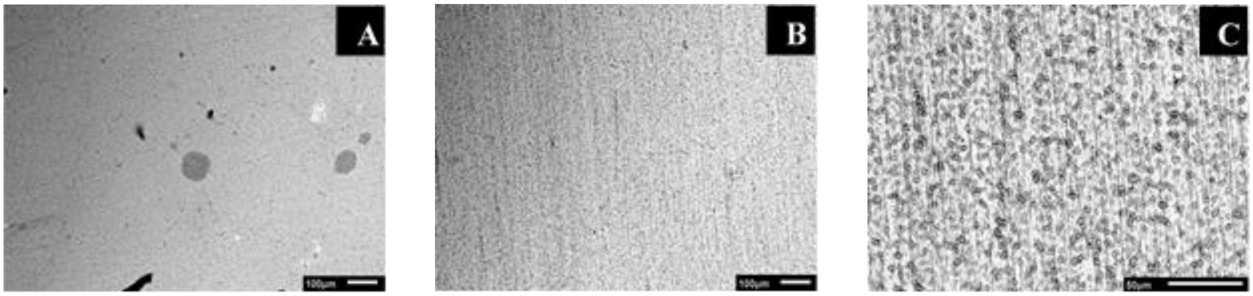

Figure 17. SEM BSE images of the MPU fine face (A) and MPU coarse face (B) after 362 hour exposure in air with emphasis on the nodule formation on the coarse face (C)

When exposed for 500 hours, the molybdenum-doped alloy had a similar coarsely-polished face phenomena as the alloy doped with manganese. The majority of the face was covered by iron and chromium oxides but there was preferential oxidation which was rich in chromium with very little iron (see Figure 18). It is interesting to note that there was no evidence of molybdenum present on the surface of the coarsely-polished face. Alternatively, on the finely-polished face, trace amounts of molybdenum were detected, although the majority of the face was covered by a mostly chromium-rich oxide.

Figure 18. SEM BSE images of the MPU coarse face (A) and MPU fine face (B) after 500 hour exposure in air

5.1.1.2 Wet Air

Certain cathode environments deviate from dry air and begin to contain water vapor, such as when a seal is leaking. Three model alloys, Fe-30Cr (MPS), Fe-30Cr-2Mn (MPT), and Fe-

30Cr-2Mo (MPU) were exposed to a wet air (10% water vapor) environment for 500 hours at 700°C. The Fe-30Cr binary alloy had surface oxidation of both chromia as well as iron oxides (see Figure 19). The darker areas corresponded to a higher chromium and oxygen content, indicative of chromia formation, whereas the lighter areas corresponded to a higher iron content as well as presence of chromium and oxygen. There were also multiple locations of impurities containing carbon, magnesium, silicon, sodium, aluminum, sulfur, potassium, and calcium. There was some presence of tin (white areas) due to the specimens being places in a tin container post-exposure. Although this specimen was finished to two different grit finishes (600 SiC and 1200 SiC) there was no difference in the oxidation behavior of either face of the specimen.

Figure 19. SEM BSE images of the MPS coarse face (A) and the MPS fine face (B) after 500 hour exposure in wet air

The alloy doped with manganese showed similar surface oxidation behavior, although there was a distinction between the coarsely-polished face and the finely-polished face (see Figure 20). Most of the coarsely-polished face was covered by an oxide layer rich in chromium and iron, with some manganese present. Along scratch marks, precipitates rich in manganese could be seen. On the finely-polished face, two oxide areas could be seen. The dark area was an oxide layer extremely rich in manganese with little iron whereas the lighter area was enriched in chromium and iron with a smaller amount of manganese.

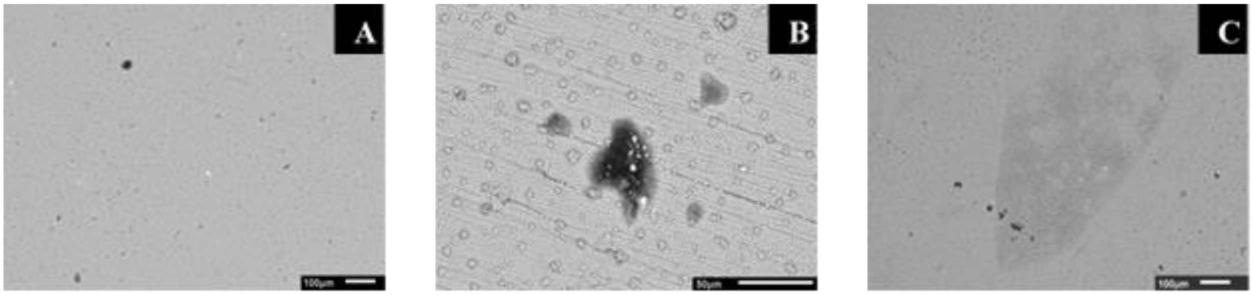

Figure 20. SEM BSE images of MPT coarse face (A), with higher magnification emphasis on the magnesium precipitates (B), and MPT fine face (C) after 500 hour exposure in wet air

The alloy doped with molybdenum did not show any presence of molybdenum on the coarsely-polished face (see Figure 21). A majority of the surface was covered by a uniform layer of chromium and iron oxide. There were also some areas which were concentrated in chromium and oxygen with very little iron presence. Just as with the alloy doped with manganese, this specimen also had trace amounts of molybdenum on the finely-polished face. However, the molybdenum-doped alloy specimen had an interesting “two-tone” structure on the fine face, with the darker areas corresponding to slightly lower chromium and iron contents compared to the lighter areas. There were a few areas of localized attack which were rich in chromium with very little iron.

Figure 21. SEM BSE images of the MPU coarse face (A) and the MPU fine face (B) after 500 hour exposure in wet air

5.1.2 XRD Analysis

Sample surfaces were analyzed by X-ray diffraction in order to determine the presence of sigma phase. Two scans were used for each sample. First, a fast scan that traveled the full 20° – 90° 2θ distance was performed to quickly determine if there was sigma presence. If sigma was present, various peaks between 35° – 50° should be detected [14]. To ensure that sigma presence was properly determined, a slower scan was performed to highlight this range and determine if such peaks were present.

5.1.2.1 Dry Air

The Fe-30Cr fast scan was fairly noisy, although major peaks only appeared around 25°, 33°, and 45° 2θ which was indicative of only alpha presence (see Figure 22). To ensure lack of sigma presence, a slow "sigma" scan was performed for 2θ values ranging from 23° to 65° (see Figure 23). This slower scan was much cleaner, but again only showed a few major peaks which correspond to only alpha presence in the alloy.

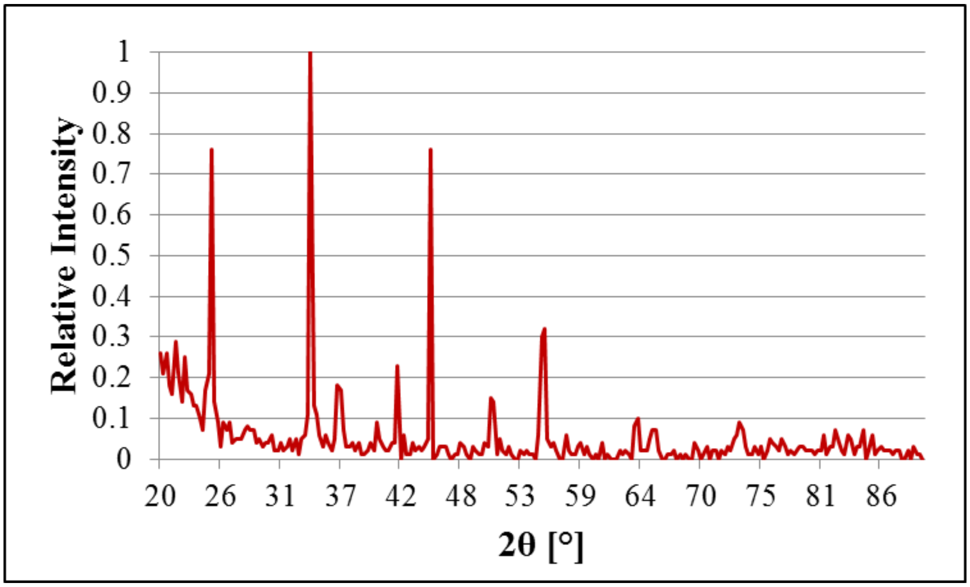

Figure 22. XRD Fast Scan of MPS alloy after 500 hour exposure at 700°C in dry air

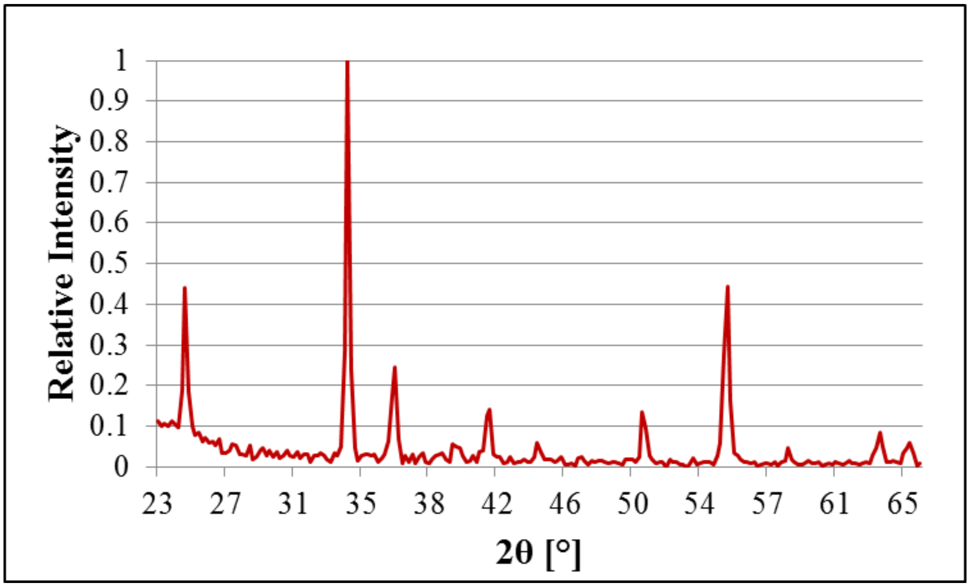

Figure 23. XRD Sigma Scan of MPS alloy after 500 hour exposure at 700°C in dry air

The fast scan for the manganese-doped alloy showed a large peak only around a 2θ value of 35° (see Figure 24). It was interesting to note that the alpha peak that should be prominent at about 45° was not seen in the fast scan, but when the sigma scan was taken, the main peaks at 35° and 45° were both seen (see Figure 25). There was no evidence of sigma formation based on these XRD plots.

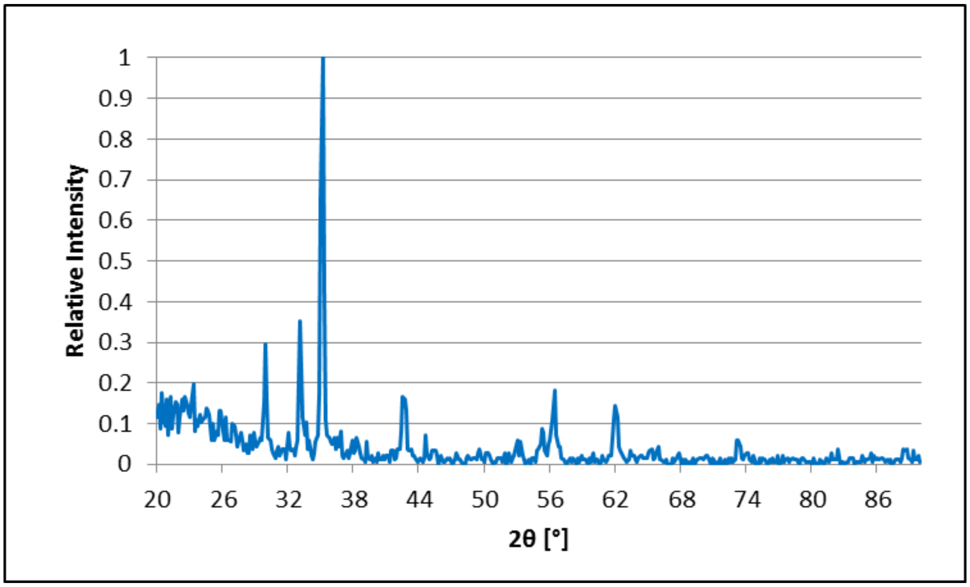

Figure 24. XRD Fast Scan of MPT alloy after 500 hour exposure at 700°C in dry air

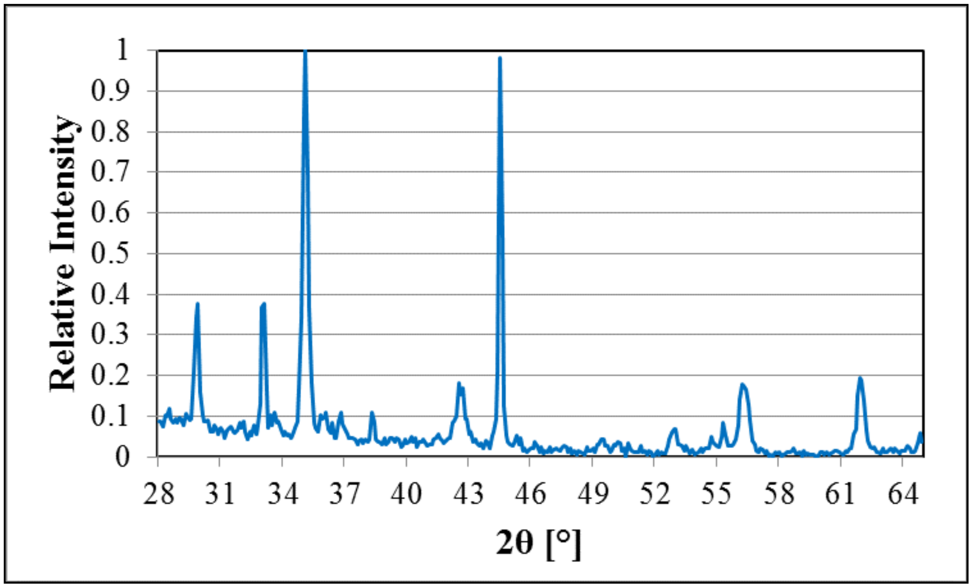

Figure 25. XRD Sigma Scan of MPT alloy after 500 hour exposure at 700°C in dry air

After a short 22 hour exposure, the only peak that was visible for the molybdenum-doped alloy with a fast scan was the 45° alpha peak (see Figure 26). A slow sigma scan of the area confirmed that this was the only peak visible, suggesting that there is no sigma presence after 22 hours of exposure (see Figure 27). After 220 hours of exposure in dry air, the fast scan for the molybdenum-doped alloy was much messier (see Figure 28). When a slower sigma scan was used, the only major peaks appeared around 33° and 37° (see Figure 29). Similar to the manganese-doped alloy, it was interesting to note that the large 45° peak was not present in this alloy. After 362 hours of exposure, the molybdenum-doped alloy fast scan was still very messy (see Figure 30). A slower sigma scan showed peaks at 33° and 36°, similar to the 220 hour exposure alloy (see Figure 31). However, at 500 hours, the fast XRD scan suggests sigma formation from the presence of a variety of peaks between 38° and 51° (see Figure 32). A slower sigma scan of this region confirms the presence of many low intensity peaks surrounding the high intensity alpha peak at about 45° (see Figure 33). The presence of these peaks suggests sigma formation in the molybdenum-doped alloy after 500 hours of exposure.

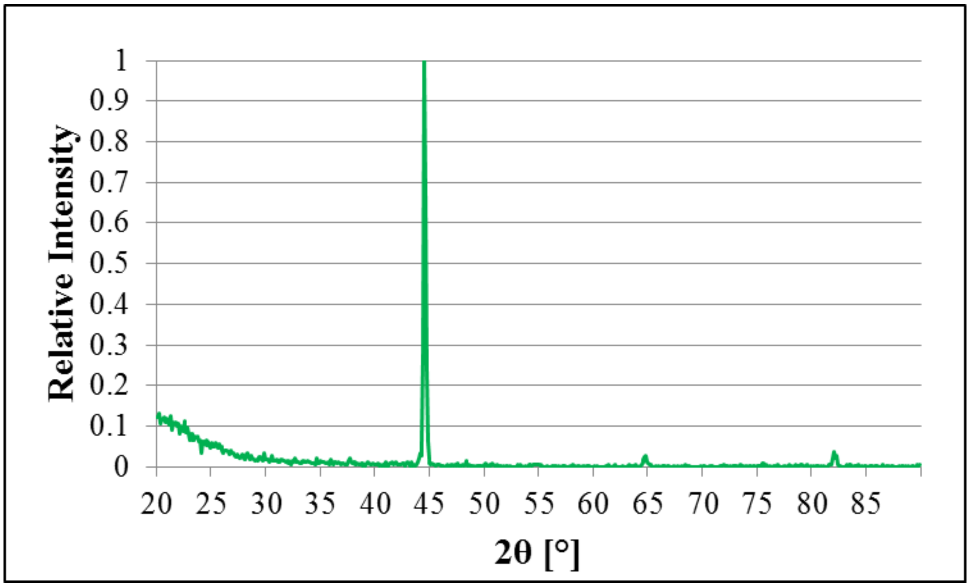

Figure 26. XRD Fast Scan of MPU alloy after 22 hour exposure at 700°C in dry air

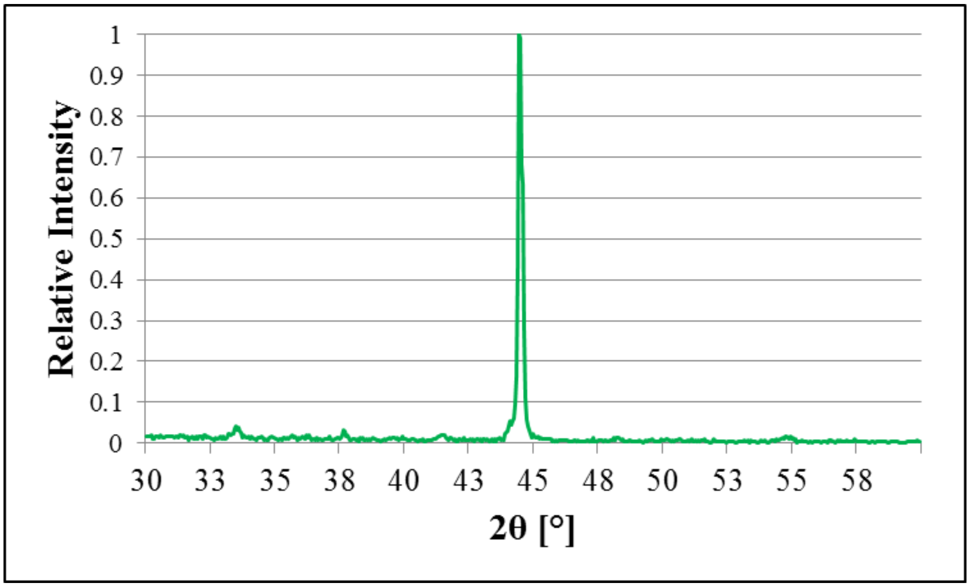

Figure 27. XRD Sigma Scan of MPU alloy after 22 hour exposure at 700°C in dry air

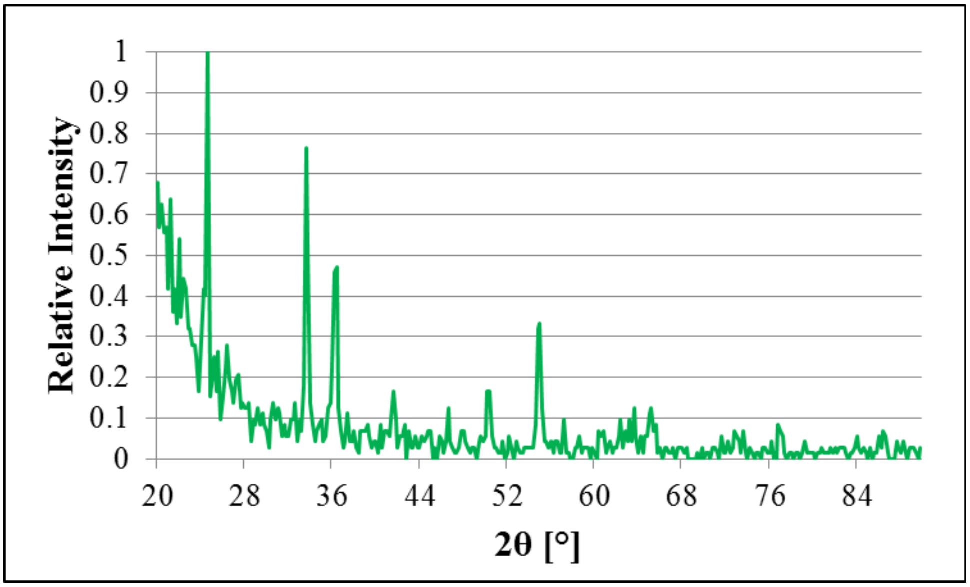

Figure 28. XRD Fast Scan of MPU alloy after 220 hour exposure at 700°C in dry air

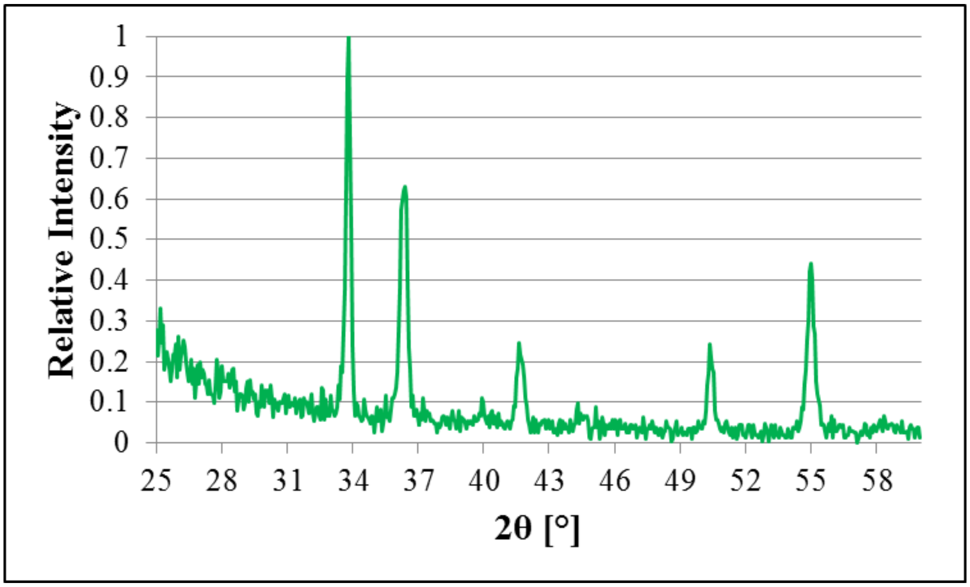

Figure 29. XRD Sigma Scan of MPU alloy after 220 hour exposure at 700°C in dry air

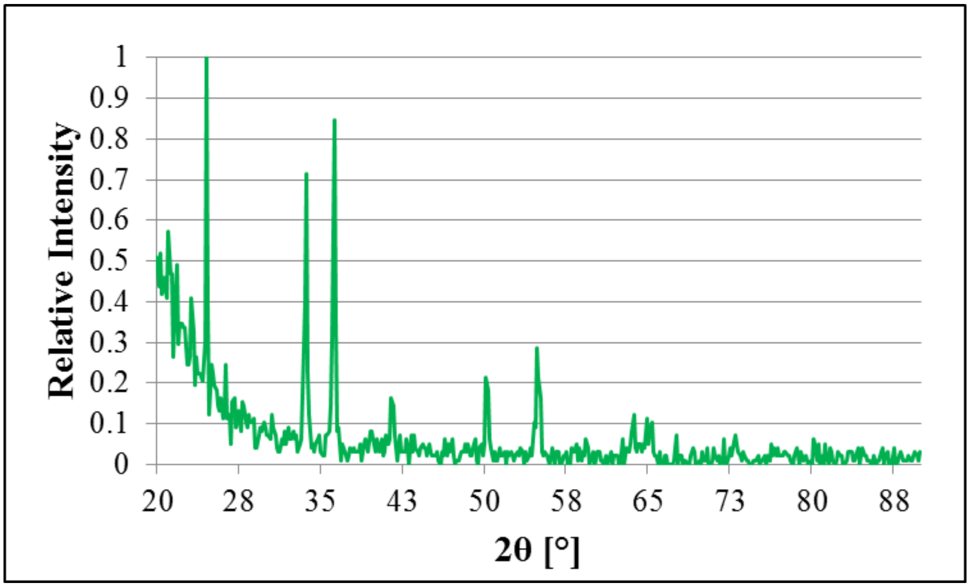

Figure 30. XRD Fast Scan of MPU alloy after 362 hour exposure at 700°C in dry air

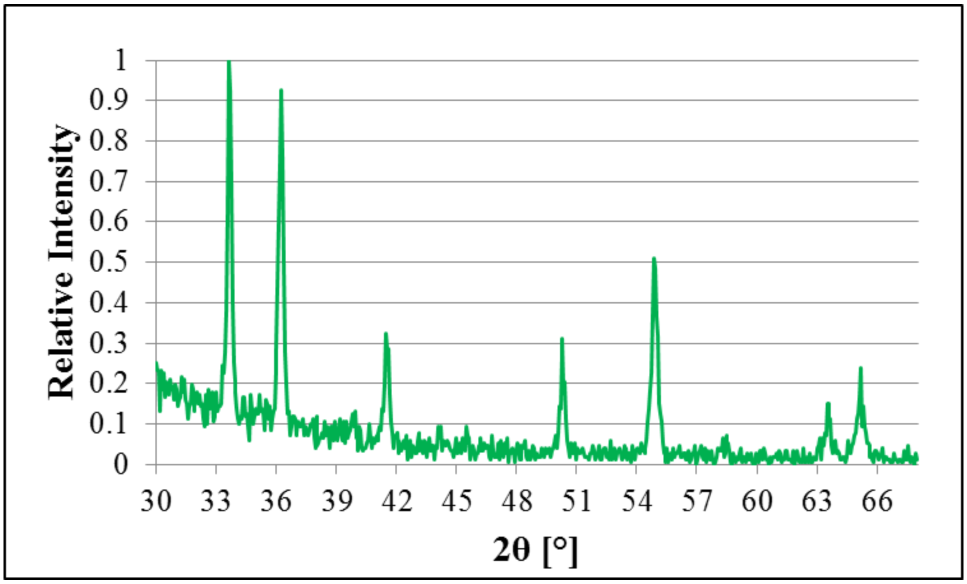

Figure 31. XRD Sigma Scan of MPU alloy after 362 hour exposure at 700°C in dry air

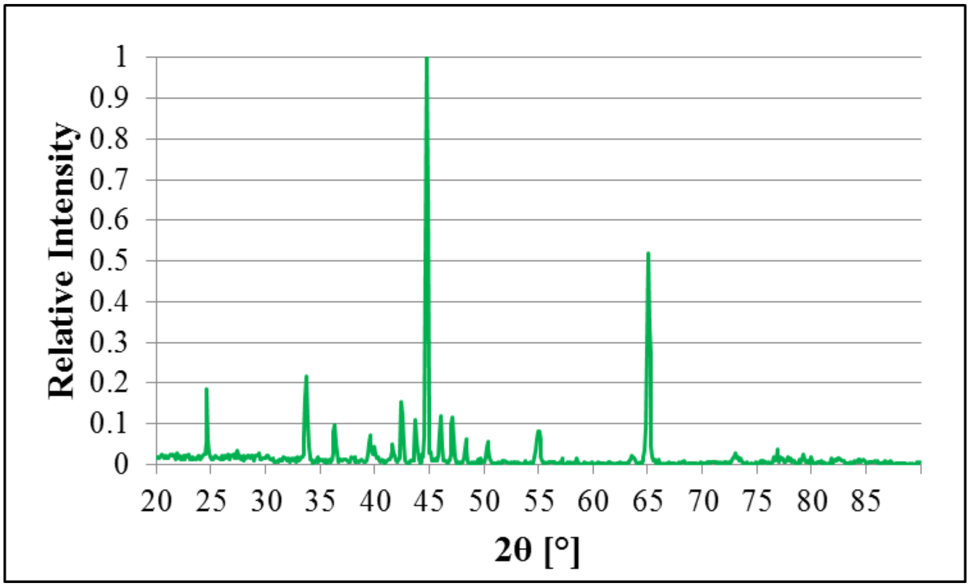

Figure 32. XRD Fast Scan of MPU alloy after 500 hour exposure at 700°C in dry air

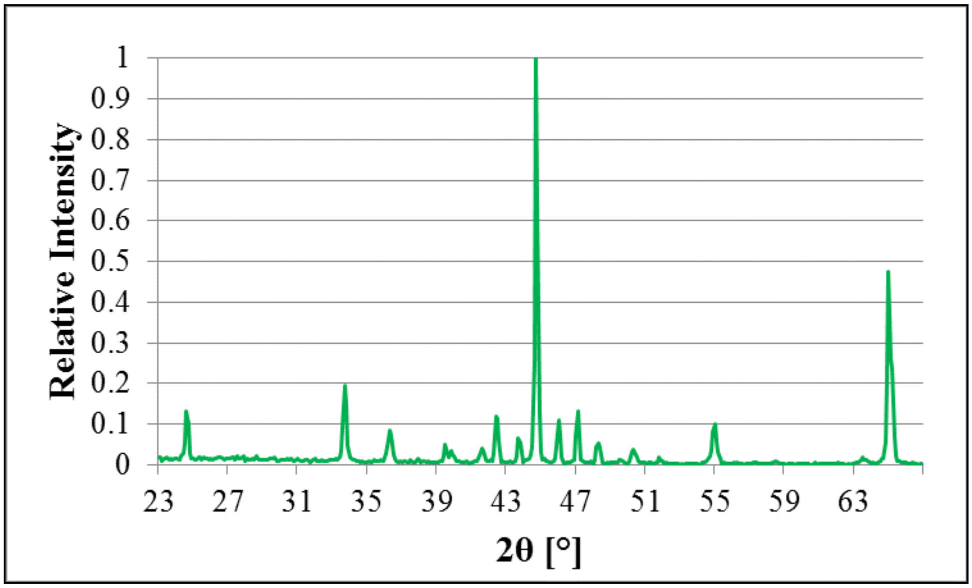

Figure 33. XRD Sigma Scan of MPU Alloy after 500 hour exposure at 700°C in dry air

5.1.2.2 Wet Air

The Fe-30Cr fast XRD scan in the air and water vapor environment looks almost identical to the fast scan in air only. There are noticeable peaks at about 24°, 33°, 37°, and a few smaller peaks between 40° and 55° (see Figure 34). Again it is interesting to note that the large alpha peak that should appear around 45° is not seen. When the sigma scan was performed, the graph looked much cleaner, but the same peaks were prominent as in the fast scan (see Figure 35). These suggest that there is no sigma formation in either environment, but also that something may be happening to the fraction of ferrite phase in the material under the wet air environment which is causing the prominent 45° peak to disappear. This seems highly unlikely, however, and a more reasonable explanation is that there may be some texturing of some of the specimens analyzed which is causing a diminishing or disappearing of the 45° peak.

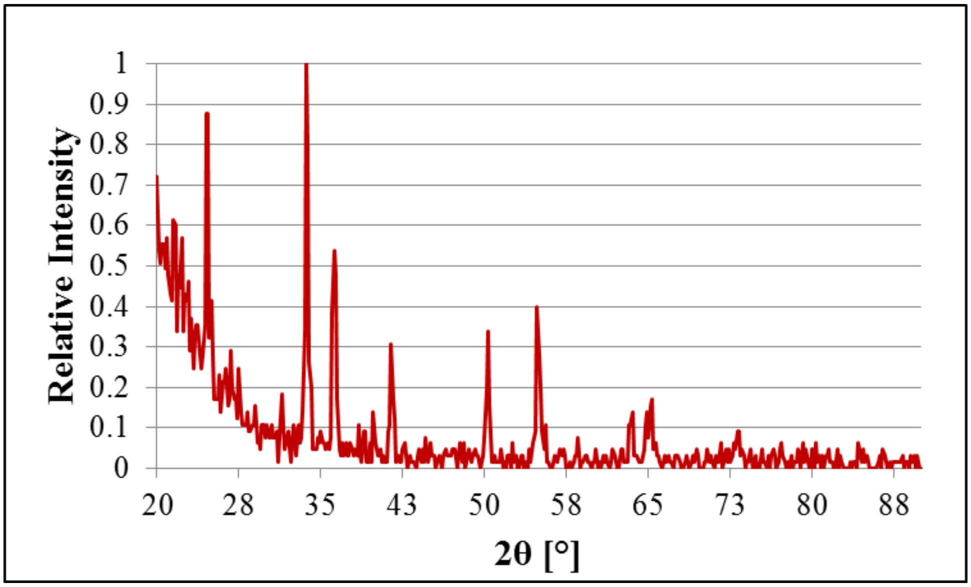

Figure 34. XRD Fast Scan of MPS Alloy after 500 hour exposure at 700°C in wet air

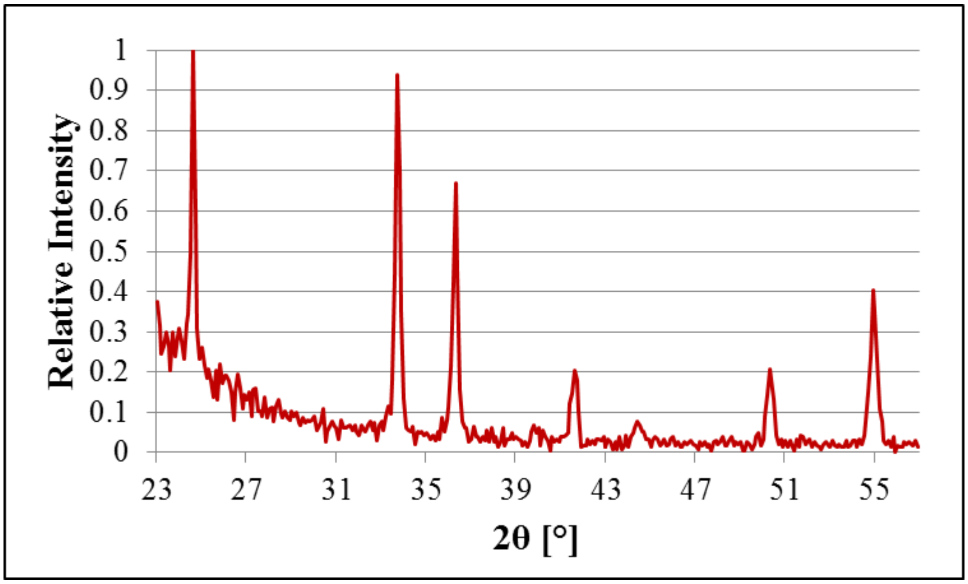

Figure 35. XRD Sigma Scan of MPS Alloy after 500 hour exposure at 700°C in wet air

Just as with the Fe-30Cr alloy, the alloy doped with manganese fast scan in the wet air environment looked similar to the fast scan in the air only environment. There is one large prominent peak at 35° and a few smaller ones around it (Figure 36). Just as with the Fe-30Cr scan, the 45° ferrite peak is not seen, but this was the case for both dry air and wet air with the manganese-doped alloy specimen. A slower sigma scan showed only one prominent peak at about 35° and suggests that the wet air environment also does not promote sigma formation (see Figure 37).

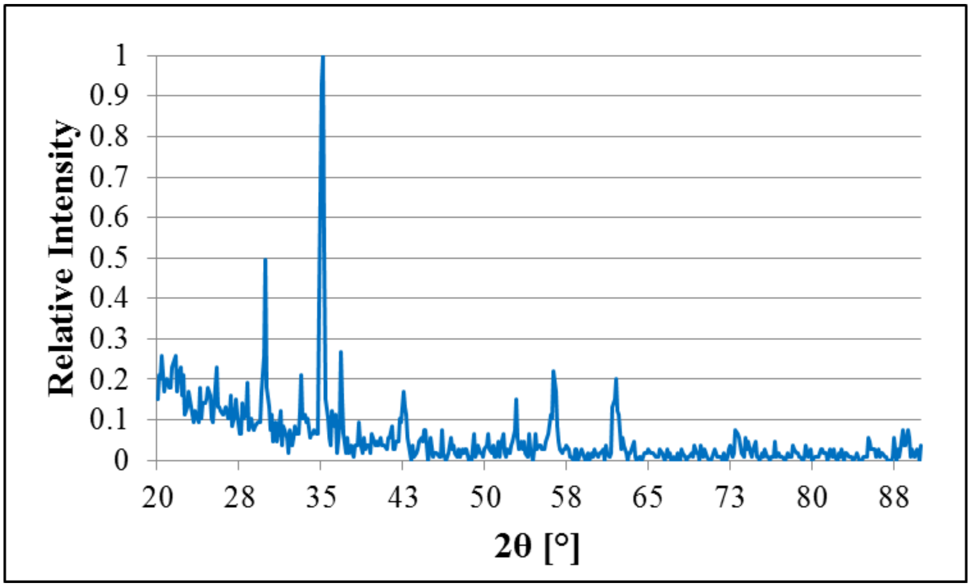

Figure 36. XRD Fast Scan of MPT Alloy after 500 hour exposure at 700°C in wet air

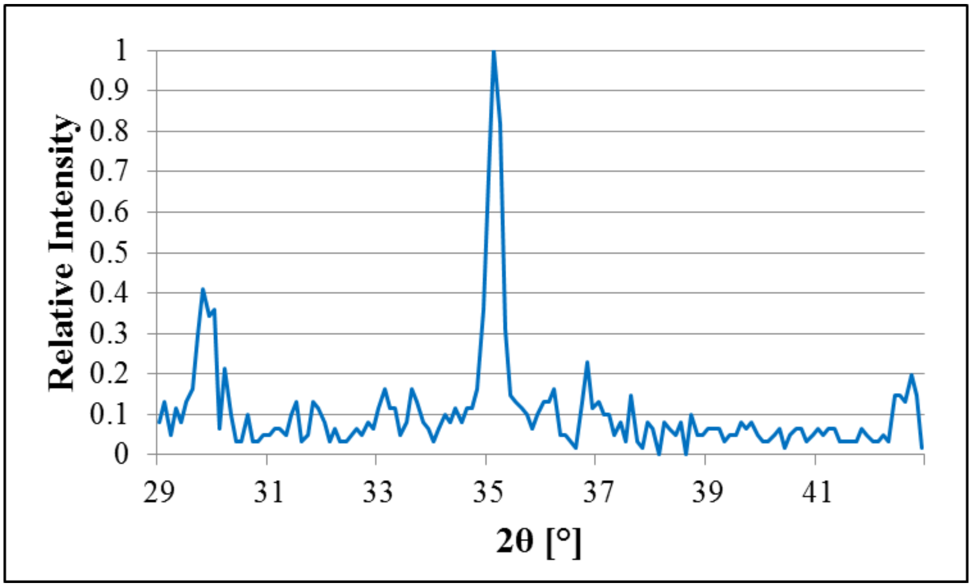

Figure 37. XRD Sigma Scan of MPT Alloy after 500 hour exposure at 700°C in wet air

The fast scan of the molybdenum-doped alloy in wet air looks similar to the dry air sample exposed for 500 hours. However, the sigma peaks that surround the alpha peak at 45° are of a higher relative intensity, about 0.25 – 0.6, compared to the dry air peaks, around 0.1 (see Figure 38). A slower sigma scan showed even higher relative intensities for the sigma peaks, reaching almost 0.85 (see Figure 39). These scans suggest that sigma formation has occurred in the manganese-doped alloy in wet air and that there may be a higher relative fraction of sigma which precipitates when the alloy is exposed to wet air as opposed to dry air.

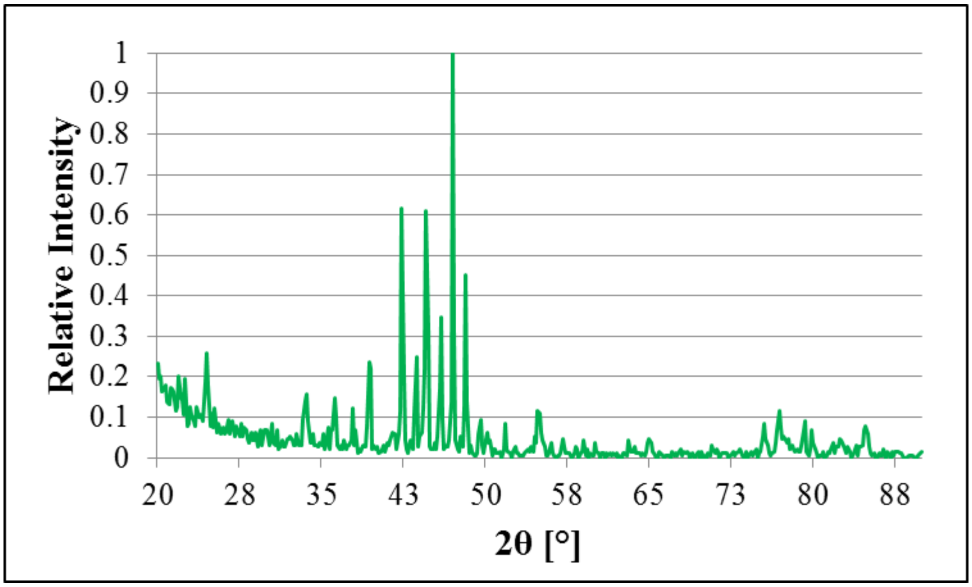

Figure 38. XRD Fast Scan of MPU Alloy after 500 hour exposure at 700°C in wet air

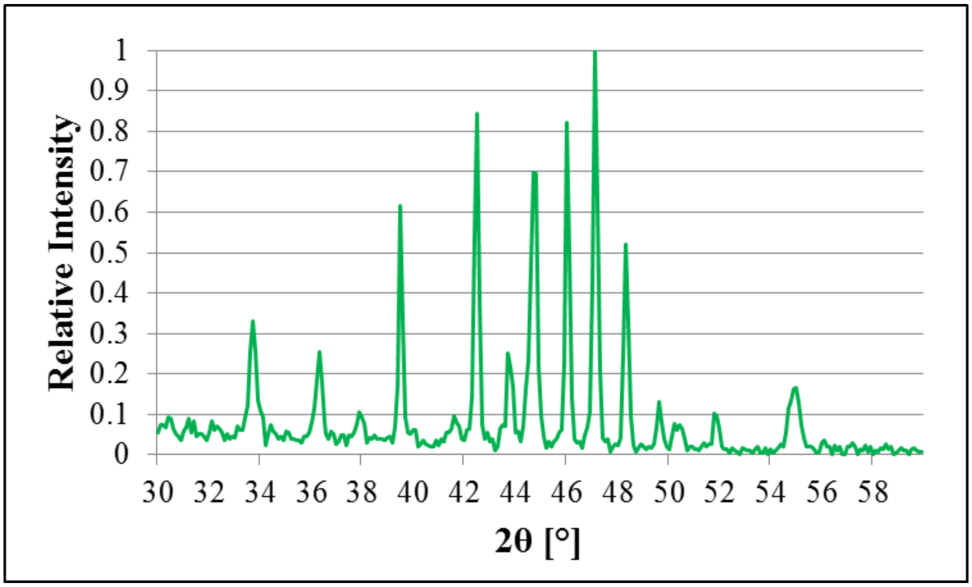

Figure 39. XRD Sigma Scan of MPU Alloy after 500 hour exposure at 700°C in wet air

5.1.3 Electrolytic Etching

5.1.3.1 Dry Air

The electrolytic etch applied to these alloys was a 10% aqueous KOH solution. The etch turns the sigma phase a bright orange/yellow color while the rest of the material should remain its natural color. When the etch was applied to both the F3-30Cr and Fe-30Cr-2Mn alloys, no effect was seen. There was some residue left from the solution, but no obvious formation of sigma phase due to a lack of any colored phases when observed with an optical microscope (see Figure 40).

Figure 40. Micrographs of electrolytic etching of MPS (A) and MPT (B) alloys after 500 hour exposure at 700°C in dry air

When the electrolytic etch was applied to the molybdenum-doped alloy, the specimens exposed for 22, 220, and 362 hours had similar results compared to the Fe-30Cr and manganese-doped alloys (see Figure 41). However, the molybdenum-doped alloy specimen exposed for 500 hours clearly had sigma formation (see Figure 42). There was sigma formation all along the edge of the sample, and sigma could be seen growing inward from the edge along what seemed to be the grain boundaries. The sigma is distinguishable as a dark orange color and the brittleness of the phase can be seen in the various cracks within the phase.

Figure 41. Micrographs of electrolytic etching of MPU alloy exposed for 22 hours (A), 220 hours (B), and 362 hours (C) at 700°C in dry air

Figure 42. Micrographs of electrolytic etching of MPU alloy exposed for 500 hours at 700°C in dry air showing edge formation of sigma (A) and grain boundary formation of sigma (B)

5.1.3.2 Wet Air

The Fe-30Cr and manganese-doped alloys had similar results in wet air compared to dry air when the electrolytic etch was applied (see Figure 43). There was no evidence of sigma formation in either alloy. However, the molybdenum-doped alloy had extensive sigma growth, similar in nature to the dry air exposure (see Figure 44). The growth was seen in small sigma grains forming around the edge of the sample with larger grains growing inwards along grain boundaries. When exposed in wet air, it was seen that sigma would nucleate at what appears to be grain boundaries in the center of the sample without needing to grow inward from the sample edge. Just as with the dry air sample, the sigma formation in the wet air sample is a bright yellow color and can easily be distinguished by the cracking evident in the grains. It does appear as if there is more sigma nucleation and growth at the internal grain boundaries of the wet air specimen compared to the dry air specimen. This was also theorized based on the XRD peaks intensities seen in the wet air specimen compared to the dry air specimen.

Figure 43. Micrographs of electrolytic etching of MPS (A) and MPT (B) alloys after 500 hour exposure at 700°C in wet air

Figure 44. Micrographs of electrolytic etching of MPU alloy exposed for 500 hours at 700°C in wet air showing edge formation of sigma (A) and grain boundary formation of sigma (B)

5.1.4 SEM Cross-Sectional Analysis

SEM was performed on the sample cross-sections to confirm existence or non-existence of sigma phase. If sigma phase was seen, as with the molybdenum-doped alloy specimens, compositional analysis was also performed to determine the chemical composition of the sigma phase.

5.1.4.1 Dry Air

Neither the Fe-30Cr nor the manganese-doped alloys showed signs of sigma formation. When observed in backscatter compositional mode on the SEM, no instances of formation could be found (see Figure 45).

Figure 45. SEM BSE micrographs of MPS (A) and MPT (B) alloys after 500 hour exposure at 700°C in dry air

The molybdenum-doped alloy, when exposed for 22, 220, and 362 hours, also did not show any sigma formation (see Figure 46). However, after 500 hours of exposure, sigma formation was observed both at the surface (edge) of the sample as well as along some internal grain boundaries (see Figure 47). When the sigma grains were analyzed with EDX on the SEM, the composition was determined to be Fe-35Cr-6Mo wt.%. This composition was roughly constant (within 1 wt.%) for all sigma formation throughout the sample, whether it was from the surface or an internal grain boundary. Analysis of the surrounding matrix did not show a large diffusion zone, as compositional analysis of roughly Fe-30Cr-2Mo was seen at a distance of about 30 microns from a sigma grain.

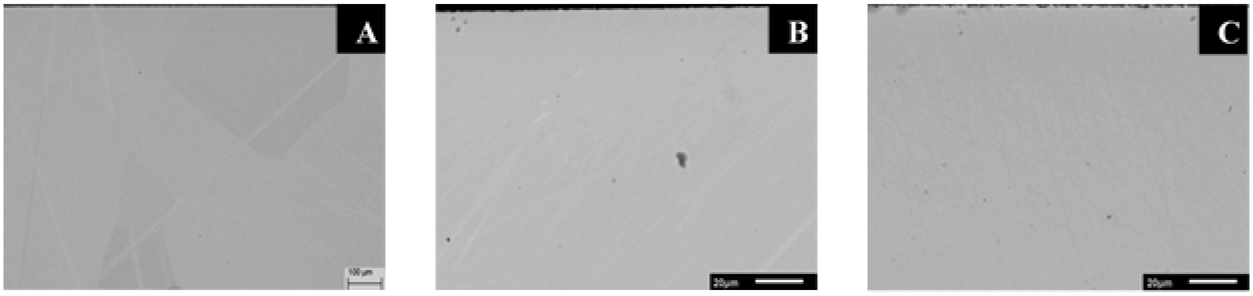

Figure 46. SEM BSE micrographs of MPU after 22 hour (A), 220 hour (B), and 362 hour (C) exposure at 700°C in dry air

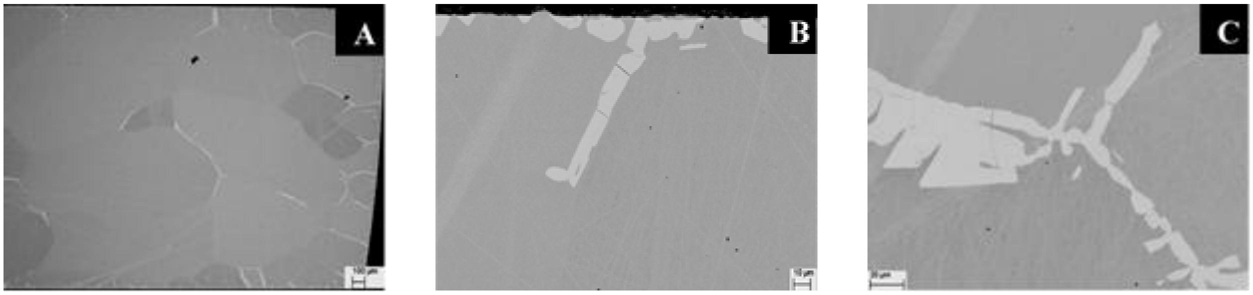

Figure 47. SEM BSE micrographs of MPU after 500 hour exposure at 700°C in dry air showing sigma phase formation through the thickness of the sample (A) with focus on the edge formation (B) and inner grain boundary formation (C)

5.1.4.2 Wet Air

Just as with the dry air sample, the wet air specimen of the Fe-30Cr alloy did not show any sign of sigma formation (see Figure 48). Although the manganese-doped alloy specimen did not show signs of sigma precipitation in earlier analysis, SEM observation revealed two small precipitates of sigma grains near the surface of the sample (se Figure 49). When analyzed with EDX, the composition of the sigma was determined to be roughly Fe-41.5Cr-0.5Mn. However, no other instances of sigma formation could be found in the sample, and so a vast majority of the sample could be considered “sigma-free”.

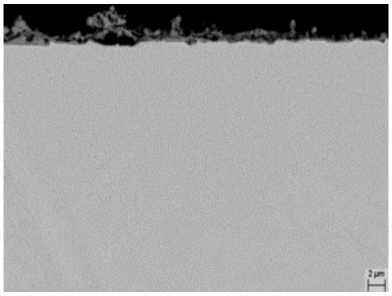

Figure 48. SEM BSE micrograph of MPS after 500 hour exposure at 700°C in wet air

Figure 49. SEM BSE micrographs of MPT after 500 hour exposure at 700°C in wet air of a typical cross-sectional view (A) with a focus on one of the sigma grain formations (B)

The molybdenum-doped alloy after 500 hour exposure in wet air had similar results to the alloy exposed for 500 hours in dry air (see Figure 50). There was sigma formation seen all around the edge of the sample growing inward. There was also precipitation at some internal grain boundaries with no connections to the grains growing from the edge of the sample. When analyzed with EDX, the sigma phase composition was roughly Fe-38Cr-3Mo. This composition was relatively constant, within 1 wt.% among all sigma phase formation in the sample, both surface grains and internal grains. There did not seem to be a large diffusion zone from the surface; at a distance of 12 microns away from the surface sigma grain, the matrix had a composition of Fe-31Cr-2Mo which is roughly the same as the composition of the manganese-doped alloy.

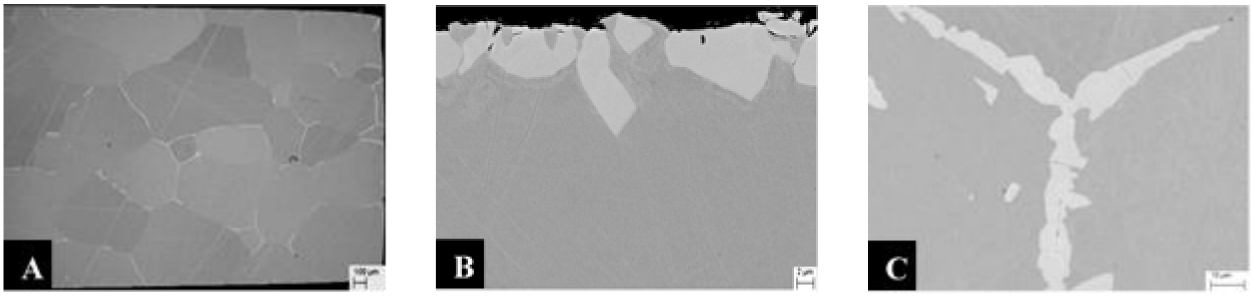

Figure 50. SEM BSE micrographs of MPU after 500 hour exposure at 700°C in wet air showing sigma phase formation through the thickness of the sample (A) with focus on the edge formation (B) and inner grain boundary formation (C)

5.1.5 The Effect of Surface Roughness and Exposure Environment on Surface Oxidation and Sigma Formation

When observing the effect of surface roughness on surface oxidation, there was a clear distinction between the coarsely-polished surface and finely-polished surface for all alloys. In all cases, the finely-polished surface tended to have more locations of localized attack, all of which was chromium-rich. For the Fe-30Cr alloy, the effect of surface roughness was the same regardless of environment. In the case of the manganese-doped alloy, the wet environment did not cause a change in the effect of the coarsely-polished surface. However, for the finely-polished surface, the wet environment caused a change from a uniform Cr, Mn oxide scale to areas of either chromium oxide scale or manganese oxide scale. The molybdenum-doped alloy had a similar result, with the coarsely-polished surface having no change of effect in the wet environment. Just as with the manganese-doped alloy however, the wet air environment did cause a separation of oxides for the finely-polished surface from a uniform Cr, Fe oxide to areas of either chromium oxide or iron oxide.

This effect is similar to results by Hammer et. al. where it was seen that water vapor in the cathode atmosphere caused volatilization of the chromia layer with as little as 0.1% water vapor . The water vapor was also seen to cause discontinuous particles of manganese on the surface, which only provides partial protection to volatilization [11]. This is directly seen in the manganese-doped alloy wet air, finely-polished surface. The surface of the specimen was originally a Cr,Mn-spinel which provides protection, but upon the introduction of water vapor, the surface split into areas of Mn-spinel and areas of chromia exposed to the atmosphere, which would be able to volatize.

Generally speaking, a coarsely-polished surface allowed for more iron oxide formation compared to the fine faces which favored chromium oxides and, in the case of the manganese-doped alloy, manganese oxides. Based on the Ellingham diagram, this could make sense for the exposure temperature of 700°C (see Figure 51). Although all oxides should easily form in atmospheric air, manganese oxide will form the easiest, followed closely by chromium oxide, and much later by iron oxide. However, this is under the assumption that the activity of the manganese in the alloy is 1. During exposure, the actual activity of manganese may be much lower than this, and could also explain why chromium-oxides tended to be the most prevalent to form. The coarsely-polished surface also allows for easier oxidation of iron, perhaps due to increased surface area which the oxides can form on.

Although the surface roughness had an effect on surface oxidation behavior of the alloys, no effect on sigma formation was noticed. Only the molybdenum-doped alloy had sigma formation after 500 hours of exposure, and in both the wet and dry air environment, the sigma formation along the edge of the specimen sample was uniform, regardless of surface roughness.

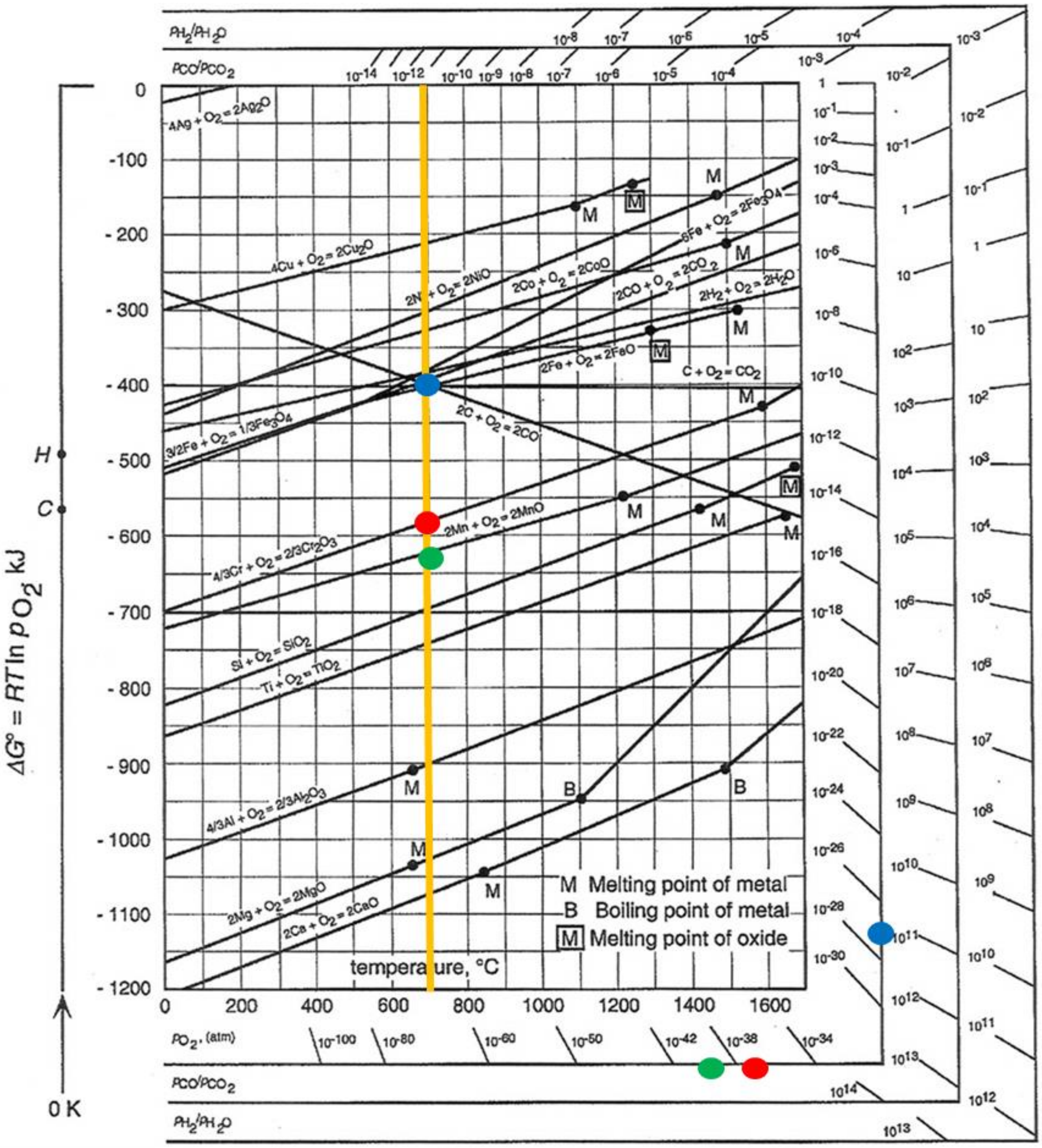

Figure 51. Ellingham Diagram of common oxides highlighting the necessary oxygen partial pressure for iron oxide (blue), chromium oxide (red), and manganese oxide (green) at 700°C [34]

5.1.6 The effect of Molybdenum and Water Vapor on Sigma Formation

The results from the cathode-simulated environment tests clearly show an effect of the addition of molybdenum on the formation of sigma phase in an iron-chromium alloy. This could be due to molybdenum atoms replacing chromium atoms in the crystal structure. Chromium has an atomic radius of about 128 pm and molybdenum has an atomic radius of about 139 pm. When molybdenum replaces chromium, there could be enough strain formed to provide energy for the nucleation of sigma phase. Conversely, manganese has an atomic radius of 127 pm, which is very close to the value for chromium. Even if manganese were to replace chromium in the crystal structure, enough strain energy may not be generated in order for easy and/or quick nucleation of sigma phase.

The formation of sigma phase in the molybdenum-doped alloy specimens confirms prior research done by Anderson and Lundberg that molybdenum is a known sigma phase promoter. In the case of their work, molybdenum replaced chromium in the sigma phase of austenitic steels [31]. Similarly, it can be theorized that molybdenum is replacing chromium for sigma phase formation in the ferritic Fe-30Cr-2Mo alloy when the composition of sigma phase is analyzed. In the dry air exposure, the sigma phase was determined to be about Fe-35Cr-6Mo (wt.%) and in the wet air exposure the sigma phase was determined to be about Fe-38Cr-3Mo (wt.%). If molybdenum is assumed to be replacing the chromium then the pseudo-composition of the sigma phase could be written in terms of just iron and chromium. In this case, both sigma phases are roughly of composition Fe-41Cr (wt.%). On the binary Fe-Cr phase diagram, at 700°C, sigma phase can begin to form in equilibrium with ferrite at a composition of about Fe-30Cr (wt.%) with pure sigma phase forming at a composition of about Fe-43 Cr (wt.%). The composition of the sigma phase seen in the samples is very close to this value. However, the effect of molybdenum on the iron-chromium system can cause many other phases and equilibria to form (see Figure 52). In the case of the lone sigma phase grain seen in the manganese-doped alloy after exposure in wet air, the composition of the phase was determined to be roughly Fe-41.5Cr-

0.5Mn (wt.%). Using the same theory as with the molybdenum-containing sigma phase, this would correlate to a binary sigma composition of about Fe-42Cr (wt.%) which is again, very close to the value in the iron-chromium binary diagram.

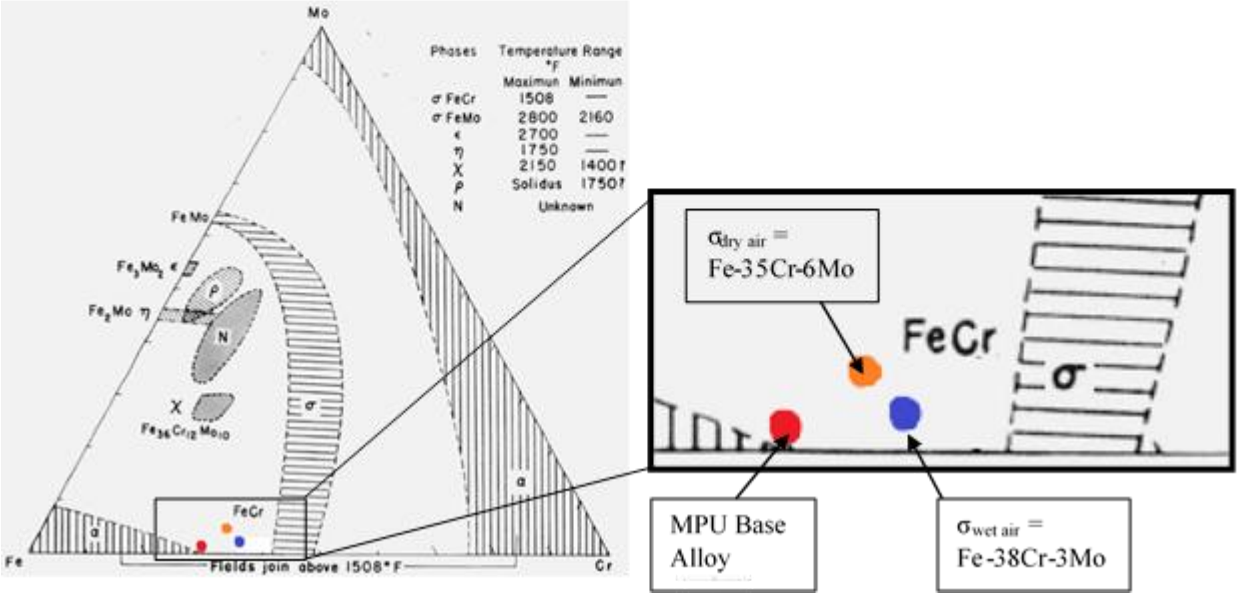

Figure 52. Fe-Cr-Mo ternary equilibrium diagram with MPU alloy and sigma phase plotted [35]

It can be seen in the ternary diagram that the molybdenum-doped alloy should already have sigma phase formation since the addition of 2 wt.% molybdenum places the material in a two-phase field of ferrite and sigma. However, the base material shows no sigma, but after exposure for 500 hours in both environments, the sigma phase can be seen on the diagram as also existing in the two phase field.

The effect of the wet air environment can be seen by the differences in the sigma phase formation of the two samples. Somehow, hydrogen presence in the atmosphere causes a "purer" sigma phase to form. That is, the sigma phase that has formed in the wet air environment relies less on the addition of molybdenum to form. Qualitatively, it could also be theorized that the presence of hydrogen in the atmosphere causes a larger amount of sigma phase to form, especially at internal grain boundaries. This is similar to results seen by Hammer et. al. where they also saw that wet air tended to cause more sigma formation [11].

When comparing Figure 47.A with Figure 50.A, it appears as if sigma has nucleated at a larger amount of grain boundaries in the wet air atmosphere after exposure compared to the dry air atmosphere. In the wet air sample, it looks as though almost every grain has some of its boundary defined by sigma phase formation. Conversely, in the dry air sample, there are large areas where individual grains are discernible, but no sigma phase formation has occurred. Previous work done by Weiss and Stickler in austentic alloys showed that sigma has a preferential order for nucleation sites. In their work, sigma nucleated first at external triple points, then grain boundaries, then twin boundaries, and finally intergranularly at precipitate sites [27]. In this case then, the addition of hydrogen in the atmosphere allows for additional nucleation at grain boundaries compared to the dry air environment. The hydrogen may be dissolving into the ferrite matrix and traveling to the grain boundaries where it lowers the energy required for nucleation and growth of sigma phase.

Another interesting note of comparison is the average grain size of the sigma phase that precipitated at the edges of the samples. After random measurements of the grains were taken, it was seen that the sigma phase grains which precipitated at the edge of the dry air sample were roughly twice as large as the sigma phase grains which precipitated at the edge of the wet air sample. However, it should also be noted that it appears as if the sigma phase which precipitated at the edge of the dry air sample was more discrete than the grains which precipitated at the edge of the wet air sample. That is, the wet air sample, at times, had an almost continuous, thin layer of sigma phase along the edge, which was rarely, if ever, seen in the dry air sample. Clearly, hydrogen is causing some sort of effect in sigma formation on the surface of the alloy. It could be that as the hydrogen dissolves into the alloy the surface is somehow affected with additional broken bonds or energy that allows for easier formation of sigma to occur. According to work done by Dubiel and Cieślak, the alpha to sigma transformation curve is s-shaped, with the incubation and growth periods being slow, but the nucleation period being fast [16]. Therefore, the hydrogen is either decreasing the incubation and/or growth period or increasing the nucleation period to allow for more nucleation and growth at the surface of the alloy.

Additionally, the fact that almost the entire surface was covered by a thin layer of sigma phase meant that external triple point nucleation sites were becoming limited. As suggested by Weiss and Stickler, the next location for nucleation and growth is at grain boundaries [27]. This would explain why the wet air specimen had additional sigma phase nucleated at internal grain boundaries compared to the dry air specimen. Because the surface was almost entirely covered in sigma phase, and nucleation was still occurring, more grain boundaries were used as nucleation and growth sites internally.

Although a few individual grains of sigma phase formation were seen in the manganese sample after wet air exposure, it is possible that there was insufficient time for additional sigma phase to precipitate and grow. Longer times may be needed in order for sufficient nucleation and growth of sigma phase to occur in order for the Fe-30Cr alloy to be comparable to the molybdenum-doped alloy. The addition of 2 wt.% molybdenum must somehow decrease the incubation or equilibrium time of sigma phase to be significantly shorter than the times required for either the alloy with 2 wt. % manganese or the binary Fe-30Cr alloy. It has been determined that the incubation time for sigma phase nucleation is a time between 362 hours and 500 hours for a 700°C isothermal dry air environment in a Fe-30Cr-2Mo alloy. Based on the increased amount of sigma formation in the wet air environment specimen, the incubation time for the same alloy in a wet air environment may be less than 362 hours. It may also be that the incubation time does not change, but rather than the wet air environment causes a shorter nucleation time or a faster growth after nucleation.

5.1.7 Summary of Simulated Cathode Environment Results

There was an effect of surface roughness on the surface oxidation of all the alloys tested. In all cases, having a coarser-polished surface allowed for more iron oxide to form during exposure. This may be due to an increased surface area available for oxidation which allows the less stable iron oxide to form along with the more stable chromium oxide and manganese oxide. In contrast, the finely-polished surfaces had more areas of localized attack. When water vapor was introduced to the exposure environment, the finely-polished surfaces of the manganese-doped and molybdenum-doped alloys changed from a uniform oxide scale to a mixed oxide scale. In the case of the manganese-doped alloy, it changed from uniform Cr,Mn-spinel coverage to areas of either chromia or manganese oxide. In the case of the molybdenum-doped alloy, it changed from a uniform chromia scale to areas of chromia or iron oxide. This splitting of the oxides on the surface may be due to the water vapor causing volatilization of the chromia scale.

After 500 hours of exposure in both dry air and wet air at 700°C, the binary Fe-30Cr alloy did not contain any sigma formation. When 2 wt.% manganese was added to the alloy, a few grains of sigma had formed after 500 hour exposure in wet air, with dry air exposure showing no signs of sigma formation. It may be that 500 hours is the minimum incubation time for sigma formation in the manganese-doped alloy when exposed in wet air, and that the incubation time for dry air exposure is a longer period of time.

The alloy doped with 2 wt. % molybdenum showed significant sigma formation after 500 hour exposure in both dry air and wet air. While the exact composition of the sigma phase was slightly different for each exposure, the pseudo-binary composition for both alloys was determined to be Fe-41Cr (wt.%) which is very close to the composition of pure sigma phase based on the phase diagram for iron-chromium at 700°C. Although the dry air sample had larger sigma grains which had grown at the surface edge of the sample, the wet air sample had more sigma phase growth at internal grain boundaries throughout the thickness of the sample. Additionally, the wet air specimen had areas of a continuous, thin layer of sigma phase at the surface edge of the sample, whereas the dry air specimen only had discrete grains. Based on additional exposure times which were tested for the dry air environment, the propagation time for sigma nucleation in the manganese-doped alloy was determined to be a time between 362 hours and 500 hours. Due to the increased amount of sigma phase which had grown at internal grain boundaries in the wet air sample and along the entire specimen edge, it could be concluded that the presence of water vapor aided in lowering the incubation time for sigma nucleation in the manganese-doped alloy and allowed for more growth of the phase after 500 hours of exposure, forcing additional precipitation and growth of sigma phase internally.

5.2 SIMULATED ANODE ENVIRONMENT

An environment of Ar-4%H_2-10%H_2O was used for all simulated anode environment tests. The water vapor was introduced into an Ar-4%H_2 gas mix by the same method as for the wet air simulated cathode environment. The main point of the environment is to simulate the use of hydrogen or hydrocarbons as fuel, along with their combustion products, while keeping the partial pressure of oxygen low.

Most specimens which were exposed to the simulated anode environment were pre-coated with a thin layer of nickel. These specimens were the focus of a majority of this section, but non-coated specimens of a few alloys were also investigated briefly.

5.2.1 SEM Surface Analysis

Five alloys, a low Cr-content ferritic alloy (LKC), Crofer® 22APU (KMT), Crofer® 22APU with additional niobium and silicon (KST), Crofer® 22APU with additional tungsten (KDN), and Crofer® 22H (MEC), were exposed in the simulated anode environment for 220 hours at 700°C without a pre-coated layer of nickel. Post-exposure, the surfaces of these specimens were examined using SEM to determine surface conditions and the composition of any oxides that may have formed.

All the specimens formed an external chromia layer with manganese spinel above it (see Figure 53). The spinel was formed either as whiskers or platelets. All of the alloys, except for the one with niobium and silicon additions, formed relatively uniform layers of Mn-spinel above the base layer of chromia. Crofer® 22APU with tungsten and Crofer® 22H formed the largest platelets, while the low-Cr alloy and Crofer® 22APU formed smaller platelets with more whiskering around them. Where Mn-spinel growth was observable on Crofer® 22APU with niobium and silicon, it appeared to be comprised of very small platelets and mostly whiskering, similar to the low-Cr alloy and Crofer® 22APU.

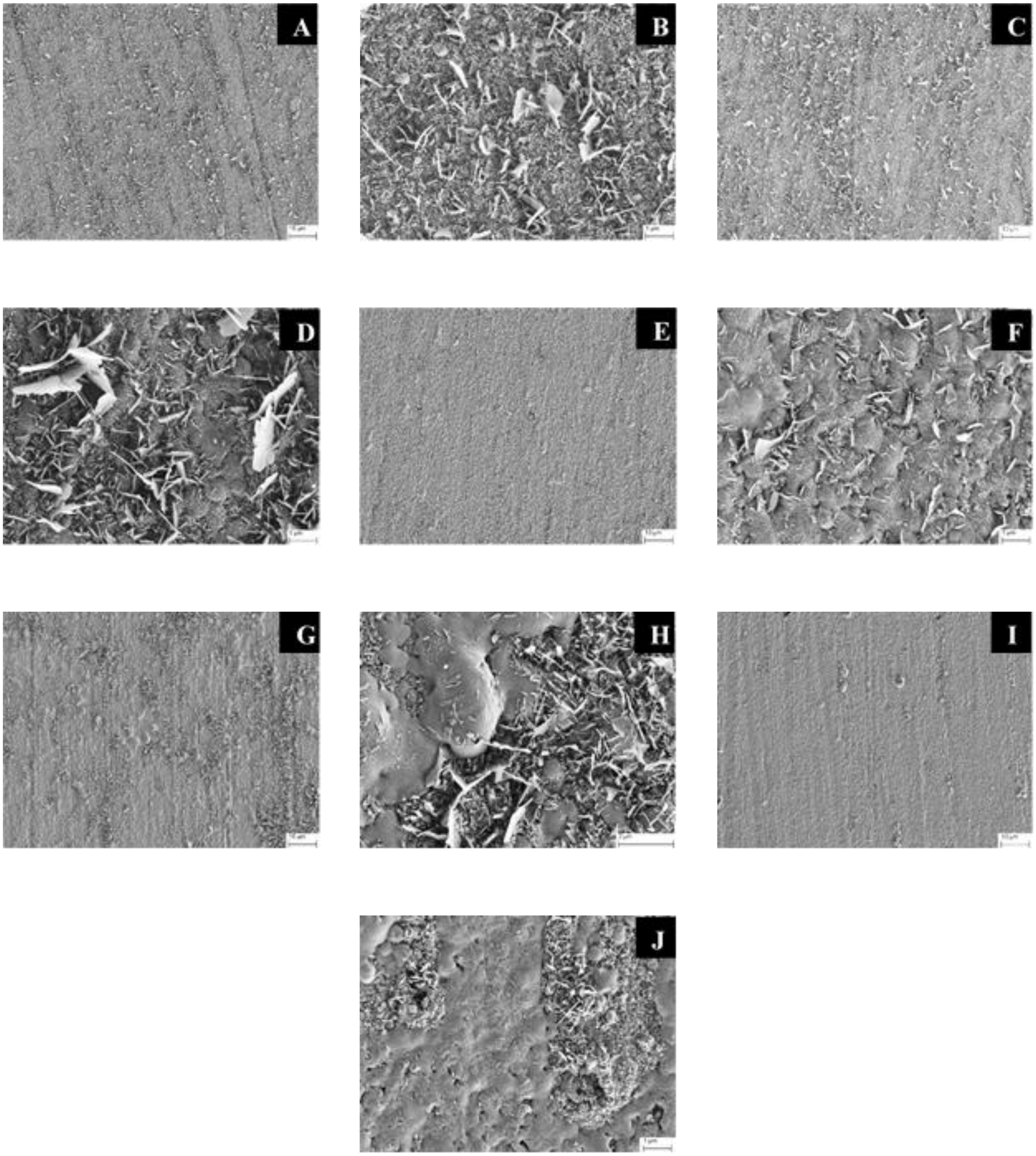

Figure 53. SEM micrographs showing the Mn-spinel growth on MEC (A, B), KDN (C, D), LKC (E, F), KMT (G, H), and KST (I, J) specimens after exposure in simulated anode environment for 220 hours at 700°C

There were very few similarities between the surface morphology of these specimens compared to the ones which were tested in the simulated cathodic environment. Due to a lack of manganese in the Fe-30Cr and the Fe-30Cr-2Mo alloys, none of those specimens which were tested have the ability to create a Cr,Mn-spinel when exposed in the cathodic environment. The only alloy which could do this is the Fe-30Cr-2Mn alloy. When it was exposed for 500 hours in the dry cathodic environment, the coarse face was covered in chromia and iron oxide. The fine face did have a Cr,Mn oxide growth on it, although the scale was relatively uniform and flat, with no platelet growth or whiskering observable. In the wet air cathodic environment, the manganese-doped alloy showed few similarities to the anodic environment surfaces as well. The coarse face had some areas of manganese-rich oxides, possible showing platelet-like Cr,Mn-spinel formation. The fine face again just showed uniform areas of either pure chromia or pure manganese-oxide with no indication of spinel formation.

The pre-coated nickel layer on the remaining specimens prevented an external oxide scale from forming. For this reason, the other specimen surfaces were not examined. Additionally, the surfaces of the Crofer® 22H and Fe-30Cr alloy specimens which were exposed for 500 hours at 700°C were not examined. Instead, SNMS profiling was performed on these specimens, which will be discussed in detail below.

5.2.2 Electrolytic Etching

The electrolytic etch applied to these specimens was a 10% aqueous NaOH solution. The etch turns any sigma phase into a dark yellow/orange color with the rest of the material remaining unaffected. When the etch was applied to the specimens which were not pre-coated with a layer of nickel, no effect was seen and it was determined that no sigma phase formation had occurred in these specimens (see Figure 54). Some of the specimens did show the presence of other small precipitates after the etch had been applied, such as small square shaped carbide precipitates in the low-Cr alloy specimen. However, the specimens overall looked very similar with no sigma phase precipitation present at the surface edge of the sample or at any possible grain boundaries. Due to the lack of sigma phase, no further analyses of these specimens were performed.

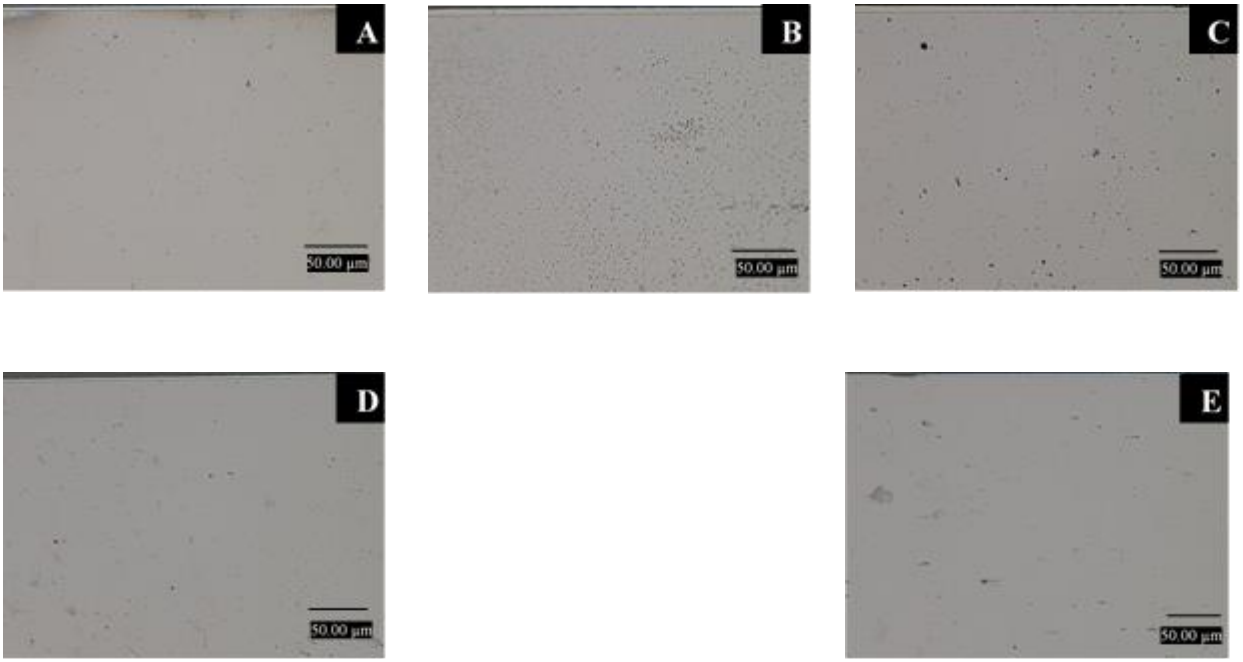

Figure 54. Optical micrographs of electrolytic etching of LKC (A), KMT (B), KST (C), KDN (D), and MEC (E), specimens after 220 hour exposure at 700°C in a simulated anode environment

The same five alloys were pre-coated with a thin nickel layer and then exposed to the simulated anode environment at 700°C for two hours. The cross-sections of these specimens were eletrolytically etched as described above and examined (see Figure 55). Just as with the specimens which had not been pre-coated with a layer of nickel, these specimens did not show any sigma phase formation after the etch was applied. However, an interdiffusion layer between the original nickel pre-coated layer and the outside surface of the specimens can be seen. It is important to note that in the case of some of the specimens, specifically the Crofer® 22APU, and Crofer® 22H specimen, there are areas where there was no pre-coated layer of nickel. In those areas, a lack of diffusion zone is seen, and the surface edge of the specimen looks to be almost identical to the specimens which were not pre-coated with a layer of nickel and were exposed for 220 hours. Just as before, some of the specimens also show internal precipitation, such as the tungsten precipitates seen in the Crofer® 22APU with tunsgten specimen.

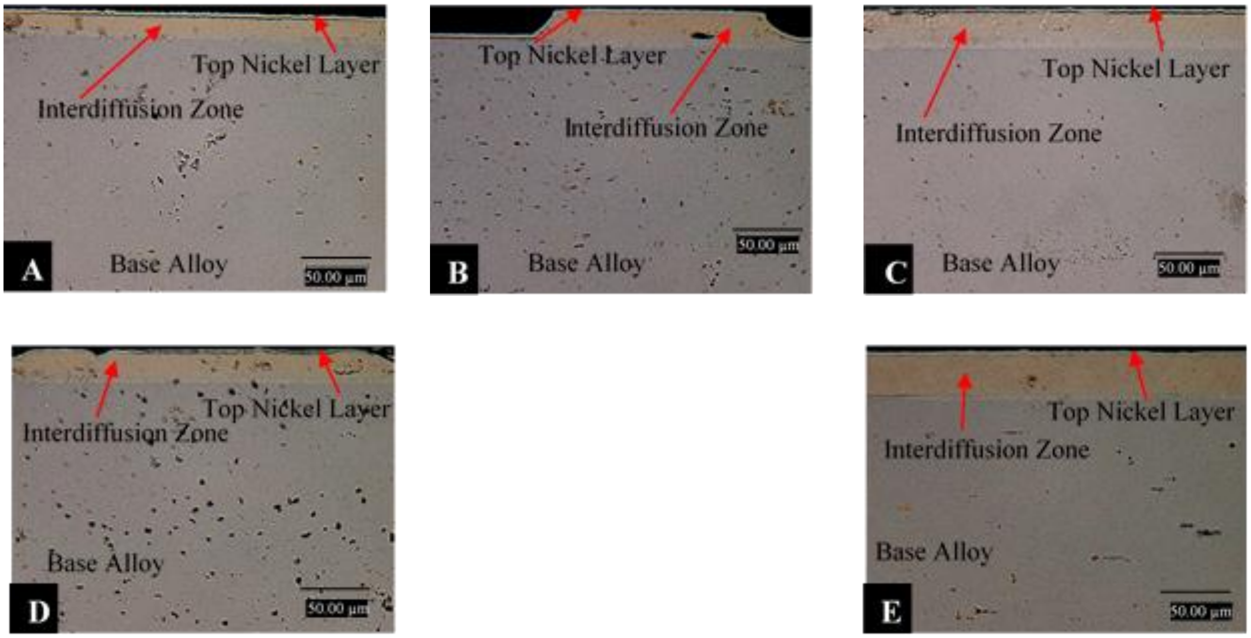

Figure 55. Optical micrographs of electrolytic etching of LKC (A), KMT (B), KST (C), KDN (D), and MEC (E), nickel pre-coated specimens after 2 hour exposure at 700°C in a simulated anode environment

The same five alloys were again pre-coated with a thin layer of nickel and then exposed to the simulated anode environment at 700°C for 22 hours. The cross-sections of these specimens were eletrolytically etched as described above and examined (see Figure 56). Sigma grains had nucleated at the interdiffusion/alloy interface for all the alloys except the low-Cr content alloy. The Crofer® 22H specimen, MEC, had the most sigma formation along the interface edge of the specimen. The alloy doped with tungsten, KDN, also had a significant amount of sigma formation at the interface, although it still seemed less compared to MEC. The alloy doped with niobium and silicon, KST, had a lower amount of sigma formation, and seemed to be roughly the same amount as KMT, the Crofer® 22APU specimen.

There was a formation of an interdiffusion zone between the initial nickel layer and the base alloy for every specimen. It is interesting to note that the interdiffusion zones of all the specimens seem to be comprised of various layers. For almost all samples, with the exception of MEC, the top-most layer of the interdiffusion zone was an oxide. Even in the case of MEC, a thin oxide formation can be seen at the outside surface, although a majority of the formation is deeper into the specimen. After the oxide layer there is a bare zone with no oxide formation, no precipitate formation, and no sigma formation. There is almost a planar interface between this bare zone and the next zone, which has small precipitates of some sort in it. Based on the electrolytic etch, it is hard to tell if these are very small sigma phase precipitates or if they are precipitates based on some other elements in the alloys. Finally, below the precipitate layer for all the alloys except LKC, there was formation of small sigma grains along the boundary of the interdiffusion zone and the base alloy. The grains appeared slightly elongated and non-symmetrical. There was not one particular shape that the grains adhered to, although the height of all of the grains was roughly 2 - 4 microns for all the specimens which contained sigma phase.

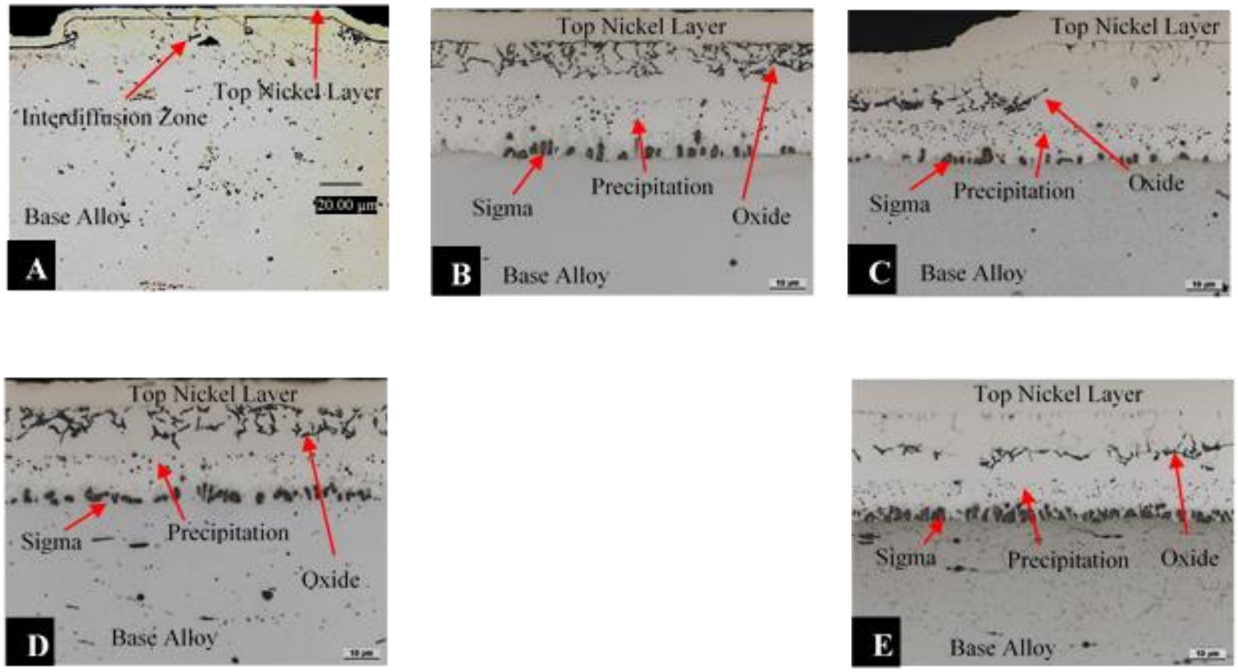

Figure 56. Optical micrographs of electrolytic etching of LKC (A), KMT (B), KST (C), KDN (D), and MEC (E), nickel pre-coated specimens after 22 hour exposure at 700°C in a simulated anode environment

The same five alloys were again pre-coated with a thin layer of nickel and then exposed to the simulated anode environment at 700°C for 220 hours. The cross-sections of these specimens were eletrolytically etched as described above and examined, with similar results compared to the 22 hour exposure (see Figure 57). All of the alloys except for the low-Cr alloy had sigma phase formation, again at the boundary between the nickel interdiffusion zone and the base alloy. The longer exposure time allowed for more grains of sigma phase to nucleate in all samples as well as slightly larger grains of sigma to nucleate. The grains in the various Crofer® 22APU alloy specimens did not really increase in size between the 22 hour exposure and the 220 hour exposure. In contrast, the grains in the Crofer® 22H 220hour specimen were almost double the size of the grains in the 22 hour specimen. After 22 hours of exposure, the sigma grains were about 3 – 4 microns in length in the Crofer® 22H specimen. However, after 220 hours of exposure, the grains grew to about 7 – 8 microns in length for the Crofer® 22H specimen.

Just as with the 22 hour specimens, the 220 hour specimens also have various layers in their interdiffusion zones. The first layer in the low-Cr alloy, Crofer® 22APU, and Crofer® 22APU with tungsten specimens is an oxide layer, whereas the Crofer® 22APU with niobium and silicon and the Crofer® 22H specimens both have a bare outermost layer followed by an oxide layer. For all the alloys, the rest of the layers are similar- a thin bare layer beneath the oxide followed by a precipitate layer of some sort, and then sigma formation which seems to be growing up from the interdiffusion zone/base alloy interface. The electrolytic etch also highlighted the precipitates which some of the alloys contain, especially in the case of the Crofer® 22APU with tungsten specimen.

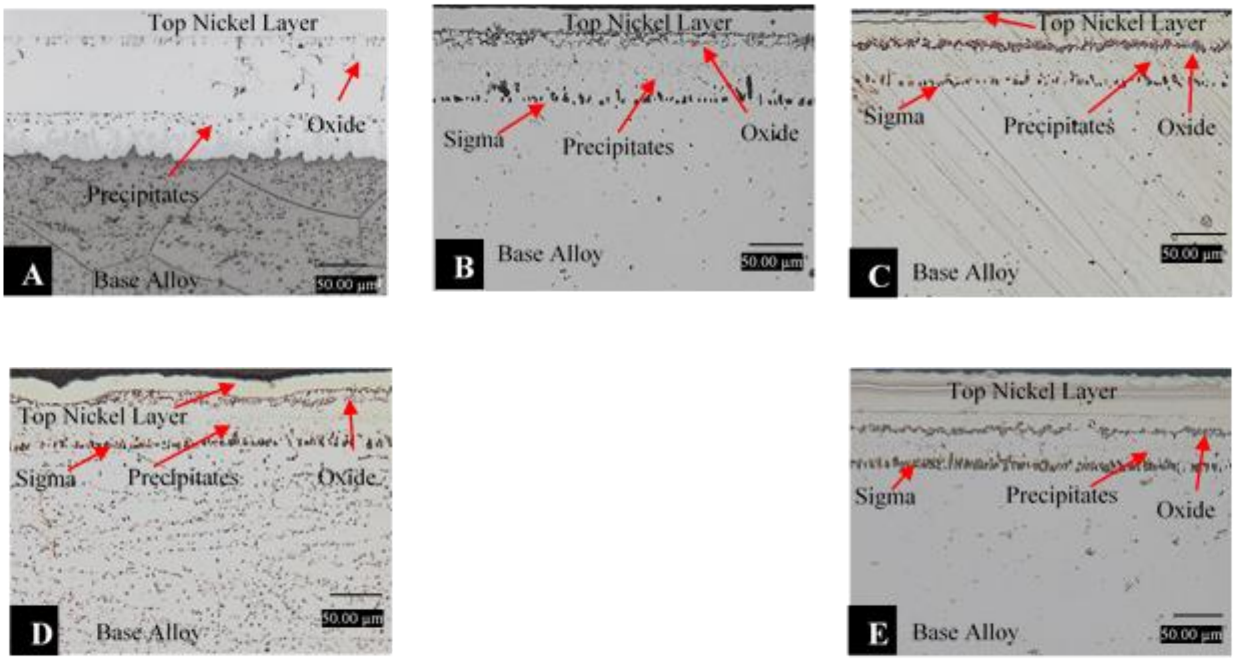

Figure 57. Optical micrographs of electrolytic etching of LKC (A), KMT (B), KST (C), KDN (D), and MEC (E), nickel pre-coated specimens after 220 hour exposure at 700°C in a simulated anode environment

Two alloys, Crofer® 22H and a Fe-30Cr alloy (MPS), were tested in the simulated anode environment at 700°C for 500 hours. For these alloys, two specimens were prepared: one which had been pre-coated with a layer of nickel and one which had not been pre-coated. The cross-sections of these specimens were electrolytically etched and then examined with an optical microscope.

There is clearly a difference between the specimens which were pre-coated with a layer of nickel and those which were not (see Figure 58). The two specimens which were not pre-coated with a layer of nickel showed no sigma phase formation and very little oxide formation. In contrast, the Fe-30Cr specimen which was pre-coated with a layer of nickel not only had an oxide layer and interdiffusion zone, but large sigma grain growth as well. The Crofer® 22H specimen with the pre-coated layer of nickel also showed sigma growth, although the grains were about 5 – 6 microns in length compared to the 10 – 15 micron length grains in the Fe-30Cr specimen (note that the magnification for Figure 58.B and Figure 58.D are different). Unlike the 220 hour specimens, the interdiffusion zones for the 500 hour specimens do not appear to show the same amount of stratification. There is the outer-most oxide layer, followed by the interdiffusion region and then the sigma growth. In the Fe-30Cr specimen, there appears to be a few small precipitates above the sigma grains, although it is hard to tell if they are sigma phase due to their size. Since there was no interdiffusion zone or presence of sigma phase formation, the specimens which were not pre-coated with a layer of nickel were not examined further.

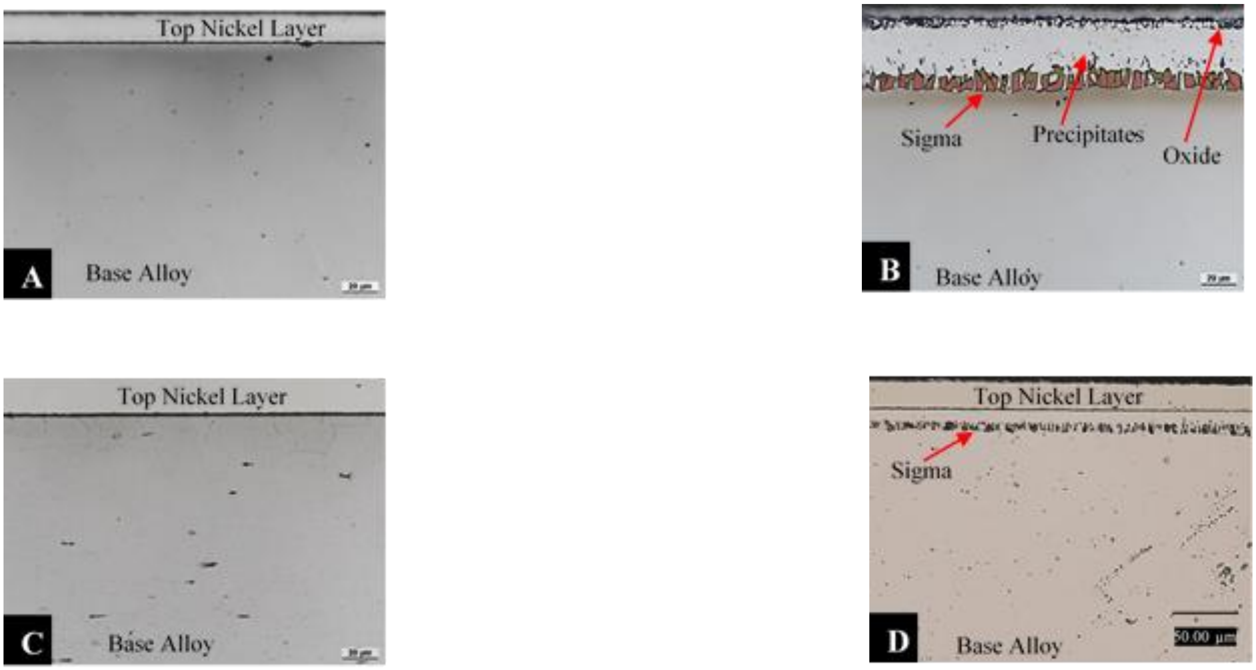

Figure 58. Optical micrographs of electrolytic etching of MPS specimens without (A) and with (B) a pre-coated layer of nickel, and MEC specimens without (C) and with (D) a pre-coated

5.2.3 SEM Cross-Sectional Compositional Analysis

Although there was no sigma formation observable in the 2 hour specimens based on the electrolytic etching, they were still analyzed with the SEM in order to determine the composition of the nickel/alloy interdiffusion zone (see Figure 59).

The delineation point between the lighter interdiffusion area and the darker diffusion area is the point at which the zone transitions from being nickel-rich to being iron-rich. It may also be a phase boundary between an austenitic nickel-rich zone and a ferritic iron-rich zone. At the top of the darker area, the composition still sits within the FCC/austenitic phase on the Fe-Cr-Ni ternary diagram (see Figure 60). However, by the bottom of the zone, the composition has shifted so that it is just inside the sigma-FCC two phase region.

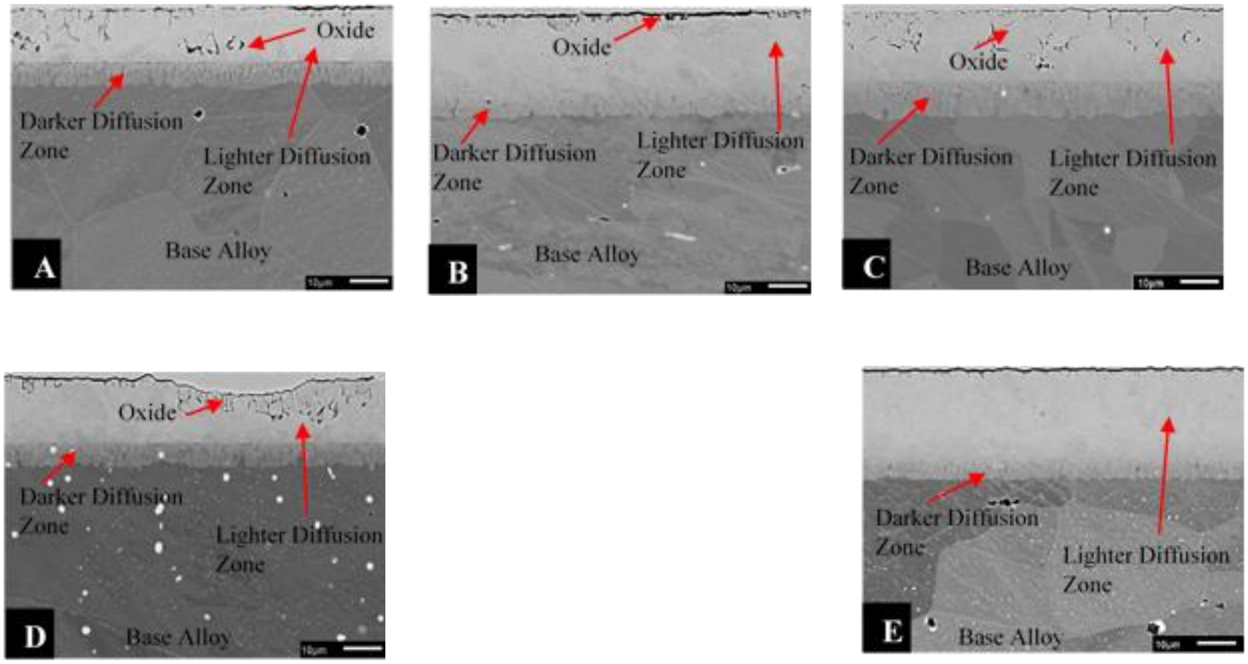

Figure 59. SEM BSE micrographs of LKC (A), KMT (B), KST (C), KDN (D), and MEC (E) after 2 hour exposure at 700°C in a simulated anode environment

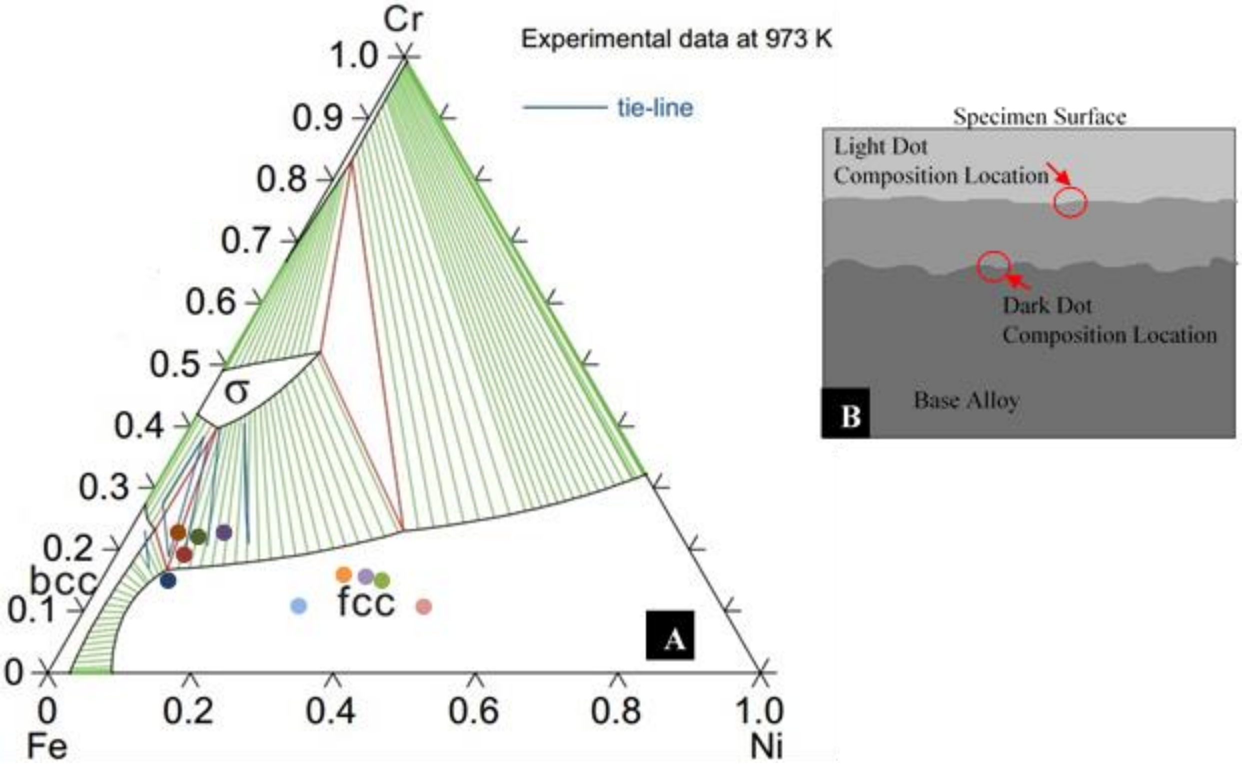

Figure 60. Fe-Ni-Cr ternary diagram (A) showing the composition of the diffusion zone at the dark/light interface (light dots) and base alloy/interdiffusion zone interface (dark dots) for LKC (blue), KMT (red), KST (green), KDN (orange), and MEC (purple) after 2 hour exposure at 700 °C in a simulated anode environment with a schematic (B) of where measurements occurred [36]

Since both the 22 hour specimens and the 220 hour specimens contained sigma phase, only the 220 hour specimens were examined with SEM. The oxide layer for all the specimens except the low-Cr alloy consisted mainly of chromia with some nickel and iron present as well as small amounts of silicon, niobium, and manganese. In the case of the LKC, which is the low-chromium alloy, the oxide consisted of a lower-concentration of chromium with higher amounts of nickel and iron present. All of the alloys appear to have some sort of precipitation in the interdiffusion zone area. In the case of the low-Cr alloy, the precipitates are mostly titanium with some iron, niobium, and nickel present. For the other alloys, the precipitates were too small to get an accurate measurement, but it was seen that they contained trace amounts of sulfur and manganese. The specimen for the Crofer® 22APU with tungsten specimen also contains niobium-rich precipitates, similar to what was seen in the 2 hour specimen. This is to be expected since the addition of tungsten into the alloy should promote the formation of Laves phase precipitates. In the Crofer® 22H specimen, the slightly smaller white precipitates could also be Laves phase precipitates since the alloy also contains tungsten, although lower in concentration compared to the Crofer® 22APU with tungsten specimen.

All the alloys except for the low-Cr alloy have sigma formation, which was observable as a bright white/grey phase in the BSE mode on the SEM (see Figure 61). For the Crofer® 22APU, Crofer® 22APU with tunsgten, and Crofer® 22H specimens there was frequent sigma formation along the interdiffusion-base alloy interface. In these specimens, the grains were elongated with a slightly larger base, and had roughly the same "height" of about 7 – 8 µm. For the Crofer® 22APU with niobium and silicon specimen, there was less observable sigma formation and the grains were much smaller and more spherical in shape. The average height for the sigma grains in this specimen was about 3 – 4 µm. The compositions were roughly the same for all specimens at 57 – 61 wt.% Fe, 27 – 38 wt.% Cr, 3 wt.% Ni. The only exceptions were the Crofer® 22APU with niobium and silicon specimen which had an additional 0.5 wt.% Si in the sigma phase, the Crofer® 22APU with tungsten specimen which had up to 9 wt.% W in the sigma phase, and the Crofer® 22H specimen which had both elements present in the sigma phase at roughly 0.5 wt.% Si and 5 wt.% W.

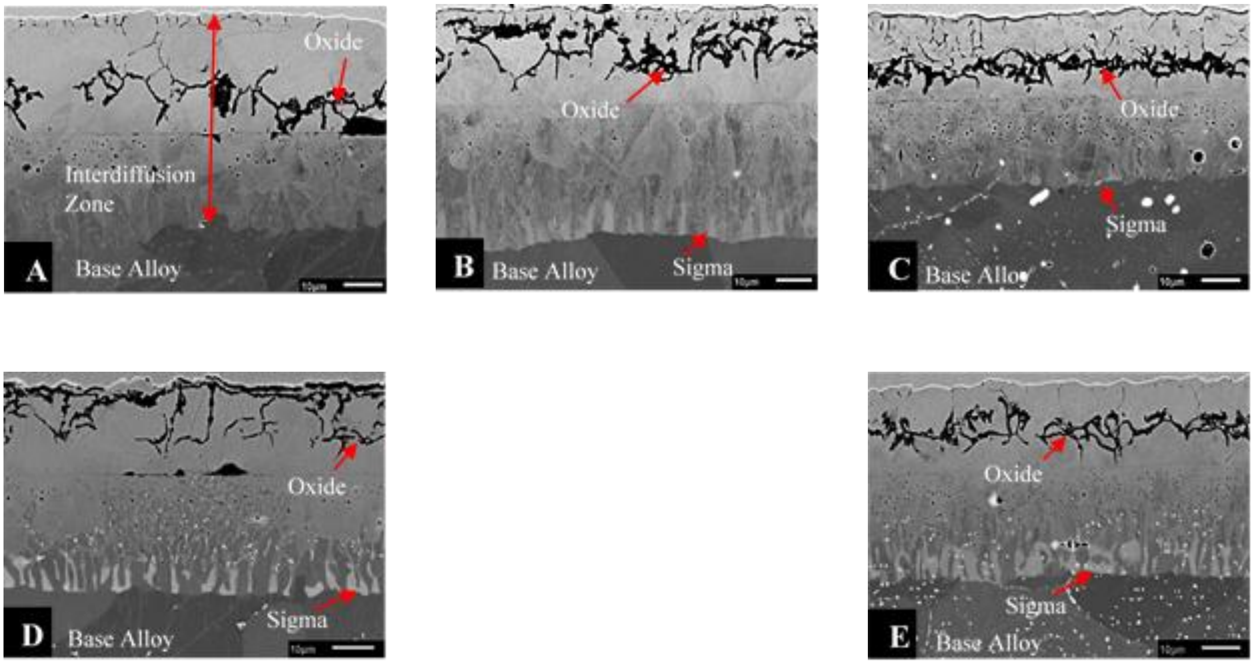

Figure 61. SEM BSE micrographs of LKC (A), KMT (B), KST (C), KDN (D), and MEC (E) after 220 hour exposure at 700°C in a simulated anode environment

Only the nickel-coated specimens which were exposed for 500 hours were examined with the SEM (see Figure 62). The Fe-30Cr specimen had an external oxide scale form whereas the Crofer® 22H specimen had internal oxide formation beneath a nickel-rich surface layer. The oxide layer in the Fe-30Cr specimen was chromium rich with some nickel and iron present. The oxide layer in the Crofer® 22H specimen is also chromium rich, with iron, nickel, and manganese present as well as lesser amounts of silicon and niobium. The sigma phase in the Fe-30Cr specimen had a composition of roughly 57 – 62 wt.% Fe, 34 – 40 wt.% Cr, 3 – 4 wt.% Ni. The sigma phase in the Crofer® 22H specimen had a composition of 55 – 58 wt.% Fe, 31 – 35 wt.% Cr, 3 – 5 wt. % Ni, and 5 wt.% W which was similar to the phase composition seen in the 220 hour specimen. Small white precipitates were visible in the Crofer® 22H specimen, similar to the 220 hour specimen, and are assumed to be Laves phase precipitates rich in niobium. It is interesting to note that even after 500 hours of exposure there was very little depletion of elements just below the sigma phase-base alloy boundary.

Figure 62. SEM BSE micrographs of MPS (A) and MEC (B) after 500 hour exposure at 700°C in a simulated anode environment

5.2.4 SEM EBSD Analysis

EBSD analysis was performed on some of the 2 hour specimens to determine if an austenite/ferrite boundary existed between the interdiffusion zone and the base alloy. There was some difficulty using the OIM software to identify phases because sigma phase is not available in the database. Generally, it seems as if the database will identify sigma to be ferrite phase during analysis. The grains appear elongated in some of the figures due to some drifting during the EBSD scan. Drifting can be a problem for analysis because EBSD requires a clean surface free of any etch or sputtering, but also requires high conductivity. Since the oxide scale must be preserved, the specimens are cold mounted in a non-conductive epoxy resin. To create some conductivity, copper tape is applied to one end of the specimen and wrapped around the mount. However, it appeared that this may not supply sufficient conductivity, and so some specimens also received a very thin palladium sputtered coating to help provide additional conductivity during analysis. Due to the difficulty of obtaining accurate scans, only the MEC specimen results will be discussed.

Previous results indicate a lack of sigma formation in the 2 hour Crofer® 22H specimen which had been pre-coated with a layer of nickel. There was, however, an interdiffusion zone between the initial nickel layer and the base alloy. The scan area (see Figure 63) encompasses the entire diffusion zone as well as some of the base alloy. Grain boundary orientation is not particularly revealing for this scan, but the phase mapping does indicate the diffusion zone boundaries. The bottom of the image is the surface of the sample. The bright green indicates austenite phase which is contributed by the nickel-rich coating. The bright red indicates a strong ferrite presence. In Figure 63.C a bright red line is visible near the top of the scan. This line is around where the interdiffusion zone ends and the base alloy begins. Based on the figure, it appears as if the interdiffusion zone may be a mix of austenite and ferrite, but the boundary between the base alloy and the interdiffusion zone is comprised of a majority of ferrite. It should be noted that the top of Figure 63.C, which is the base alloy, should be mostly red since Crofer® 22H is ferritic in nature. However, due to the difficulty of maintaining conductivity and the sensitive nature of EBSD analysis, the software had a difficult time determining the phase composition at various points in the scan. For this reason, the base alloy appears as a mixture of austenite and ferrite.

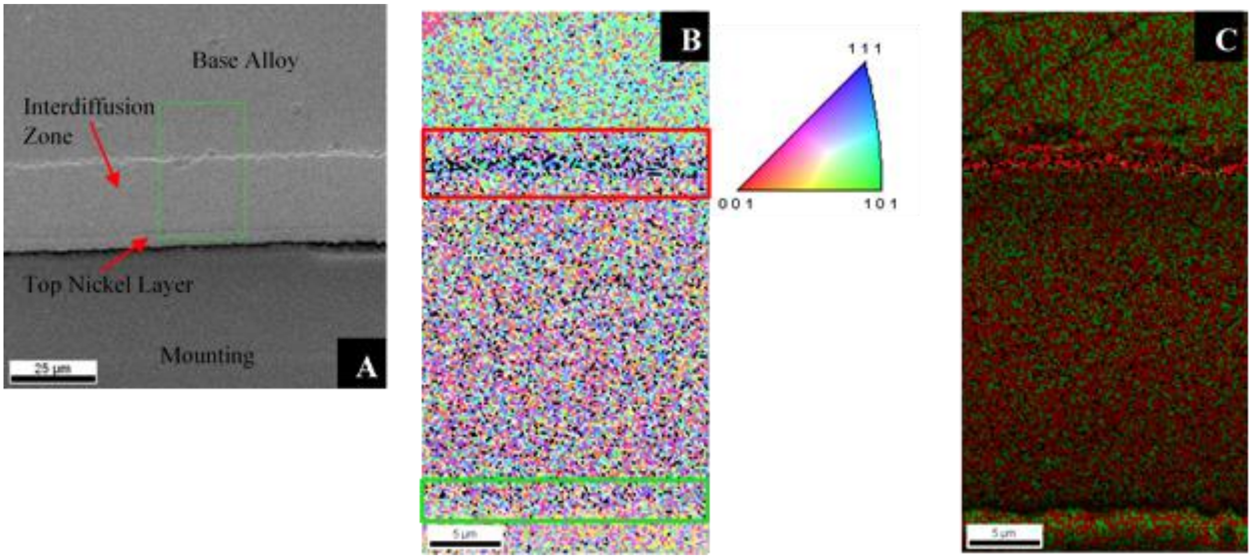

Figure 63. SEM micrograph of area being analyzed for EBSD enclosed in a green box (A), grain orientation of scanned area with emphasis on interdiffusion zone/base alloy interface (red box) and interdiffusion zone/nickel top coat interface (green box) (B), phase ovelay of scanned area with ferrite/sigma indicated by red and austenite indicated by green (C) for MEC specimen pre-coated with a layer of nickel exposed in a simulated anode environment at 700 °C for 2 hours

EBSD analysis was also performed on some 220 hour specimens which had been pre-coated with a layer of nickel and showed sigma phase formation to determine if the sigma grains were preferentially nucleating at any particular phase boundary. Again, due to the difficulty of obtaining accurate scans, only the Crofer® 22H specimen results will be discussed.

When the Crofer® 22H specimen was analyzed, the sigma phase appeared to be growing at the ferrite/austenite interface and tended to have the same crystallographic orientation, close to the [111] direction (see Figure 64). The ferrite, which is the base alloy material, was observed to have large grains. The austenite which was the diffusion zone was observed to have smaller grains. The sigma phase, however, had the smallest grains, as seen in Figure 64.B. That is, what appeared to be a single grain during electrolytic etching and SEM BSE analysis was actually a conglomerate of very small grains around 1 – 2 microns in size. The sigma grains are the small, roughly uniform shaped grains which are conglomerated together into elongated “super grain” shapes. Their preferential growth direction allows them to be easily spotted in Figure 64.B because of their purple/blue color compared to the multi-colored ferrite and austenite grains which surround them. It should be noted that the grain boundaries are determined by the OIM software which marks grain boundaries starting at angles of misorientation which are greater than 2°. So many of the sigma grains may be due to very low misorientation values.

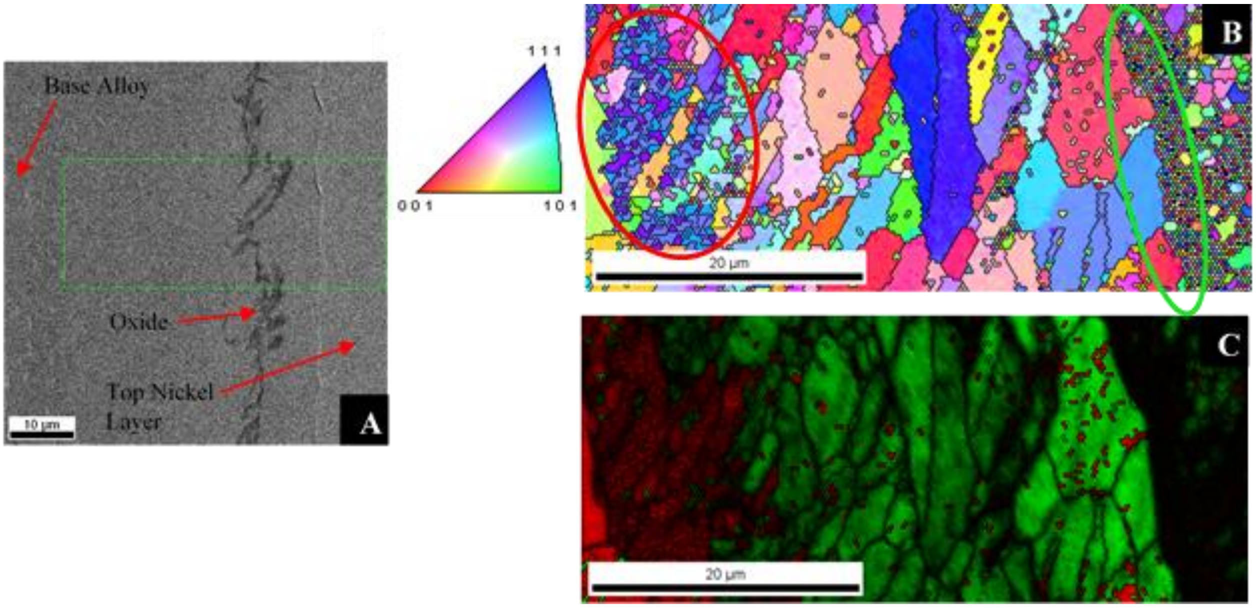

Figure 64. SEM micrograph of area being analyzed for EBSD enclosed in a green box (A), grain orientation of scanned area with emphasis on interdiffusion zone/top nickel layer boundary (green oval) and sigma grain formation (red oval) (B), phase overlay of scanned area with ferrite/sigma indicated by red and austenite indicated by green (C) for MEC specimen pre-coated with a layer of nickel exposed in a simulated anode environment at 700°C for 220 hours

Finally, EBSD was performed on the 500 hour Fe-30Cr specimen which had been pre-coated with a layer of nickel (see Figure 65). A lack on conductivity on the sample surface did cause the beam to drift, which in turn created a scan of elongated grains. In analyzing this scan, is it important to ignore the shape of the grains and instead focus on orientation and phase mapping. In the grain orientation mapping, it is difficult to determine where the sigma phase is located. However, in the phase overlay mapping, a clear distinction can be seen. A majority of the scan is the base alloy, which is seen as bright red elongated grains. The edge of the specimen is seen as the bright green area, representing austentite, which indicates the high-nickel content at the top of the interdiffusion zone. The interdiffusion zone itself is a mix of green and red, or austenite and ferrite. Interestingly, what appears to be darker red grains of ferrite seem to be attached to the base alloy material and growing into the interdiffusion zone. These darker red grains are the sigma phase, similar in nature to the ones seen in the 220 hour Crofer® 22H specimen. In this case, it appears as if sigma phase only nucleated and grew at a boundary of what would have initially been the ferritic base alloy and the austenitic interdiffusion zone.

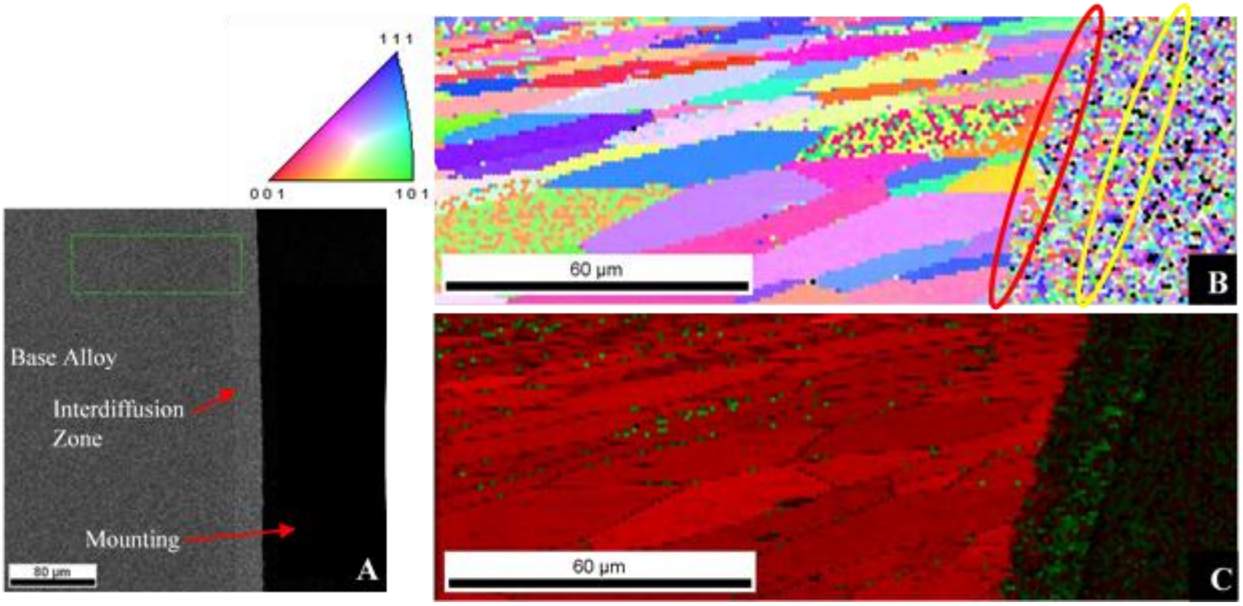

Figure 65. SEM micrograph of area being analyzed for EBSD enclosed in a green box (A), grain orientation of scanned area with emphasis on interdiffusion zone/top nickel layer interface (yellow oval) and base alloy/interdiffusion zone interface (red oval) (B), phase overlay of scanned area with ferrite/sigma indicated by red and austenite indicated by green (C) for MPS specimen pre-coated with a layer of nickel exposed in a simulated anode environment at 700°C for 500 hours

5.2.5 SNMS Analysis

SNMS profiling was performed on the two Crofer® 22H specimens which were exposed in the anodic environment for 500 hours (see Figures 66, 67). The profiles were used to compare the chemical composition of the oxide scale and see how the addition of a pre-coated layer of nickel affected diffusion of the elements during exposure. The samples are uniformly sputtered during analysis, so that the sputtering time can be correlated to the penetration depth into the specimen from the surface which is represented by a time of 0 seconds.

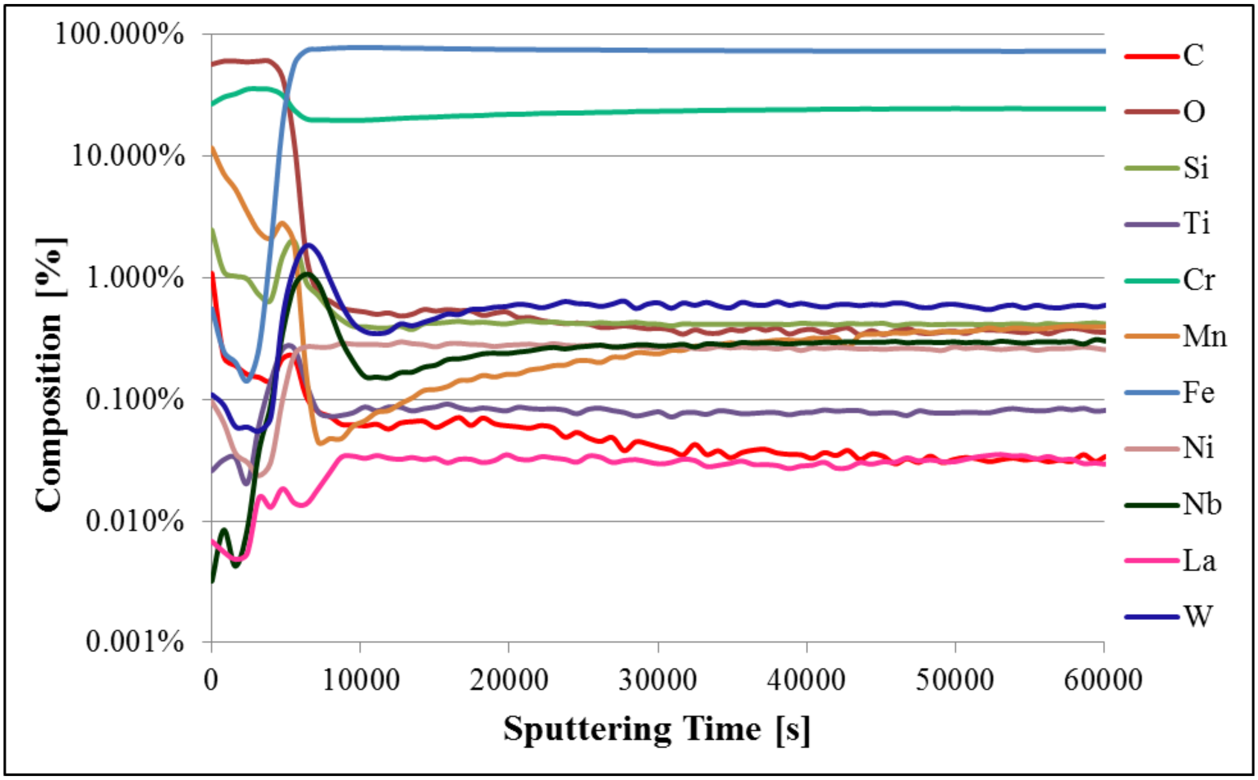

Figure 66. SNMS profile of MEC specimen after 500 hour exposure at 700°C in a simulated anode environment

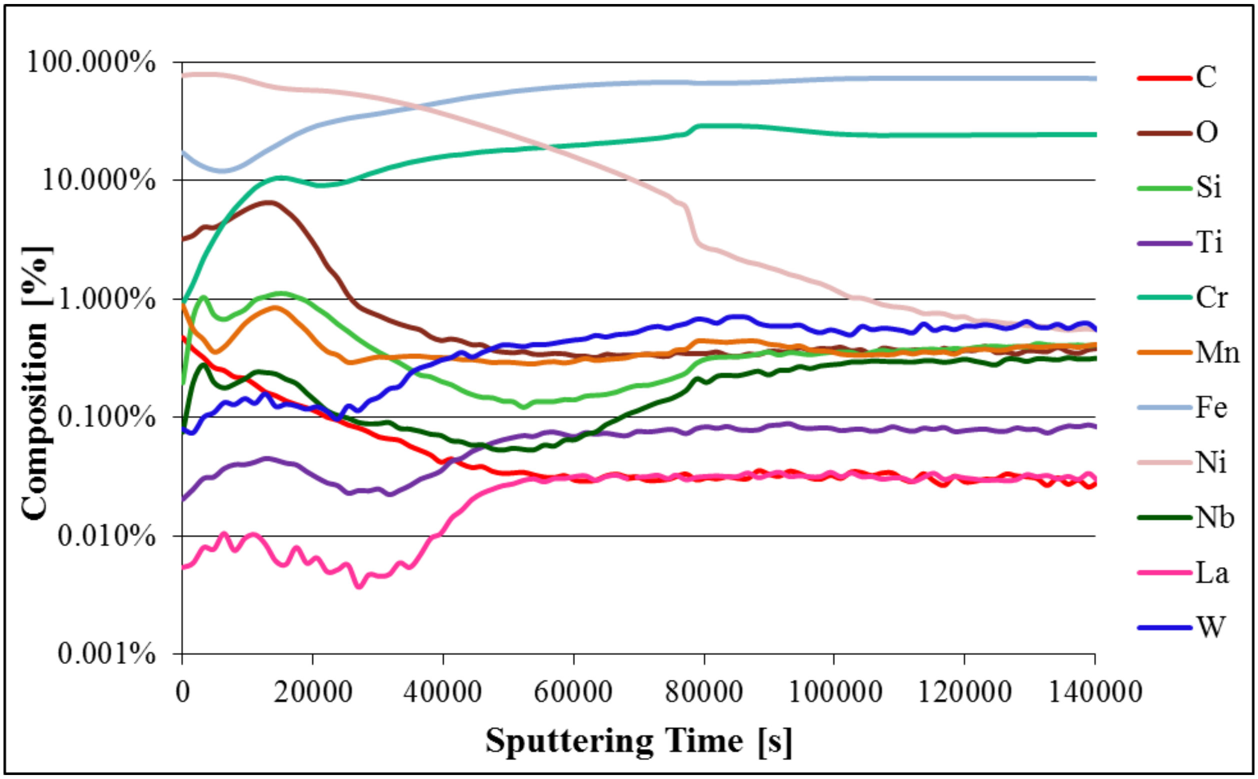

Figure 67. SNMS profile of MEC specimen pre-coated with nickel after 500 hour exposure at 700°C in a simulated anode environment

Both the profiles confirm earlier results that the oxide scale on the samples consisted of a chromia layer with an outer layer of Mn,Cr-spinel. The uncoated specimen has an oxide layer followed by a layer enriched with silicon, tungsten and niobium. While the uncoated Crofer® 22H has the oxide scale on the surface of the specimen, the nickel-coated Crofer® 22H shows a more complex behavior, with the oxide precipitates forming within the initial nickel layer. The coated specimen has an oxide which contains silicon and niobium along with the manganese and chromium. Due to niobium enrichment in the oxide layer, there is a depleted zone in the sub-oxide layer which could result in a vanishing of the Laves phase in the subsurface zone of this specimen. Just as with the niobium enrichment, the silicon enrichment in the oxide layer of the nickel-coated specimen leads to a depletion zone in the sub-surface of the steel.

The addition of the pre-coated layer of nickel also causes the sub-surface diffusion zone to substantially increase. In the Crofer® 22H specimen with no coating, the base alloy composition is reached after roughly 10,000 seconds of sputtering time. However, in the case of the nickel-coated Crofer® 22H specimen, it takes almost 130,000 seconds to reach the base alloy composition due to significant nickel diffusion through the specimen. If the nickel diffusion is ignored, then it still takes about 80,000 seconds of sputtering time to reach base alloy composition due to the sub-surface depletion of silicon and niobium.

5.2.6 The Effect of Nickel Diffusion on Sigma Formation

The results from the anode-simulated environments show a distinct effect of the pre-exposure nickel layer on the formation of sigma phase in the ferritic alloys tested. The most obvious difference comes in the comparison of the Fe-30Cr specimen which was exposed for 500 hours. The addition of a thin layer of nickel caused the formation of large sigma grains. Clearly, the ability of nickel to diffuse into an iron-chromium alloy, and the ability of iron and chromium to diffuse outwards, is causing some sort of phase transformation, not just in terms of sigma, but also in terms of austenite. This is similar to results obtained by Niewolak et. al. where the addition of a nickel layer caused a phase transformation from ferrite to austenite and then from austenite to sigma [13]. Alternatively, Villanueva et. al. suggested that the sigma formation happens due to a eutectoid decomposition of delta ferrite into austenite and sigma phase. Similar to the results seen with these specimens, they noted that sigma phase formed in the ferrite region but needed a minimum amount of austenite-favorable elements, such as nickel, to form [37].

Generally speaking, EBSD results showed that the interdiffusion zone, due to the high concentration of nickel, consisted mainly of austenite. Comparing the interdiffusion zone of all the sigma-phase containing specimens, many similarities could be seen. The cross-sectional progression of layers is schematically shown in Figure 68.

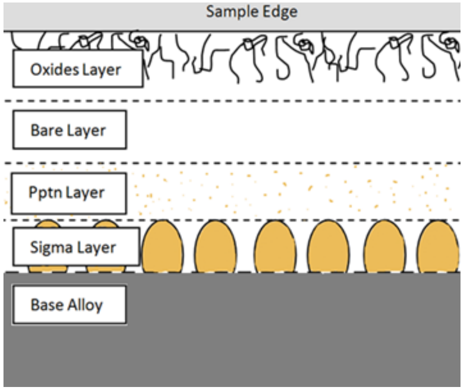

Figure 68. Schematic of sample cross-section which contains sigma phase

As discussed above, the common factors of all the sigma-containing specimens were an oxide layer, a seemingly "bare" layer devoid of any oxides or precipitates, a precipitation layer, a sigma layer, and then immediately the base alloy. It is important to note that some specimens had an outermost layer of almost pure nickel followed by an internal oxide scale, but beyond that the specimens were similar in the remaining layers. Due to the small nature of the precipitates above the sigma layer, it was difficult to determine if the precipitates were small sigma phase precipitates, or based on the other alloying elements present in the material.

A comparison of the cross-sections of the various Crofer® 22H specimens which were exposed with a pre-coated layer of nickel allows for a rough determination of the velocity of the growth of the interdiffusion zone (see Figure 69). By measuring the depth of the interdiffusion zone from the surface and comparing it against the various exposure times, the velocity can be determined and compared (see Equation 2).

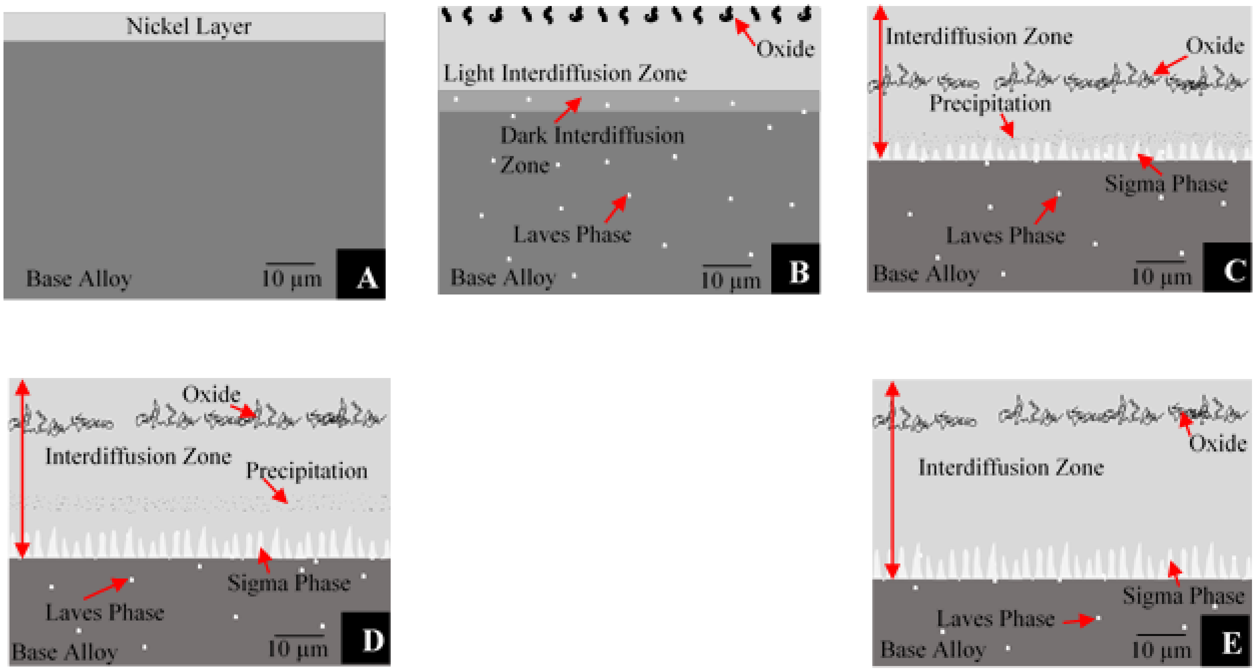

Figure 69. Schematic of growth of interdiffusion zone for MEC alloy pre-coated with nickel before exposure (A), after 2 hours of exposure (B), after 22 hours of exposure (C), after 220 hours of exposure (D), and after 500 hours of exposure (E) in a simulated anode environment at 700 °C

Some noticeable changes can be seen between the 2 hour exposure and the other exposures. Most prominently is the formation of sigma phase sometime between 2 and 22 hours of exposure Additionally, the 2 hour exposure has a two-layer interdiffusion zone, with the lighter layer being nickel rich and the darker layer being iron and chromium rich. After 22 hours, once the sigma phase has formed, this interdiffusion zone is a continuous layer in terms of appearance, although the composition vastly changes from the top, where it is almost 100 wt.%

nickel, to the bottom (near the formation of sigma phase) where the composition is more enriched in iron and chromium.

$$v = \frac{L_{IDZ,t2} - L_{IDZ,t1}}{t2 - t1} \qquad (2)$$

Using equation 2, the velocity of the interdiffusion zone growth can be calculated and compared for the exposure times (see Table 6). By substituting the height of the sigma grains for the length of the interdiffusion zone, the relative growth rate of the sigma grains can also be calculated and compared (see Table 7). It is also worth comparing the penetration depth of the interdiffusion zone and its relation to time to see if it follows the typical diffusion relation seen in equation 3 where x would be depth of the interdiffusion zone, and t is the exposure time (see Figure 70).

$$x = 2\sqrt{Dt} \qquad (3)$$

Table 6. Comparison of interdiffusion zone velocities

Exposure time [hr]	Calculated velocity [cm/s]
22	1.528×10^{-8}
220	5.618×10^{-10}
500	3.968×10^{-10}

Table 7. Comparison of sigma growth rates

Exposure time [hr]	Calculated growth rate [cm/s]
22	5.556×10^{-9}
220	5.612×10^{-10}
500	1.984×10^{-10}

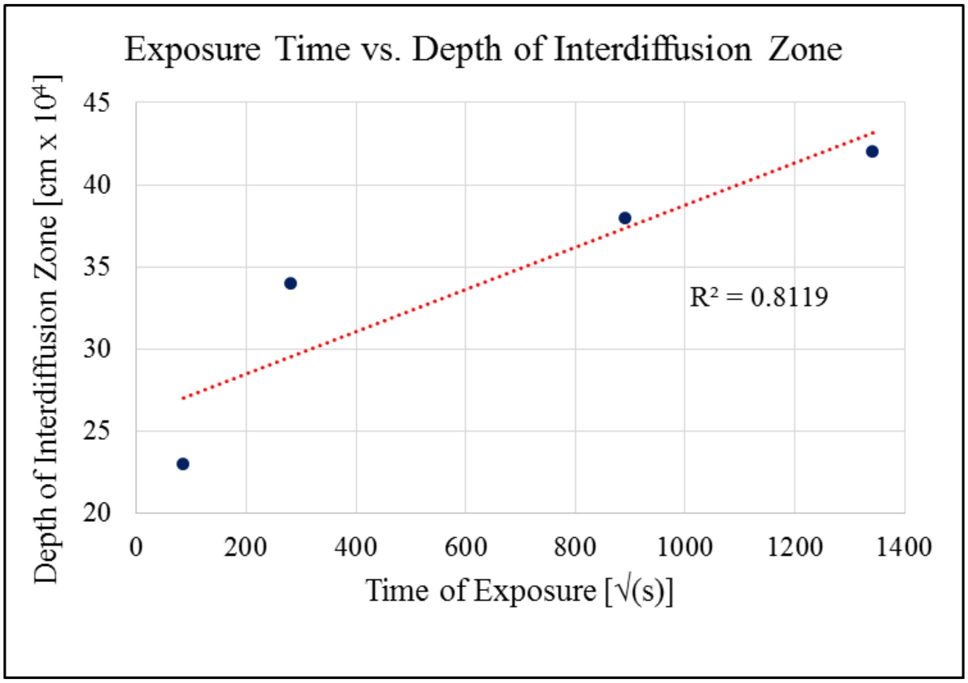

Figure 70. Comparison of depth of interdiffusion zone with exposure time

Based on the velocities shown in Table 6, it appears as if the diffusion rate of nickel into the base alloy decreases over time. In the early stages of exposure, the growth rate of the interdiffusion zone is a factor of 100 times bigger than the growth rate for longer exposure times. The interdiffusion zone is created by the nickel diffusing downwards into the alloy and the iron and chromium diffusing upwards through the nickel layer. Initially, it seems as if it is easier for nickel to diffuse downwards, since the 2 hours specimen has a large area of nickel-rich diffusion zone compared to a small area of iron and chromium-rich diffusion zone. Eventually, the iron and chromium concentration at the interface between the base alloy and the diffusion zone must become large enough that sigma phase is able to nucleate and grow. This is similar to results seen by Hsieh and Wu which stated that δ-ferrite to sigma transformation forms in high Cr-concentrated regions of ferrite particles [38]. The relationship between the interdiffusion zone and the exposure time is somewhat linear, with an R^2 value of 0.8119. However, this is not a very strong correlation and four data points is too few to define a definitive relationship.

However, just as how the interdiffusion zone slows its growth over time, the sigma phase also slows growth over time, although not as significantly. Between 22 hours and 220 hours of exposure, the sigma phase slows growth by a factor of 10. This could be because the sigma phase initially grows in the chromium-rich ferrite phase, but then grows into the nickel-rich austenite phase. According to Hsieh and Wu, the diffusion velocity of sigma phase-forming elements through δ-ferrite is much faster than through austenite, so this could be an explanation of why the phase can nucleate easily at first, but then is much slower to grow [38].

Using the SEM and EDX analysis on the Fe-30Cr specimen with sigma phase, a rough diffusion path could be determined between the initially pure nickel layer and the base alloy underneath (see Figure 71). It is interesting to note that the sigma phase compositions lie in the two-phase region of sigma and ferrite, although it is very close to the pure sigma phase region. Also note that the oxide layer is ignored when determining the compositional change through the cross-section.

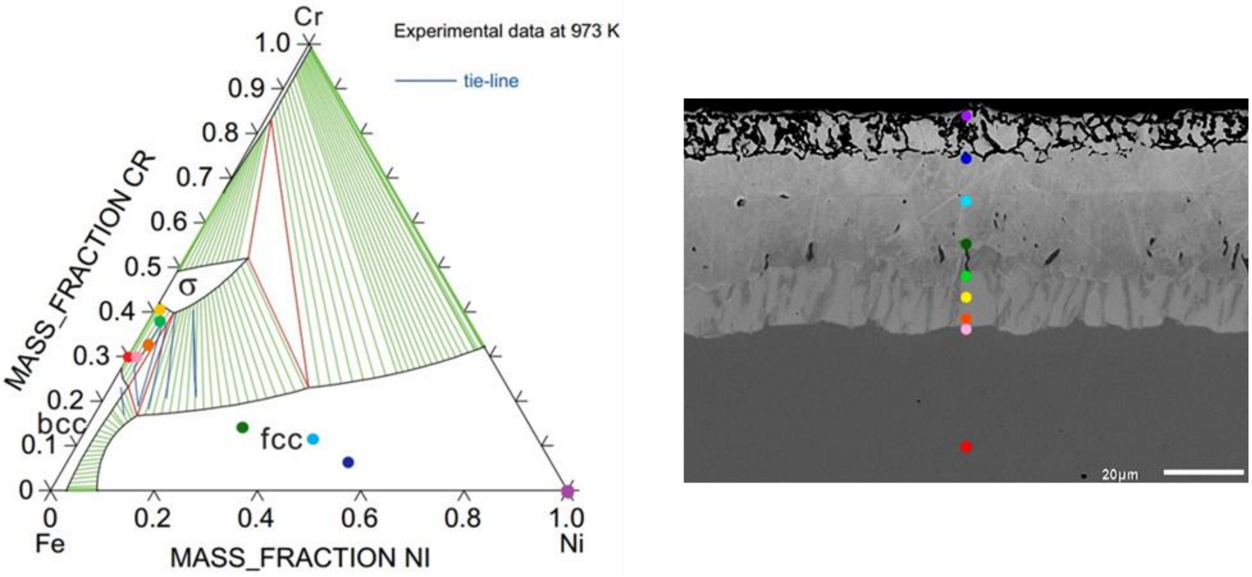

Figure 71. Ternary phase diagram showing progressing of phase compositions based on SEM micrograph and characterization of nickel pre-coated MPS specimen exposed in a simulated anode environment at 700°C for 500 hours [36]

Based on earlier analysis, it was determined that there were two areas which were chromium-rich: the oxide layer as well as the sigma layer. It was also determined that the base-alloy just below the sigma layer was not depleted in chromium. Therefore, most of the interdiffusion zone was depletion in chromium, some to the extent of having little-to-no chromium present. There may be a moving interface between the bare alloy and the sigma layer which produces the elongated sigma grains. As the nickel is able to diffuse downwards and chromium is able to diffuse upwards, sigma phase can be created. However, near the top of the grains, the nickel concentration becomes large enough to cause a phase transformation from sigma to austenite. The increased nickel content may strongly inhibit sigma formation due to the pointed "tops" of the sigma grains compared to the wide "bottom" of the grains. The temperature of exposure may also have an effect of the shape of the sigma grains. When the temperature is lower, near 600°C, the sigma grains are more rounded, however as temperature increases to 800-900°C the grains change shape into a more faceted and needle-like morphology [37]. Since these alloys were exposed at an intermediate temperature of 700°C it could explain why the sigma grains were sometimes rounded, but with longer exposure tended to elongate into a thinner morphology.

This effect may be seen in the difference between the sigma grain formation of the 22 hour exposed specimens compared to the 220 hour exposed specimens. In the 22 hour specimens, the grains were about 2 – 4 microns in length and the shape was more uniform/circular compared to the elongated shapes of the 220 hour specimens. Although the size of the sigma grains did not change for the Crofer® 22APU family specimens, the Crofer® 22H specimens (which have the highest chromium content) almost doubled in size from 2 – 4 microns to 7 – 8 microns in length. In all the specimens, the interdiffusion zone also increased in size from about 28 – 30 microns to 40 – 42 microns. However, after 500 hours of exposure, the nickel-coated Crofer® 22H specimen had an interdiffusion size similar in length to the 220 hour specimen. Also, the sigma grains were roughly the same size after 500 hours of exposure compared to after 220 hours of exposure. This indicates that there may be a maximum diffusion limit for the nickel from the coating or that the moving interface only travels for so long before slowing down and eventually stopping.

According to work done by Villanueva et. al., the formation of sigma phase in superferritic and duplex steels is not from the transformation of austenite into sigma phase, but rather ferrite directly into both austenite and sigma phase. This is because, traditionally, the transformation of sigma phase from austenite is incredible sluggish and can take thousands of hours to occur [37]. In this work, sigma phase was seen after as few as 22 hours with the presence of an austenitic/ferritic boundary.

Just like the alloys tested in the cathodic environment, the alloys tested in the anodic environment are ferritic in nature. Specifically, the Crofer® 22APU family and Crofer® 22H specimens which are Fe-Cr alloys with the chromium-content ranging between 20.65 – 22.9 wt.%, and all lie in the pure ferrite phase field of the ternary diagram. The addition of the nickel layer, which causes diffusion of nickel, chromium, and iron when exposed in the high temperature anodic environment, allows for "uphill diffusion" of the alloy from the purely ferritic phase to almost purely sigma phase, before turning and eventually becoming the austenitic phase of pure nickel (see Figure 72). Composition measurements were taken at various points through the interdiffusion zone, sigma phase, and base alloy in order to determine the possible diffusion path. Regardless of the composition of the alloy, all of the alloys which formed sigma phase had a similar diffusion path, with slight differences in the composition of the sigma phase itself and the "sharpness" of the turn from sigma phase back to austenite.

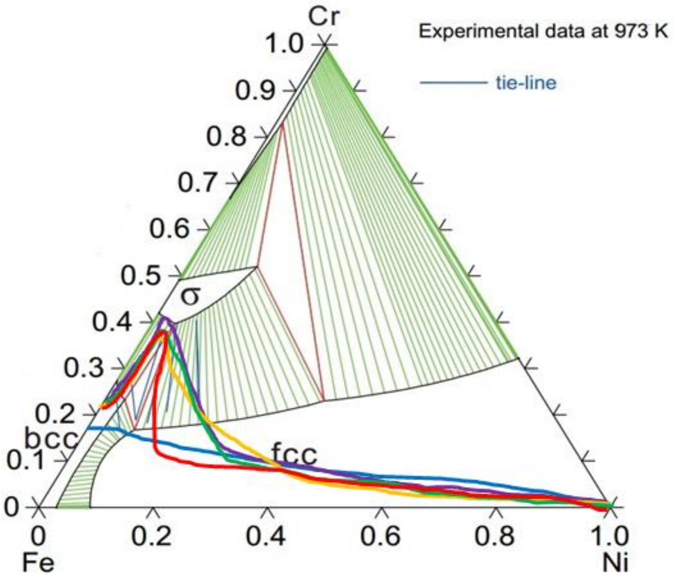

Figure 72. Fe-Ni-Cr ternary diagram showing the composition-based diffusion paths for LKC (blue), KMT (red), KST (green), KDN (orange), and MEC (purple) after 220 hour exposure at 700°C in a simulated anode environment [36]

Another phenomenon for a few specimens was the addition of other alloying elements into the sigma phase composition. In particular, the Crofer® 22APU with niobium and silicon specimen had an additional 0.5 wt.% silicon, the Crofer® 22APU with tunsgten specimen had up to 9 wt.% tungsten, and the Crofer® 22H specimen had both 0.5 wt.% silicon and 5 wt.% tungsten in the sigma phase composition. The addition of silicon into the sigma phase for the Crofer® 22APU with tungsten specimen and Crofer® 22H specimen is surprising because the amount in the phase is double that of the base alloying element. This indicates a particular segregation of the silicon into the sigma phase and also may explain why a depletion zone of silicon can be seen in the SNMS profile. Based on EDX analysis, it was seen that parts of the austenitic interdiffusion zone were incredibly rich in nickel compared to the iron and chromium rich ferritic base alloy. When delta-ferrite is rich in sigma forming elements, such as chromium, molybdenum, and silicon, compared to the austenite, this aids in the precipitation of sigma phase and leads to a sigma phase which itself is rich in the sigma forming elements, which could explain the presence of the silicon [37]. Tetsui et. al. showed that silicon can easily dissolve into the ferrite phase and affect sigma phase formation. In their work, the addition of silicon caused a lattice strain effect similar of that to cold working, which aided in the nucleation of sigma phase [32]. A similar phenomena may be occurring in the specimens here where the silicon from the base alloy is easily diffusing to the ferrite/austenite boundary of the base alloy with the interdiffusion zone. Once there, the addition of silicon can lead to additional nucleation energy beyond that of the phase boundary mismatch.

Tungsten acts in a similar way in the Crofer® 22APU with tungsten and Crofer® 22H specimens. Although it is only added in up to 2.6 wt.% as an alloying element, it is seen at up to three times that concentration in the sigma phase. Just as with the molybdenum addition in the binary alloy tested in the cathodic environment, the addition of tungsten in the anodic environment samples may be causing additional strain energy during exposure. Tungsten has an atomic radius of 139 pm, which is the same as molybdenum. If tungsten is replacing chromium in the matrix, it may be causing additional strain energy which allows for easier formation of sigma phase during exposure. This is contrary to results seen by Tetsui et. al. where their addition of 4 wt.% tungsten into an Fe-30Cr alloy did not cause formation of sigma phase. Their theory was that not enough energy was created from the tungsten mismatch in the ferrite matrix to generate sigma phase nucleation [32]. If this is the case, then the nickel interdiffusion zone is a necessary second requirement for sigma phase formation in Fe-Cr alloys with tungsten. In this case, the addition of the tungsten along with the phase boundary mismatch allowed for easier formation of sigma phase, especially considering that the chromium content of this alloy was only 20.65 wt.% compared to the 30 wt.% in the work done by Tetsui et. al.

Additionally, EBSD analysis showed that the boundary between the diffusion zone and the base alloy was comprised of mostly ferrite phase. The diffusion zone is austenitic in nature, and there may be strain from the incompatibility between the BCC ferrite phase and the FCC austenite phase. This incompatibility may aide in the nucleation of sigma phase at this boundary point, which was also suggest by Hsieh and Wu when they determined that precipitation of sigma phase can occur due to the high energy from the high energy mismatch of ferrite phase and austenite phase [38]. Singhal and Martin also had similar results where they stated that a high energy interface may be necessary for the growth of sigma phase [25]. In the EBSD results, sigma phase was seen to be growing from the ferritic base alloy into the austenitic diffusion zone. The OIM analysis software also classified sigma phase as ferrite phase during phase mapping, which could be explained by the fact that sigma formation occurs through the consumption of ferrite phase with a locally high chromium content. This growth mechanism is suggested by Singhal and Martin for their work with duplex stainless steels and Hsieh and Wu have similar theories for their work as well [25, 38]. This growth mechanism is also suggested by Villanueva et. al. who suggest that the ferrite is directly decomposing through a eutectoid reaction into austenite and sigma. In their work, sigma phase formed directly in the ferrite phase, which could explain why the EBSD software classified it as ferrite phase [37].

Finally, it should be noted that the only specimen which did not form sigma phase when pre-coated with a layer of nickel was the low-Cr alloy specimen. This is probably due to the low-chromium content of the alloy compared to the other specimens tested. This indicates that there is some minimum chromium concentration required in the base alloy for sigma phase precipitation to occur. Based on the specimens tested, this value is somewhere between 17.3 – 20.65 wt.% chromium. This minimum may be required to create a high enough chromium concentration locally at the ferrite/austenite interface in order for sigma precipitation to occur. However, although no sigma phase formed in this low-chromium alloy, there was still a phase transformation from ferrite to austenite which created an interdiffusion zone in the alloy, just as with the other specimens.

5.2.7 Summary of Simulated Anode Environment Results

Five ferritic alloys of various chromium content were exposed for 220 hours in a simulated anode environment at 700°C. All specimens showed the same result: an external chromia layer with a manganese spinel and a lack of sigma formation in the alloy.

The same five alloys were then coated with a layer of nickel before again being exposed in a simulated anode environment at 700°C, but only for two hours. Electrolytic etching of these specimens revealed that all specimens had an interdiffusion zone between the initial nickel coating and the base alloy. However, none of the specimens showed signs of sigma formation.

The same alloys were again coated with a layer of nickel and exposed in a simulated anode environment at 700°C for 22 hours. Once again, all specimens had an interdiffusion zone between the initial nickel layer and the base alloy. However, all of the alloys except the low-Cr alloy also showed signs of sigma formation, with small, slightly elongated grains forming at the interface between the interdiffusion zone and the base alloy. When the same alloys were exposed for 220 hours in the same conditions, the results were almost identical. The only difference was that the interdiffusion zone in the Crofer® 22H specimen had increased in size, as had the sigma grains. The other alloys showed no difference in results between 22 hours of exposure and 220 hours of exposure.

Compositional analysis revealed that the sigma formation in the ferritic alloys was roughly identical. The sigma phase composition was determined to be 57 – 61 wt.% Fe, 27 – 28 wt.% Cr, and 3 wt.% Ni. The only difference from this composition was that the Crofer® 22APU with niobium and silicon alloy had an addition 0.5 wt.% Si in the sigma phase, the Crofer® 22APU with tungsten alloy had an additional 9 wt.% W in the sigma phase, and the Crofer® 22H alloy had an additional 0.5 wt.% Si and 5 wt.% W in the sigma phase.

The Fe-30Cr alloy and the Crofer® 22H alloy were exposed in a simulated anode environment at 700°C for 500 hours both with and without the pre-coated nickel layer. An electrolytic etch showed clear sigma formation in the specimens which had been pre-coated with a layer of nickel, most significantly in the Fe-30Cr specimen. Compositional analysis of the sigma phase in these specimens was similar to the sigma phase of the other specimens.

EBSD analysis was performed on some specimens to determine if there was a preferential site for sigma phase nucleation and growth. The Crofer® 22H alloy specimen which was exposed for two hours was analyzed first. Phase mapping showed that the interdiffusion zone of the specimen was comprised of mostly austenite phase and that the boundary between the interdiffusion zone and the base alloy, where the sigma phase is theorized to nucleate, was comprised of mostly ferrite phase. The Crofer® 22H specimen which was pre-coated with nickel and exposed for 220 hours was next examined. Phase mapping showed the sigma phase as being ferritic in nature. When grain mapping was used, the sigma phase was shown to be growing preferentially in a nearly [111] direction. It was also determined that each “grain” of sigma phase seen in the micrographs of the electrolytically etched samples were actually comprised of many smaller grains of sigma phase. The Fe-30Cr specimen which was pre-coated with nickel and exposed for 500 hours was examined last. Similar to the 220 hour Crofer® 22H specimen, the 500 hour Fe-30Cr specimen had a sigma phase which phase mapping associated with ferrite. The sigma in the specimen appeared to be attached to the ferritic base alloy although the orientation of the grains was difficult to determine.

Finally, SNMS profiling was performed on the Crofer® 22H specimens exposed for 500 hours. Both profiles confirmed that an oxide scale rich in chromium with a Mn,Cr-spinel had formed during exposure. However, the specimen which was pre-coated with a layer of nickel also had silicon and niobium in the oxide layer. This enrichment of those elements in the oxide layer caused a depletion area further down into the interdiffusion zone, which may explain why there was a lack of Laves phase in part of the interdiffusion zone compared to the matrix.

6.0 CONCLUSIONS

A variety of alloys were tested in both cathodic and anodic environments at 700°C. In the cathodic environments, a binary Fe-30Cr alloy did not show any sigma formation after 500 hours of exposure. The addition of 2 wt.% manganese into the alloy showed a few signs of small sigma formation after 500 hours of exposure in a wet-air cathodic environment. The addition of 2 wt.% molybdenum showed significant sigma formation after 500 hours of exposure in both a dry and wet air environment. The molybdenum in the alloy may be replacing the chromium in the matrix which leads to additional strain energy which allows for easier sigma formation. Additionally, the presence of water vapor in the exposure environment caused an increased amount of sigma formation and growth, which suggests that water vapor, particularly the hydrogen in the water, may be decreasing the incubation time necessary for initial sigma phase nucleation.

In the anodic atmosphere, all of the alloys which were exposed formed a chromia oxide layer with additional Mn,Cr-spinel. When specimens which were pre-coated with a layer of nickel showed formation of an interdiffusion zone after as little as 2 hours of exposure. Many of the alloys began to show sigma phase formation after as little as 22 hours of exposure. Therefore, in practical applications during SOFC use, the direct contact of nickel parts with the steel interconnects could result in a number of degradation phenomena dependent on steel composition and exposure time (see Figure 73).

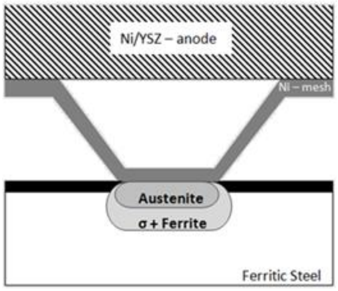

Figure 73. Schematic of possible steel degradation phenomena during SOFC operation

These degradation phenomena include microstructural transformation of ferrite into austenite in the 17 wt.% Cr steels and microstructural transformation of ferrite into austenite and sigma phase in the 20 – 22 wt.% Cr steels. There may be a minimum chromium content required in the alloys for the diffusion path to cross into a sigma-containing phase field in order for sigma phase nucleation and growth to occur. In all cases, chromium depletion occurs in the alloys. A possible solution to this problem would be to create a low-chromium Crofer® type alloy which avoids these transformations. Another solutions is to create protective coating between the steel and nickel parts to prevent the nickel diffusion from occurring.

BIBLIOGRAPHY

[1] Rosenberg, Matt. “Current World Population”. *The New York Times Company*, Last Updated: 2011. Online. Accessed February 20, 2013. <http://geography.about.com/od/obtainpopulationdata/a/worldpopulation.htm>

[2] Yuming, Xu. “Nuclear Energy Development in China”. *China Atomic Energy Authority*, Last Updated: July 31, 2002. Online. Accessed February 20, 2013. <http://www.caea.gov.cn /n602670/n621902/32228.html>

[3] Brett, D., Atkinson, A., Brandon, N., & Skinner, S. “Intermediate temperature solid oxide fuel cells.” *Chemical Society Reviews* 37.8 (2008): 1568 – 1578. Online.

[4] Froitzheim, J. “Ferritic Steel Interconnectors and their Interactions with Ni Base Anodes in Solid Oxide Fuel Cells (SOFC).” Diss. Rheinisch-Westfälischen Technischen Hochschule Aachen, 2008. Online.

[5] Irvine, J. & Connor P. (Ed.) *Solid Oxide Fuel Cells: Facts and Figures*. London: Springer, 2013. Print.

[6] Badwal, S. & Foger, K. “Solid Oxide Electrolyte Fuel Cell Review.” *Ceramics International* 22.3 (1996): 257 – 265. Online.

[7] Ishihara, T. (Ed.) *Perovskite Oxide for Solid Oxide Fuel Cells*. London: Springer, 2009. Print.

[8] Minh, N. “Solid oxide fuel technology – features and applications.” *Solid State Ionics* 174.1 - 4 (2004): 271 – 277. Online.

[9] Bossel, U. “Does a Hydrogen Economy Make Sense?” *IEEE* 94.10 (2006): 1826 – 1837. Online.

[10] Singhal, S. & Kendall, K. (Ed.) *High Temperature Solid Oxide Fuel Cells: Fundamentals, Design and Applications*. Oxford: Elsevier, 2006. Online.

[11] Hammer, J., Laney, S., Jackson, R., Coyne, K., Pettit, F., & Meier, G. The Oxidation of Ferritic Stainless Steels in Simulated Solid-Oxide Fuel-Cell Atmospheres.” *Oxidation of Metals* 67. 1-2 (2007): 1 – 38. Online.

[12] Fergus, J. “Metallic interconnects for solid oxide fuel cells.” *Materials Science & Engineering A* 397.1-2 (2005): 271 – 283. Online.

[13] Niewolak, L., Wessel, E., Hüttel, T., Asensio-Jimenez, C., Singheiser, L., & Quadakkers, W. “Behavior of Interconnect Steels in Carbon Containing Simulated Anode Gas of Solid Oxide Fuel Cells.” *Journal of the Electrochemical Society* 159.11 (2012): F725 – F732. Online.

[14] Niewolak, L., Wessel, E., Singheiser, L., & Quadakkers, W. “Potential suitability of ferritic and austenitic steels as interconnect materials for solid oxide fuel cells operating at 600°C.” *Journal of Power Sources* 195.22 (2010): 7600 – 7608. Online.

[15] Froitzheim, J., Meier, G., Niewolak, L., Ennis, P., Hattendorf, H., Singheiser, L., & Quadakkers, W. “Development of high strength ferritic steel for interconnect application in SOFCs.” *Journal of Power Sources* 178.1 (2007): 163 – 173. Online.

[16] Dubiel, S. & Cieślak, J. “Sigma-phase in Fe-Cr and Fe-V alloy systems and its physical properties.” Rev. AGH University of Science and Technology Kraków, 2011. Online.

[17] *Iron-Chromium (Fe-Cr) Phase Diagram*. Computational Thermodynamics Inc., 2011. Web. Accessed 19 August 2013.

[18] Bain, E. & Griffiths, W. “An Introduction to the Iron-chromium-nickel Alloys.” *Transactions of the American Institute of Mining and Metallurgical Engineers* 75 (1927): 166 – 211. Online.

[19] Jette, W. & Foote, F. “The Fe-Cr Alloy System.” *Metals & Alloys* 7 (1936): 207 – 210. Online.

[20] Bergman, G. & Shoemaker, P. “The Determination of the Crystral Structure of the σ Phase in the Iron-Chromium and Iron-Molybdenum Systems.” *Acta Crystallographica* 7.12 (1954): 857 – 865. Online.

[21] Zhu, W. & Deevi, S. “Opportunity of metallic interconnects for solid oxide fuel cells: a status on contact resistance.” *Materials Research Bulletin* 38.6 (2003): 957 – 9752. Online.

[22] Birks, N., Meier, G., & Pettit, F. *Introduction to the High-Temperature Oxidation of Metals*. New York: Cambridge University Press, 2006. Print.

[23] Meier, G., Yanar, N., Gleeson, B., Mayer, J., & Quadakkers, W. “Surface Reactivity of H_2O and CO_2 Molecules on High Temperature Materials.” Grant Proposal: Office of Naval Research Arlington, 2012. Print.

[24] Dheeradhada, V., Cao, H., & Alinger, M. “Oxidation of ferritic stainless steel interconnects: Thermodynamic and kinetic assessment.” *Journal of Power Sources* 196.4 (2011): 1975 – 1982. Online.

[25] Singhal, L. & Martin, J. “Metallurgical Transactions.” *Iron Steel Institute* 207 *(*1969): 1382

[26] Yano, K. & Abiko, K. “Formation of σ Phase in Highly Purified Fe – Cr Alloys.” *physica status solidi (a)*160.2 (1997): 449 – 457. Online.

[27] Weiss, B. & Stickler, R. “Phase Instabilities During High Temperature Exposure of 316 Austenitic Stainless Steel.” *Metallurgical Transactions* 3.3 (1972): 851 – 866. Online.

[28] Magnabosco, R. “Kinetics of Sigma Phase Formation In a Duplex Stainless Steel.” *Materials Research* 12.3 (2009): 321 – 327. Online.

[29] Anantatmula, R. “Occurrence and Prediction of Sigma Phase in Fuel Cladding Alloys for Breeder Reactors.” *Journal of Nuclear Materials* 125.2 (1984): 170 – 181. Online.

[30] Hsieh, C. – C. & Weite, W. “Phase Transformation of δ → σ in Multipass Heat-Affected and Fusion Zones of Dissimilar Stainless Steels.” *Metals and Materials International* 17.3 (2011): 375 – 381. Online.

[31] Anderson, T. & Lundberg, B. “Effect of Mo on the Lattice Parameters and on the Chemical Composition of Sigma Phase and $M_{23}C_6$ Carbide in an Austenitic 25Cr-20Ni Steel.” *Metallurgical Transactions A* 8A.5 (1977): 787 – 790. Online.

[32] Tetsui, T., Shinohara, M., & Abiko, K. “Aging Properties of Ultra-High-Purity Fe-High-Cr Alloys.” *physica status solidi (a)* 160.2 (1997): 459 – 467. Online.

[33] Abiko, K. “The Evolution of Iron.” *physica status solidi (a)*160.2 (1997): 285 – 296. Online.

[34] Gaskell, D. *Introduction to the Thermodynamics of Materials, Fifth Edition*. New York: Taylor & Francis Group, LLC, 2008. Print.

[35] Bechtoldt, C.J. & Vacher, H.C. “Phase-Diagram Study of Alloys in the Itron-Chromium-Molybdenum-Nickel System.” *Journal of Research of the National Bureau of Standards* 58.1 (1957): 7 – 19. Online. Works Cited

[36] Hertzman, S. & Sundman, B. “A thermodynamic analysis of the Fe-Cr system.” *CALPHAD* 6 (1982): 67-80.

[37] Villanueva, W., Junior, F., Plaut, R., & Padilha, A. “Comparative study on sigma phase precipitation of three types of stainless steels: austenitic, superferritic and duplex.” *Materials Science and Technology* 22.9 (2006): 1098 – 1104.

[38] Hsieh, C.-C. & Wu, W. “Overview of Intermetallic Sigma Phase Precipitation in Stainless Steels.” *ISRN Metallurgy* 2012 (2012): 1 – 16.